UNIVERSITÀ DEGLI STUDI DI TRIESTE

XXXVI CICLO DEL DOTTORATO DI RICERCA IN

NANOTECHNOLOGIE

TUNING OF MAGNETOELECTRIC COUPLING IN MULTIFERROIC HETEROSTRUCTURES

Settore scientifico-disciplinare: **FIS/03**

DOTTORANDO
DEEPAK DAGUR

COORDINATORE
PROF. ALBERTO MORGANTE

SUPERVISORE DI TESI
DR. PIERO TORELLI

CO-SUPERVISORE DI TESI
DR. GIOVANNI MARIA VINAI

ANNO ACCADEMICO 2022/2023

‘‘The purpose of education is to replace an empty mind,
with an open one.’’

\- Malcolm Forbes

Contents

Preface

This Ph.D. thesis contains the result of the scientific research undertaken through the University of Trieste at CNR-IOM laboratory located at the Elettra Synchrotron, Trieste. The main goal of the project was to investigate the interfacial magnetic modifications of ferromagnetic thin films deposited on photo-ferroelectric substrates as a function of two external stimuli, specifically visible light excitation and thermal treatments. In this context, two experimental characterizations have been performed to characterize and model the effects of the stimuli on the heterostructures. Here I introduce the main aspects that will be presented throughout the thesis.

The study depicted in the chapter 3 of the thesis discusses the potentiality of light-induced effects in multiferroic heterostructures for tuning the interfacial magnetoelectric coupling, emphasizing the role of photo-ferroelectric materials' sensitivity to light illumination. Specifically, the effects of 405 nm laser illumination were characterized on the ferroelectric and ferromagnetic responses of (001) $Pb(Mg_{1/3}Nb_{2/3})O_3$-$_{0.4}PbTiO_3$ (PMN-PT)/Ni heterostructures. By combining magneto-optic, spectroscopic, electrical, and structural characterizations, I demonstrated that light illumination above the ferroelectric bandgap energy induces a photovoltaic current and an induced photostrictive effect in the PMN-PT substrate. This second aspect directly impacts the magnetic response of the interfacial magnetostrictive Ni layer. In particular, photocurrent measurements and I(E) curves demonstrate the generation of free charge carriers via bulk photovoltaic effect in PMN-PT that leads to modifications in the internal electric field and induction of photostrictive effect. Furthermore, the effect of photostrictive behavior of PMN-PT under light was explored on the magnetic properties of magnetostrictive Ni layer. Magneto-Optic Kerr effect measurements showed a substantial reduction in the coercive field of Ni film upon exposure to light. This was linked to the modifications of PMN-PT substrate via X-ray Magnetic Circular Dichroism measurements, which revealed a variation of Ni orbital moment in presence of light illumination, a signature of modification of the electronic environment of Ni driven by the interfacial photostriction. This underlines the importance of spectroscopic techniques in identifying the physical origin of interfacial coupling and emphases on the delicate energy balance that leads to significant light-induced effects in multiferroics, highlighting the potential for optically-induced strain modulation as an effective approach for tuning the ferromagnetic properties. Finally, the study provides comprehensive insights into the complex interplay between light-induced effects, ferroelectric-ferromagnetic counterparts and interfacial properties in multiferroic heterostructures, offering potential avenues for tailoring and optimizing functionalities.

In chapter 4, I present the study carried out on the effects of thermal treatments on the structural and ferroic properties of PMN-$_{0.4}$PT/Fe multiferroic heterostructures. The research combines structural, spectroscopic, and magnetic characterizations to understand the impact of thermal annealing on the domain population of PMN-PT substrates, and how this affects the interfacial properties of the heterostructure. XRD analysis revealed that the pristine unannealed PMN-$_{0.4}$PT substrates exhibited a combination of majoritarian out-of-plane and minoritarian in-plane domains, with low crystalline quality and an isotropic lattice response to polarization-dependent micro-Raman characterizations, indicating a high level of local disorder. Thermal treatments carried out by annealing the PMN-PT substrate over its first-order phase transition lead to a substantial increase in crystallographic quality and local order, along with a switch in the domain population from mostly out-of-plane to in-plane orientation in case of quick annealing. These structural modifications and the changes in orientation of PMN-PT domains were found to be sensitive to the time span of annealing above Curie temperature, as longer thermal treatments lead to a maximization of the out-of-plane domain direction. The combination of X-ray absorption spectroscopy and Magneto-Optic Kerr measurements allowed to analyze the effects of thermal treatments on electronic and magnetic properties of the interfacial Fe layer. XAS showed no chemical modifications of the Fe thin film over the whole thermal treatment procedure; in particular, no sign of oxidation coming either from the PMN-PT substrate or from the atmosphere was found, excluding any thermally induced interfacial intermixing or oxygen migration between Fe and PMN-PT during the annealing processes. MOKE magnetometry showed the passage of Fe layer from isotropic to anisotropic behavior upon annealing, linked to the structural modifications of the PMN-PT substrate. These findings confirm that the modification and rearrangement of ferroelectric domains upon annealing influences the interfacial coupling in multiferroic heterostructures, and stimulate for further investigations, both on the ferroelectric properties of thermally treated PMN-PT crystals and on the interplay between annealed PMN-PT and ferromagnetic interfacial layers.

Overall, the thesis addresses the effects of external stimuli on the interfacial coupling mechanisms in multiferroic heterostructures that lead to tunable modifications in ferroic properties. The results show the potential for the application of external stimuli different from electric and magnetic fields to act on the magnetic properties of multiferroic heterostructures. Moreover, these results also leave open questions on the maximization of interfacial coupling, which could be reached, for instance by combining the observed effects of the two systems. Finally, the observed effects stimulate for further investigations, including different experimental approaches and the introduction of different ferroelectric substrates, providing a rich playground for future experiments and modeling.

Abstract

The work presented in this thesis deals with the optical and thermal control of magnetism in multiferroic heterostructures. The main goal was to investigate the interfacial magnetic modifications of magnetic properties of ferromagnetic (FM) thin films deposited on photo-ferroelectric (FE) substrates, as a function of two external stimuli, specifically visible light excitation and thermal treatments. The photo-induced effects of low-power 405 nm visible light illumination on the ferroelectric and magnetic properties of PMN-$_{0.4}$PT/Ni heterostructures were investigated by combining electrical, structural, magnetic, and spectroscopic characterizations, in both pristine and polarized states of the PMN-PT substrate. The results show that under light illumination, the photostriction of PMN-PT induces an interfacial strain on the magnetostrictive Ni layer. This leads to an optical modification of the Ni orbital moment, leading up to a 45% reduction in coercive field under illumination, as observed by Magneto-Optic Kerr effect (MOKE). The light-induced variation in the Ni orbital moment was experimentally observed for the first time in multiferroic heterostructures, via sum-rule analysis of x-ray magnetic circular dichroic measurements (XMCD). The observed effect is strongly reduced after polarizing the PMN-PT substrate out-of-plane. This was justified by the larger photostrictive contribution coming from the in-plane FE domains. These results shed light on the delicate energy balance that leads to sizeable light-induced effects in multiferroic heterostructure. The scope is also to highlight the novelty and importance of the presented work, which emphasizes on the photostrictive effect induced by laser illumination in the PMN-PT/FM heterostructure and its effect on the Ni thin film via inverse magnetostriction mechanism. Concerning the thermal treatment effects on multiferroic heterostructures, this aspect was characterized on PMN-$_{0.4}$PT/Fe heterostructures. The study was done by combining structural, magnetometric, and spectroscopic characterizations. X-ray diffraction (XRD) and micro-Raman spectroscopy were used to characterize the structural properties of PMN-PT substrate, whereas MOKE magnetometry was performed to analyze the in-plane magnetic response of Fe thin films deposited on top. The pristine unannealed substrate exhibited a larger presence of out-of-plane FE domains, with broad

and inhomogeneous features in the 2D reciprocal space maps of XRD, signifying the presence of a low crystalline quality of the ferroelectric structure. Once annealed for 15 minutes above the first-order phase transition, the majority of the domain population shifted towards the in-plane direction, showing in addition an overall improved crystalline quality. Further annealing led to a return to a mostly out-of-plane domain population. These structural modifications of PMN-PT upon annealing tailored the magnetic anisotropy of Fe film in different manners, exploiting the magnetoelastic interfacial coupling. Specifically, the angular dependence of the magnetic response of Fe passed from an isotropic one in the pristine case to an anisotropic one after short annealing, due to the larger presence of in-plane tetragonal domains. These results place thermal treatments as an additional parameter to be exploited for tuning the magnetic properties of multiferroic heterostructures. The results obtained with the two presented external stimuli, i.e., light illumination and thermal treatments, exploit the rich set of properties of ferroelectric materials and pave the way for further investigations, either by combining them or by further optimizing the choice of materials.

In this introductive chapter, the focus will be on explaining the ferroelectric and ferromagnetic materials that are constituents of a multiferroic heterostructure and their respective phenomenology's. The most general concepts are presented and coupling mechanisms in a multiferroic is discussed, linking the bridge between different order parameters like electric polarization of ferroelectric substrate and magnetization of a thin film deposited on top. The field of optical control of magnetism and multiferroic heterostructures has been expanding continuously in the recent years, and many recent review articles summarize the state of the art. These references will be used in this chapter in order to better understand the results found within the thesis.

Chapter 1

Scientific Background

1.1. Ferroelectric materials

Ferroelectricity is a property of a class of materials that exhibits a spontaneous electric polarization that can be reversed by the application of an external electric field.[1,2] The scientific research in the field of ferroelectricity has experienced a renaissance in the past decades driven by the discovery of new classes of ferroelectrics with enhanced properties, advances in first-principles theoretical techniques and an expanded range of applications. Great advances have been made so far in tuning the structural properties and related properties of bulk and thin-film ferroelectrics – a development that has been key to the progress in ferroelectric memories.[3]

Ferroelectric materials present specific structural properties, being a subgroup of piezo and pyroelectric materials (Figure 1). In a more general approach, the structural symmetries of a crystal affect a series of physical properties, such as dielectric, elastic, piezoelectric, ferroelectric, non-linear optical properties. The piezoelectric effect was discovered by Jacques Curie and Pierre Curie in 1880 in polar crystals exhibiting spontaneous polarization.[4,5] The crystals having a unique rotation axis, but does not have any mirror perpendicular to this axis thus showing different atomic arrangement at the two extreme ends are known as polar crystals, and it is required to exhibit piezoelectric properties. Piezoelectricity is the ability of a dielectric material to convert mechanical energy into electrical energy and vice versa. The two types of piezoelectric effects are direct and converse effects i.e., generation of internal electric field due to applied stress or mechanical strain/stress induction due to application of an electric field, respectively. According to Neumann's principle,[6] symmetry elements of all physical properties in a crystal should include all symmetry elements of the point group of this crystal. Thus, if a physical parameter is subjected to a symmetry operation of this crystal, the value of this physical parameter should remain invariant. Structural symmetry of a crystal depends on its lattice structure. The lattice structure is described by Bravais unit cell of the crystal. Among all possible crystalline structures, only 32 present macroscopic symmetry types (32-point groups). Out of 32 macroscopic crystal classes (point groups), 11 are centrosymmetric and thus cannot exhibit polar properties. The remaining 21 lacks a center of symmetry (two opposite ends of a crystallographically unique direction axis cannot be made to coincide by any symmetry operation) and thus can possess one or more polar axes. Among all these non-centrosymmetric point groups, 20 classes out of them are piezoelectric (the one exception being cubic class) along a unique direction axis.

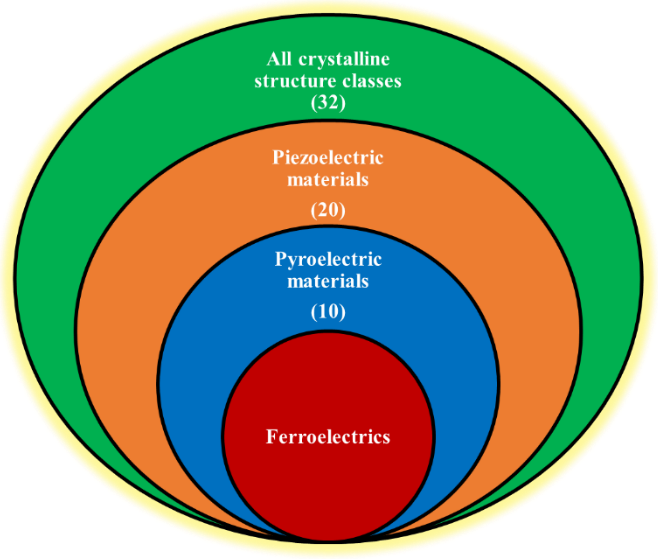

Figure 1: The hierarchy relationship among dielectric, piezoelectric, pyroelectric and ferroelectric materials.

Out of these 20, 10 classes have a unique polar axis and thus are spontaneously polarized, *i.e.* polarization in absence of an external electric field (these as called as pyroelectric crystals). The intrinsic polarization of pyroelectric crystals is often difficult to detect experimentally because of the neutralization of the charges on the crystal surfaces by free charges from the atmosphere and by conduction within the crystal. However, since the polarization has temperature dependence, it is often possible to observe a net spontaneous charge in these crystals by changing the temperature, hence the name pyroelectrics. Ferroelectric crystals are a subgroup of the pyroelectric family, since they exhibit as additional property the possibility of switching the direction of the spontaneous polarization by the application of an electric field. Thus, a ferroelectric material can be defined as "*a material that possess reversible spontaneous polarization as exhibited by a dielectric hysteresis loop"*.[3] The relation between the external electric field (E) and the polarization (P) is represented in Figure 2, and presents several analogies with the magnetic hysteresis loop that will be described in section 1.2 of ferromagnetic materials. Ferroelectricity was first discovered by Valasek in Rochelle salt in 1921.[7] From a physical point of view, in a virgin macroscopic crystal, it is unlikely that the direction of the polarization will be the same throughout. It is energetically more favorable for the crystal to break into macroscopic regions with uniform alignment of electric dipoles and homogeneous polarization, known as ferroelectric domains. The interface between two domains is known as domain wall and the polarization reversal can take place by nucleation of new domains and motion of these domain walls. Concerning P-E loops, if we first apply a small electric field on a depolarized ferroelectric material, there will be a linear relationship between P and E (Point A). As the electric field strength increases, a number of domains will align along the direction of the applied electric field and the polarization will increase until all the domains are aligned (Point B). This is a state of saturation in which the crystal presents the highest value of polarization, which can be modeled as a single ferroelectric domain. As we decrease the field strength, the polarization will partially decrease, without going back to zero. At zero applied electric field, some of the domains will remain aligned and the crystal will exhibit a net remanent polarization (Point C). This remanent polarization state cannot be removed until the field is applied in the opposite direction, reaching to a certain electric field value (Point D). The strength of the field thus required to reduce the polarization to zero is called the ‘‘coercive field strength’’. Further increase of the field in the negative direction will cause a complete alignment of the dipoles in this direction (Point E) and the cycle can be completed by reversing the field direction once again.

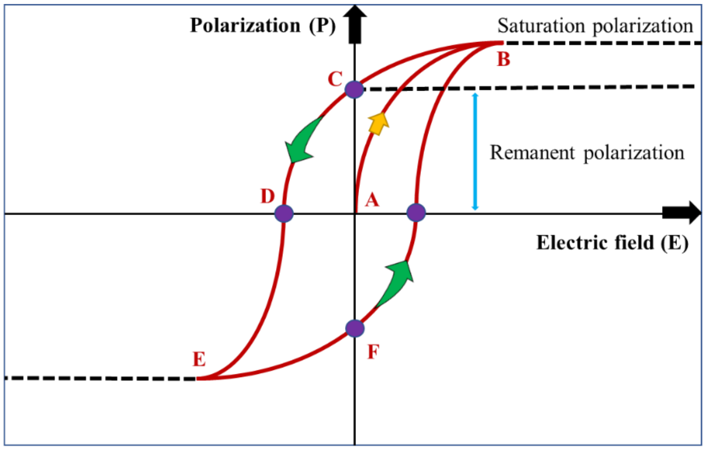

Figure 2: Typical polarization versus electric field (P-E) hysteresis loop of ferroelectrics.

Although ferroelectric crystals are a widely varied group, they possess a number of general characteristic properties, which are listed here below:

- The hysteresis loop disappears above a certain temperature of phase transition, known as Curie point (T_C), above which the crystal behaves as a dielectric material. It should be worth mentioning that in some crystals melting or chemical decomposition may occur before reaching the Curie point (e.g., the FE polymer PVDF). Above T_C, a ferroelectric crystal modifies its crystalline structure to a phase of higher symmetry, becoming non-polar or paraelectric, *i.e.* exhibiting no ferroelectricity.
- The polar crystal structure of a ferroelectric can be derived from the high temperature paraelectric structure by a slight distortion of the crystal lattice. This is the main reason behind the success of the phenomenological theory of ferroelectricity which assumes that the same free energy function is applicable for both the ferroelectric and paraelectric phases.
- Ferroelectric materials generally have large electric permittivity (ε) and susceptibility (χ), which rises to a peak value at the Curie point.
- Above the Curie point, the permittivity of a ferroelectric material (measured along the polar axis) usually obeys the Curie-Weiss law. It is represented by $\varepsilon = \frac{C}{T-T_c}$, where C and T_C are the Curie-Weiss constant and Curie-Weiss temperature, respectively.

Nowadays, ferroelectricity lead to the development of new kind of ferroelectric materials composed of inorganic elements such as Barium Titanate [$BaTiO_3$] or Lead Zirconate Titanate $Pb[Zr_xTi_{1-x}]O_3$ (PT). Both of these ferroelectric oxides belong to the family of perovskites with the generic formula of ABO_3. In the idealized cubic unit cell of such a compound, the type 'A' atom sits at cube corner position (0, 0, 0), the type 'B' atom sits at the body-center position (1/2, 1/2, 1/2) and oxygen atoms sit at face centered positions (1/2, 1/2, 0), (1/2, 0, 1/2) and (0, 1/2, 1/2). The diagram of (figure 3a) shows edges for an equivalent unit cell with A in the cube corner position, B at the body center, and O at face-centered positions. According to the radius of A and B ions, the whole structure distorts from the ideal cubic phase by stretching and tilting the oxygen octahedron or by displacing the ions (see figure 3b,c). These distortions induce an asymmetry in the lattice, leading to an unbalanced charge configuration and hence resulting in the formation of electric dipole moments. Whenever an external electric field is applied through the thickness of the ferroelectric, it aligns the neighboring dipoles leading to a static bound charge at the surface.

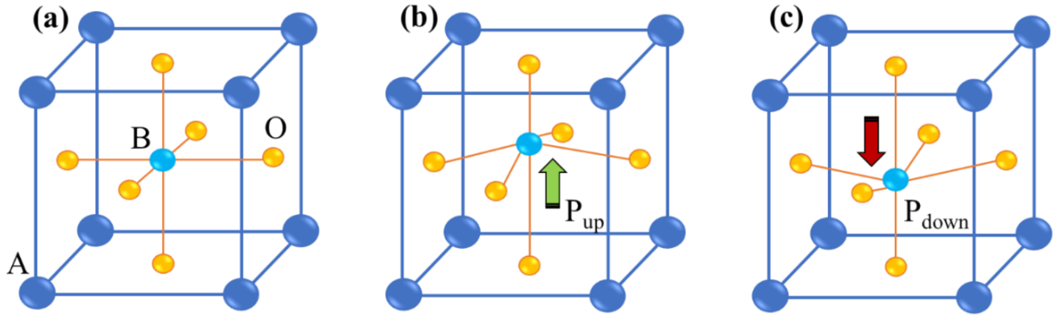

Figure 3: (a) Generic structure of ABO3 perovskite unit cell. In ferroelectric materials, the atomic displacement of B atom induces a spontaneous polarization, see for instance **(b)** and **(c)** for two opposite polarization states.

Apart from the applied external field, mechanical strain/stress and temperature can also change the net polarization in ferroelectrics, therefore modifying its properties. Conversely, the applied electric field can modify the mechanical properties of the ferroelectric, known as converse piezoelectric effect. In ferroelectrics, it is difficult to find an exact relationship between strain and electric field, since the coexistence of electrical switching and movement of ferroelectric domain walls, together with the non-volatile behavior of the polarization, makes the whole picture of the interconnection between the two quite complex.

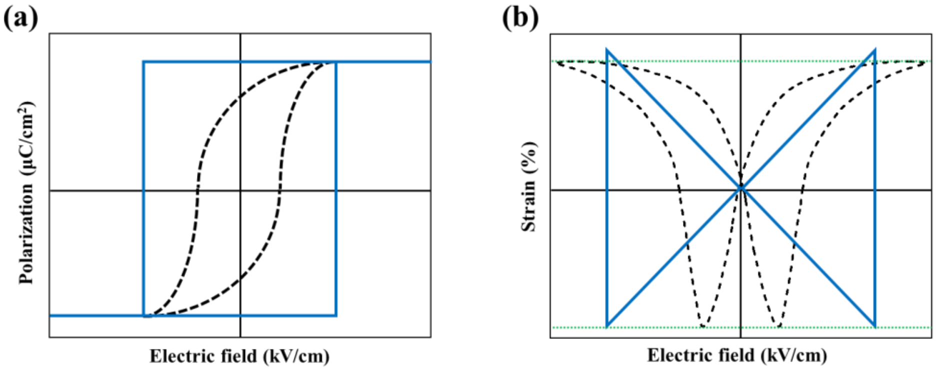

Figure 4: (a) Polarization and **(b)** strain curves under an electric field of a typical ferroelectric material. Solid blue lines are the loops of an ideal monodomain crystal, while blacked dashed curves are sketches of what is usually observed experimentally.

If we consider a monodomain ferroelectric single-crystal, its net polarization is reversed instantaneously by an electric field when overpassing a critical applied electric field, as shown in the blue P−E curve of figure 4a. This curve considers the squared non-volatile hysteresis loop of the polarization. In a real case, the presence of ferroelectric domains leads to a smoother reversal of the polarization under electric field, giving typical hysteresis loops as the dashed black line of figure 4a.

Strain curve of ideal monodomain ferroelectric is shown in figure 4b, as the electric field is increased, the stretching of oxygen octahedron gives changes in the lattice parameter of unit cell, hence modulating the domain size and resulting in a uniform strain. But in reality, the presence of multiple ferroelectric domains affects the strain, resulting in a "butterfly-like" loop, as shown by the black line in the same figure 4b.

Ferroelectric materials respond to a number of physical external stimuli which modify their properties (figure 5).[8] Here they will be briefly listed and described.

As previously shown, ferroelectrics are a subclass of pyroelectric materials. Pyroelectricity describes the generation of generation and accumulation of the charges at the surface (temporary voltage generation) during a temperature variation, either during heating or cooling (figure 5a).[9] If the temperature is raised to T_C, a ferroelectric-to-paraelectric phase transition occurs and polarization decreases to zero.

The piezoelectric effect (figure 5b), that includes a larger class of materials than the pyroelectric one, is the accumulation of charges at the surface when subjected to directional mechanical stress, with a resulting induced electric field.[10] Conversely, inverse piezoelectricity means that a mechanical stress develops in response to an applied electric field (figure 5c). In addition to the above-mentioned mechanisms of ferroelectric material interacting with heat, force, and electric fields respectively, light interaction of ferroelectric can also produce several effects, such as photovoltaic, acousto-optic, and electro-optic properties, giving rise to non-nonlinear optical effects in the material.[2,11,12] Nonlinear optics in ferroelectric materials is the ability to efficiently generate multidirectional second or third harmonic generation (SHG or THG) for a variety of geometries over a wide spectral range. For example, the SHG process is a second-order nonlinearity in which two photons of frequency (ω) interact with certain asymmetric materials and combine to produce a new single photon of twice the frequency (2ω) of the two incident photons (figure 5d).[13] In nonlinear optical microscopy, SHG relies on two photons hitting the same spot simultaneously. Therefore, SHG uses pulsed lasers in the near-infrared wavelength range, which can reduce non-specific phototoxicity and improve penetration of photons.[14] In the case of continuous illumination, whenever a ferroelectric material is illuminated with a light of photon energy higher than the band gap of material ($h\nu > E_g$) it shows photovoltaic effect, *i.e.* generation of electron-hole pairs separated spontaneously by the built-in electric field induced by intrinsic polarization of the material giving rise to a photocurrent and photovoltage (figure 5e).[15–17] Going one step forward, the combination of photovoltaics and inverse-piezoelectric effect in a ferroelectric material results in another successive phenomenon known as ‘‘photostriction’’, which gives non-thermal changes in the size of material upon exposure of light.[18,19] This effect will be discussed in details in the next section.

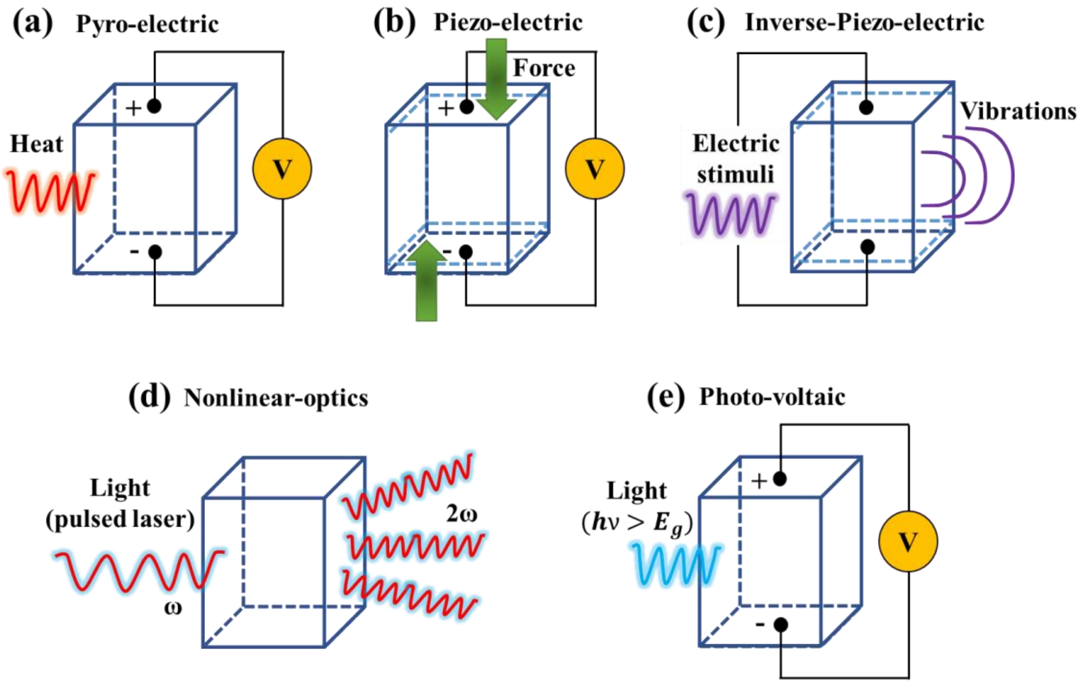

Figure 5: Unit cell of a ferroelectric material interacting and responding to external stimuli, **(a)** pyroelectric effect (generation of electric charges upon variation of temperature), **(b)** piezoelectric effect (applied force resulting in charge generation), **(c)** Inverse piezoelectric effect (induced-strain/mechanical vibrations under external voltage), **(d)** non-linear (generation of harmonic photon upon exposure to a pulsed laser) and **(e)** photo-voltaic effect (above-band gap photovoltage generation by light).

1.1.1. Photostriction mechanism in ferroelectrics

Shape responsive solids that are sensitive to a variety of external excitations upon variation of environmental conditions constitute an important class of functional materials.[20] Among-them, light-induced ferroelectric control is a particularly intriguing one and not fully explored yet. The effect of light-matter interactions resulting in non-thermal shape deformation is known as photostriction (figure 6),[18] The photostriction mechanism in ferroelectrics can be defined as photo-induced deformation of the lattice associated with a change in the internal electric field, leading to a converse piezo-response in the photo-ferroelectric compound. In order for this to happen, photostrictive effect is a superposition of the bulk photovoltaic effect (BPVE) and converse piezoelectric effect,[19,21] resulting in an expansion or contraction of the ferroelectric material. The BPVE is a distinctive class of photovoltaic effect that occurs in solids with broken inversion symmetry and refer to the generation of current by uniform illumination.

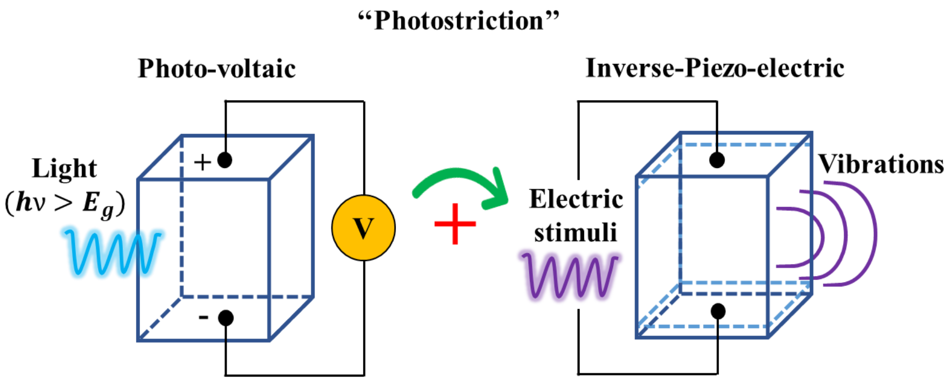

Figure 6: Photostriction mechanism of a unit cell of ferroelectric material upon exposure of light, which is the result of the combination of photovoltaic and inverse-piezoelectric effects.

The discovery of photostriction in electrically polar compounds dates back to the sixties, when Tatsuzaki *et al*. reported a photo-induced strain in single crystal of SbSI.[22] The effect was also found to be wavelength dependence with amonotonous dependence. This unexpected wavelength dependence photostriction in ferroelectric material results from two competitive contributions: electric field redistribution, leading to increment of electric field, and electric field screening by the light induced charge carriers, leading to decrease of electric field strength in the material. This assumption was in agreement with the Landau free energy expansion analysis with two competing contributions: the first one being proportional to the square of polarization, while second one being proportional to the average light-induced charge concentration.[23] The simple empirical formula for linear photostriction as a function of time *(t)*, piezoelectric coefficient d_j, and light-induced electric field in the material E_j can be written as[24]:

$$\lambda_{h\nu} = \frac{\Delta L}{L} = d_j E_j \left(1 - e^{-t/_{RC}}\right), \tag{1}$$

where, R and C are resistance and capacitance of the sample. For $t \ll 1$, one can write

$$\frac{\Delta L}{L} \cong d_j E_j \left({}^{t}/_{RC}\right), \tag{2}$$

where low dielectric permittivity (capacitance) is preferable to have faster response speed. A large piezoelectric coefficient and large internal electric field (polarization) is required for optimizing photostriction effect. While equation (1) is enough to describe qualitatively the photostriction and its response time dynamics at saturated electric state, it also assumes that piezoelectric coefficient is light independent, which is not always the case. An analytical description that includes strain effects involves some additional terms in describing the generation of light-induced charges $\sum_j n_j\, \varepsilon_j \Omega_j$ to the free energy *(F)* of the system, which can be written as[23]:

$$\boldsymbol{F} = \frac{1}{2}\alpha P^2 + \frac{1}{2}\beta P^2 + \frac{1}{2}\gamma P^6 - \frac{1}{2}\sum_i \sum_j k_{ij}\Omega_i \Omega_j - P^2 \sum_j \xi_j \Omega_j + \sum_j n_j \varepsilon_j \Omega_j, \tag{3}$$

where, $k_{ij} = \partial^2 F / \partial\Omega_i \partial\Omega_j$ are components of the elastic stiffness tensor. Ω_{ij} is the strain tensor. $\xi_j = \partial^3 F / \partial P^2 \partial\Omega_j$ is the electrostriction tensor. If we talk about relaxor ferroelectrics, they are a special category of ferroelectric materials that possess high dielectric constants and large electrostriction. The macroscopic response of relaxor ferroelectrics resembles nonlinear paraelectrics, and the hysteresis is suppressed at sufficiently high temperatures, or with suitable doping of materials. α, β, and γ are the known coefficients of ferroelectric free energy expansion. n_j is an average concentration of electron subsystem charges at the energy levels ε_j (conduction band levels of traps and recombination) close to the bandgap energy. Now, taking the derivative with respect to the polarization, which is the internal electric field, one can estimate

$$\frac{\partial F}{\partial P} = \alpha P + \beta P^3 + \gamma P^5 - 2P \sum_j \xi_j \Omega_j = E_j \tag{4}$$

The components of the deformation tensor τ_j can be defined as $\partial F / \partial\Omega_j$

$$\frac{\partial F}{\partial \Omega_j} = -\frac{1}{2}\sum_i k_{ij}\, \Omega_i - P^2 \xi_j + \sum_j n_j \varepsilon_j = \tau_j \tag{5}$$

Putting $\Omega_i = 0$, we can get

$$\tau_j = \sum_j n_j \varepsilon_j - P^2 \xi_j \tag{6}$$

This equation depicts that deformation does not depend on the sign of polarization as it was expected and should be varied in presence of light-induced charges. Notably, this equation of free energy shows that the photostriction (Eq. (1)) itself has two competing contributions: one from the direct change in polarization and another from the light induced charge carriers. Indeed, in ferroelectrics, both the piezo and electro-strictive effects are present, therefore an interplay together with the movement of charged domains at low electric fields can lead to multilevel hysteresis behavior in both bulk and surface effects and to include it, the theory must be protracted.

On the other hand, the piezoelectric coefficient determined from Eq. (1) using Eqs. (4) and (6) will become

$$d_j = \frac{\sum_j n_j \varepsilon_j - P^2 \xi_j}{\alpha P + \beta P^3 + \gamma P^5 - 2P \sum_j \xi_j \Omega_j} \tag{7}$$

Given that photostriction differs intrinsically from compound to compound and depends on the thickness and light irradiance, one can estimate a photostrictive efficiency at the given wavelength as

$$\boldsymbol{\eta_{eff}} = t * \frac{\lambda_{h\nu}}{I}, \tag{8}$$

where, *t* is the thickness along the illumination direction, $\lambda_{\mathrm{h\nu}} = \Delta L/L$ is the linear photostriction and *I* is the irradiance of light.

1.1.2. PMN-PT specific properties

All the heterostructures realized during this PhD thesis were deposited on PMN-PT substrates. PMN-PT is the abbreviation for the relaxor photo-ferroelectric $[Pb(Mg_{1/3}Nb_{2/3})O_3]_{1-x}$–$[PbTiO_3]_x$, which is a single crystal combining different ratios of lead-magnesium-niobate (PMN) and lead titanate (PT). PMN-PT has emerged as a highly promising multifunctional system combining piezoelectric, pyroelectric, and electro-optic properties that surpass by far those other ceramics. Relaxor ferroelectrics are a kind of materials where the long-range ordering of dipoles is disrupted by cation disorder, possessing complex polar states with a significant amount of local structural heterogeneity at the nanoscale range.[25] Consequently, relaxor ferroelectrics have very high specific capacitance and have thus generated interest in the fields of energy storage and electro-strictive actuators. PMN-PT is a complex oxide with perovskite structure, where the A site is occupied by Pb^{2+}, B site by Mg^{2+}, Nb^{5+} or Ti^{4+} (figure 2a), where PMN has relaxor properties while PT ferroelectric one. Solid solutions of PMN and PT combine both electro-strictive and ferroelectric properties and exhibit different crystalline structures depending on the percent concentration (x) of $PbTiO_3$, together with a temperature dependence. Its phase diagram shows a tetragonal structure for x greater than 40% and a rhombohedral structure for PT composition being less than 30%, at room temperature[26] (see figure 7). The intermediate range (i.e. between 30 and 40%), known as the morphotropic phase boundary (MPB), is associated with the co-existence of both tetragonal and rhombohedral phases[27], giving abnormally high dielectric response and giant electromechanical properties.[28] The nature of the MPB, still debated in literature, is generally attributed to a second order transition that accommodates the rhombohedral to the tetragonal transition thus allowing for easy rotation of the polarization vector. The Curie temperature T_C also varies as a function of PT composition. Above T_C the material modifies its structure into cubic, becoming paraelectric.

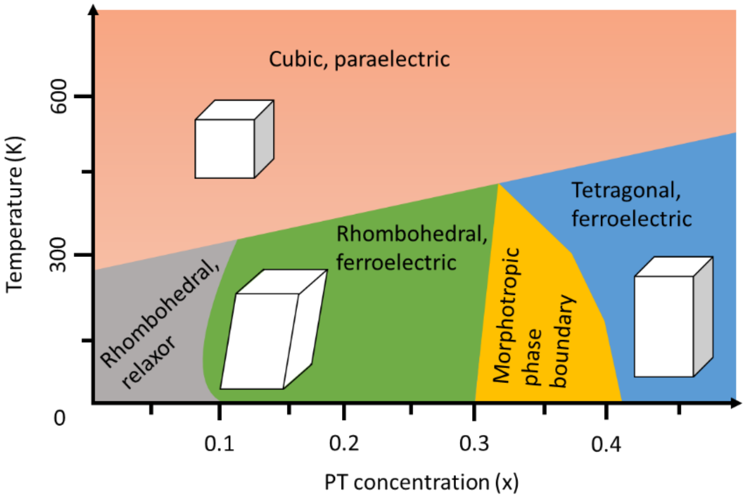

Figure 7: Schematic representation of phase diagram of $PMN_{(1-x)}$-$_x$PT material. [F. Motti et. al., *Phys. Rev. Mater.* **2020**, 4, 114418][29]

The crystalline structure plays an important role in the orientation of polarization vector under the application of an external electric field. In the tetragonal phase (PT content larger than 40%) the spontaneous polarization is aligned parallel to the long side of unit cell. In the rhombohedral case, the polarization vector aligns along any of the ⟨111⟩ pseudo-cubic directions. Under the application of an out-of-plane reversible electric field strength (‘‘up’’ or ‘‘down’’) being perpendicular to (001) plane, three possible domain orientation can be obtained: at 71°, 109°, or 180° from the initial polarization direction, as shown in figure 8.

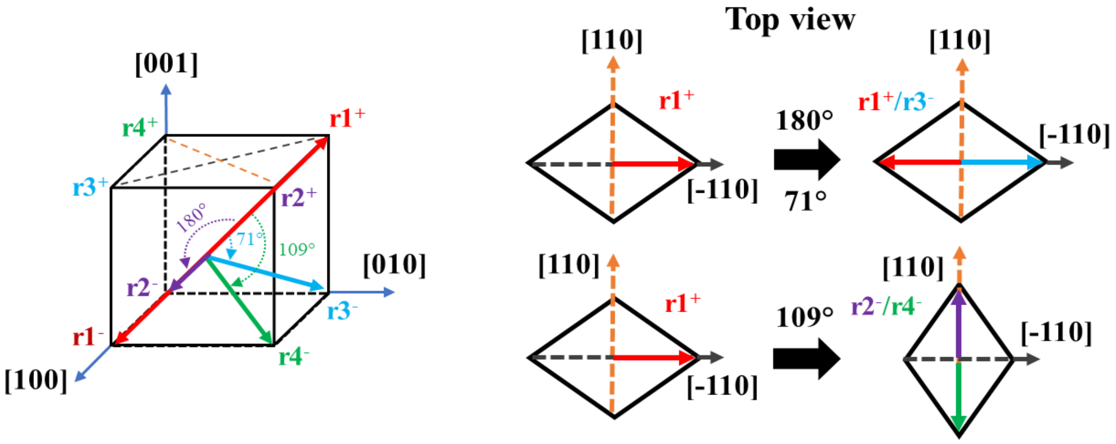

Figure 8: Simplified Rhombohedral unit cell of a ferroelectric material depicting three possible switching polarization vector directions. The out of plane component of the polarization vector can be reversed in three different ways. If we consider the in-plane component along $r1^+$, polarization switching lead to a rotation along one of the four corner $r1^-$, $r2^-$, $r3^-$, and $r4^-$, giving rotations of 109° along $r2^-$ and $r4^-$ that changes the strain in-plane while for 180° or 71° it remains unchanged, hence no strain is induced (Top view).

If the polarization rotates of an angle of either 180° or 71°, the in-plane component remains unchanged, giving no modification of the lattice parameters, therefore this rotation is strain-symmetric and will not lead to interfacial strain on multiferroic heterostructures. In the case of 109° switching of ferroelectric domains, the lattice parameters are modified, and therefore a variation of strain takes place at the interface with the ferromagnetic material on top of it. This rotation is considered to be the responsible for the non-volatile strain-induced magnetoelectric effects that observed in PMN-PT/FM heterostructures.[30,31]

Nowadays, several works showed that is favorable to avoid the strain-driven interfacial modifications because of fatigue induced by the polarization switching and consequently the deterioration of the ferroelectric properties. For this reason, optical-based process using photostriction effect have gained attention. Several studies have focused on photostrictive effects in different ferroelectric materials and thin films, for example $Pb_{(1-x)}La_x(Zr_yTi_{(1-y)})_{(1-x/4)}O_3$ (PLZT),[32,33] $BiFeO_3$ (BFO),[34] and $BaTiO_3$ (BTO),[35] but the renewed attention is currently devoted to $PbTiO_3$ compounds. In PMN-PT crystals, the PT concentration impacts directly the optical properties of PMN-PT crystals, with the refractive index and band gap energy increasing with the increase in PT content. Also, the electric field and temperature-controllable photovoltage (exhibiting different crystalline structures) in this landmark ferroelectric crystal should be regarded as the key finding to understand and optimize the photoferroelectic performance.[36]

1.2. Ferromagnetic materials

Ferromagnetic materials are a class of compounds exhibiting an asymmetry in the spin population. The term "ferromagnetism" comes from observation of a net magnetic signal coming from magnetite (Fe_3O_4).[37], Ferromagnetic compounds exhibit spontaneous parallel alignment of permanent dipoles due to the movement of electrons around atomic orbitals except in the case of coupling between rare-earth and magnetic transition metal where spins are always antiparallel. Pierre-Ernest Weiss discovered the structural arrangement of dipoles in ferromagnets.[38] These arrangements generate high magnetization even in the absence of a magnetic field, but in microscopic spaces called domains. These domains are not aligned, so the ferromagnetic compounds themselves do not act as magnets. However, when exposed to an external magnetic field, these domains align in different directions and maintain a specific orientation, generating transient magnetic fields within the material. Ferromagnetic materials include alloys formed from transition metals Co, Ni, and Fe, rare earth materials, plus some classes of metal oxides.[39]

1.2.1. Magnetic energies of a magnetic material

A ferromagnet can be described at different level of complexity as a function of the scale of the system. Regarding a single atom, the interaction energy of the magnetic moment *(μ)* with a magnetic field strength (**B**) is expressed using the hamiltonian: $H_{magn} = -\mu.\mathbf{B}$, where μ contains the orbital and spin angular moment dependencies. For condensed matter, where individual atoms interact, there are some additional terms to consider. In 1935, L. Landau and E. Lifschitz described the total free magnetic energy as the sum of various contributions: [40]

$$\boldsymbol{E = E_{exc} + E_D + E_\lambda + E_{anis} + E_Z} \tag{9}$$

where each term represents:

- ❖ E_{exc} is the **exchange energy** coming from the short range ordered interaction, responsible for the parallel alignment of the spin dependent density of states. This kind of interaction results from the Pauli exclusion principle representing one of the bases of a quantum mechanical interpretation for magnetism in solids. It can be formulated and explained using the Heisenberg exchange Hamiltonian:

$$\boldsymbol{H_{exc}} = -\sum J_{exc} S_a . S_b \tag{10}$$

where, J_{exc} represents the exchange constant (having a positive value for ferromagnetic materials) and S_a and $S_b$are the atomic spins.

- E_D corresponds the **magnetostatic dipolar energy** for the magnetic material associated to the demagnetizing field H_d created intrinsically by the material upon being magnetized, in the opposite direction of magnetization M. This demagnetizing field is mainly responsible for shape anisotropy, particularly relevant in nanopatterned thin films. The magnetostatic energy can be written as:

$$\boldsymbol{E_D} = \frac{\mu_0}{2} \int_V \boldsymbol{M} . H_D dV \tag{11}$$

This expresses a long-range interaction and describes the influence on each spin of the magnetic field generated by all the other spins in the material.

- E_λ represents the **magnetoelastic energy** and is linked to the effect of magnetostriction in materials. Magnetostriction is the modification in dimensions of the material induced upon magnetization. It can be expressed as:

$$\boldsymbol{E_\lambda} = \frac{3}{2} \lambda_S \varepsilon \cos^2 \theta \tag{12}$$

here, ε is the stress or strain induced in the material, θ corresponds to the angle between magnetization and the direction of uniform stress and λ_S is the saturation value of magnetostriction constant, for instance in the case of iron the value of saturation constant is positive ($\lambda_S = 24 \times 10^{-6}\, Jm^{-3}$) along the (100) crystallographic direction and negative ($\lambda_S = -23 \times 10^{-6}\, Jm^{-3}$) along (111) direction. [38]

- E_{anis} is the **anisotropic energy** originating due to the magneto-crystalline anisotropy of the material. For the case of material having uniaxial magnetism (exhibiting only one easy axis), the anisotropic energy can be formulated as:

$$\boldsymbol{E_{anis}} = -K_{anis} \cos^2 \theta \tag{13}$$

where, $\mathrm{K_{anis}}$ is a positive constant that depends on the considered volume and θ is the angle between magnetization and crystallographic direction of the easy axis of material. For systems having different symmetric conditions, this expression has to be modified with additional terms.

- E_Z is the **Zeeman energy** that is responsible for the alignment of the spin dependent population in accordance with the direction of applied magnetic field. It can be written as:

$$\boldsymbol{E_Z} = -\mu_0 \int_V \boldsymbol{M} \, . \, \boldsymbol{H} dV \tag{14}$$

where, μ_0 is the permeability in vacuum, **M** is the magnetization of the material, **H** is the applied magnetic field strength and V is the considered volume. When the magnetization M is parallel to the direction of applied field H, the Zeeman energy is minimized. The density of magnetic field determines the amount of spins orientated in that direction.

For a single-domain ferromagnet, the most relevant energy terms are E_{anis} and E_Z, as depicted by the Stoner-Wohlfarth model. On the other hand, for a multi-domain system, magnetocrystalline (E_D) and exchange (E_{exc}) energies are linked to the energy minimization leading to the creation of magnetic domains and domain walls.

A description of ferromagnetism in transition metals is provided by the Stoner band model (figure 9), which identifies key features in the spin polarization of the d-bands.[41] According to this model, the electrons responsible for ferromagnetism are itinerant and not localized to atomic positions, this is attributed to the presence of repulsive interaction. Let us consider, a simple model with an on-site repulsion of energy cost $\boldsymbol{U}$ in case of two electrons occupying the same quantum state. Now, Pauli exclusion principle states that two or more fermions cannot occupy the same quantum state within a quantum system simultaneously (i.e., they need to have opposite spins). Thus, in case of transition metals with an incomplete 3d shell, due to exchange interactions the d-bands separates into two, the so-called majority and minority bands with opposite spin direction with respect to each other (figure 9b). The bands of the transition d-metal are partially filled, resulting in an inter-band spin imbalance responsible for the net magnetization.

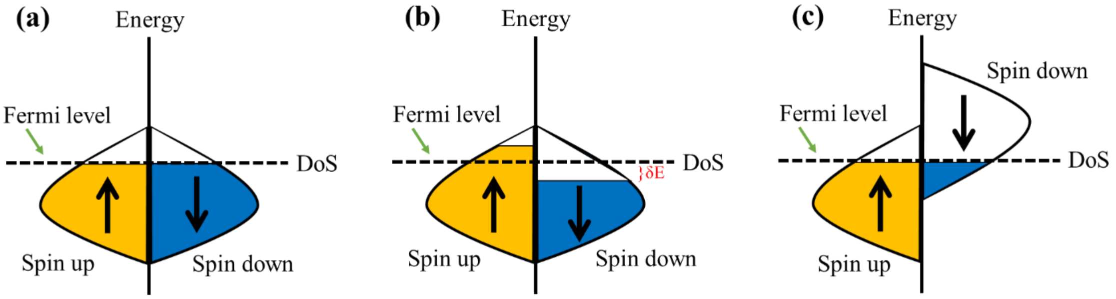

Figure 9: Schematic band structure for the Stoner model of ferromagnetism: **(a)** spin balanced condition of a paramagnetic material; **(b)** exchange interaction determining the spin-splitting of majority and minority sub-bands; **(c)** The difference in spin polarized DoS at Fermi level of ferromagnets.

With this in mind, let us consider a state in which $\boldsymbol{\delta n}$ number of down-spins flip spontaneously. Then, the number of up-spins, denoted by $\mathbf{N}_\uparrow$ will be $\mathrm{N}_\uparrow = n + \delta n$ and the number of down-spins is $\mathbf{N}_\downarrow = n - \delta n$. This restructuring of the spins leads to a modification in the energy of system. The potential energy of the system will be given by $\boldsymbol{U_E} = U_{\mathrm{N}_\uparrow \mathrm{N}_\downarrow}$ and the change in the energy can be written as,

$$dU_E = U(n+\delta n)(n-\delta n) - Un^2 = -\boldsymbol{U}(\boldsymbol{\delta n})^{\mathbf{2}} \tag{15}$$

while, the change in kinetic energy $(\boldsymbol{K_E})$ due to the δn spins occupying larger energy states can be expressed as $\boldsymbol{dK_E} = \delta n \times dE$. The density of states (DoS) that can be defined as number of states in the energy interval $[E,\ E + dE]$ (*i.e.* the energy difference between the highest and lowest occupied single-particle states in a quantum system) will be,

$$\boldsymbol{D}(\boldsymbol{E}) = \frac{dn}{dE} \tag{16}$$

Since, population modification occurs near the Fermi level, the change in number density δn and the change in energy dE can be related to the density of states at the Fermi level as $\boldsymbol{\delta n} = \boldsymbol{D_F dE}$. Thus, the change in kinetic energy can be written as,

$$dK_E = \frac{1}{D_F}(\delta n)^2 \tag{17}$$

Hence, the change in total energy is the sum of modulation of kinetic and potential energies, it can be formulated as,

$$\begin{aligned} \boldsymbol{dE_T} &= dK_E + dU_E \\ &= \frac{1}{D_F}(\delta n)^2 + (-U(\delta n)^2) \\ &= \boldsymbol{\frac{(\delta n)^2}{D_F}}[\boldsymbol{1 - D_F U}] \end{aligned} \tag{18}$$

The above equation provides the Stoner criterion for itinerant ferromagnetism and can be expressed in case when $D_F U = 1$ i.e., $\boldsymbol{dE_T = 0}$, the system can lower its energy by creating an imbalance in the number of up and down spins, thereby becoming ferromagnetic. If the total energy is zero, the system is paramagnetic.

Whenever ferromagnets are subjected to external magnetic field strength (H), its net magnetization may be modified. The relation between H and the magnetization (M) is not univocal and it depends on the magnetic history of the material, i.e. ferromagnetic materials break time-reversal symmetry. In analogy with the ferroelectric case, in figure 10 here we show the ferromagnetic hysteresis loop. In ferromagnets, the hysteretic phenomenon results in two effects: rotation of magnetization and changes in size or number of magnetic domains. The magnetization does not change within each domain, but through their nucleation and annihilation under magnetic field. Magnetic domains are separated by domain walls and the direction of magnetization rotates from the direction of one domain to the direction of the other domain. The shape of hysteresis loop strongly depends on the direction of applied magnetic field strength and magnetic anisotropy of material. There is an intrinsic preferential direction for domains to align within a magnetic material, it is called as the easy direction or axis. Therefore, if the magnetic field is applied along this easy axis, the area of the loop will be large and the shape will be squared, in a simplified single domain model (figure 10). The magnetization starts parallel to the magnetic field and rotates only when it becomes unstable and jumps in the opposite direction. Conversely, if the field is perpendicular to the easy axis, no such sharp jumps will occur. The magnetization rotates continuously from one direction to the other.

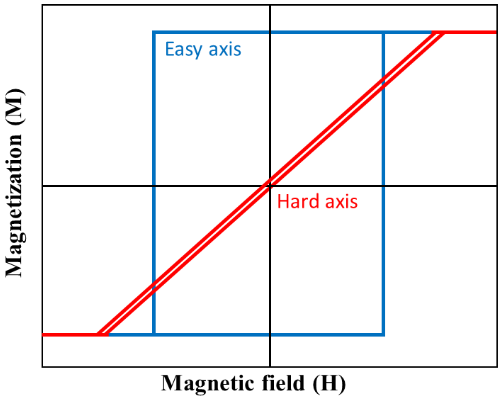

Figure 10: Two illustrative hysteresis loops for magnetic field being parallel to easy and axis hard axis of a ferromagnetic material.

The magnetic anisotropy in a ferromagnet is the result of three main contributions: Magnetocrystalline, Shape and Magnetoelastic anisotropy. The magnetocrystalline anisotropy results from the different crystalline structure and the physical origin lies on the spin-orbit coupling of electrons and its quenching by the crystal lattice. The atomic structure of the crystal determines the preferred direction of magnetization. On the other hand, shape anisotropy is related to the magnetostatic interactions occurring within the material and the boundary conditions that limit the volume of the sample. If the particle is not perfectly spherical, the demagnetizing field will not be the same in all directions, creating one or more easy axes. The magnetoelastic anisotropy is related to the external stress or strain imparted to the material by some force or tension leading to alternation of magnetic behavior. Other anisotropies can also be induced in certain materials by appropriate treatments such as magnetic annealing, strain, and plastic deformation.

1.2.2. Magnetostriction and magnetostrictive materials

Ferromagnetic material can change properties under the state of stress/strain; it naturally deforms when the deformation reduces the total energy (which is equal to the sum of the magnetic and elastic energies). This phenomenon is known as magnetostriction,[42] and the three magnetic energies give rise to bulk magnetostriction, linear magnetostriction, and form effect, respectively. Even if the lattice deformation produced by both exchange and anisotropy energies is zero, the material still exhibits magnetostriction due to the fact that demagnetizing energy is dependent on strain, it is known as form effect.[43] Since linear magnetostriction is the simplest and most commonly observed effect, most of this paragraph will be devoted to it. It has been observed that when a ferromagnetic material is magnetized, it exerts stress on its surroundings, and when released, its dimensions change. Applying Le Chatelier's principle,[44] a ferromagnet undergoing this effect can be expected to change its magnetization state when its dimensions are forced to change by an external stress. These two phenomena, the dimensional change induced by the change in magnetization and the change in magnetization under strain are both different aspects of the same thing, and understanding their fundamental properties is the basis of both theoretical and experimental studies. The magnetostriction curve for some common substances is shown in figure 11:

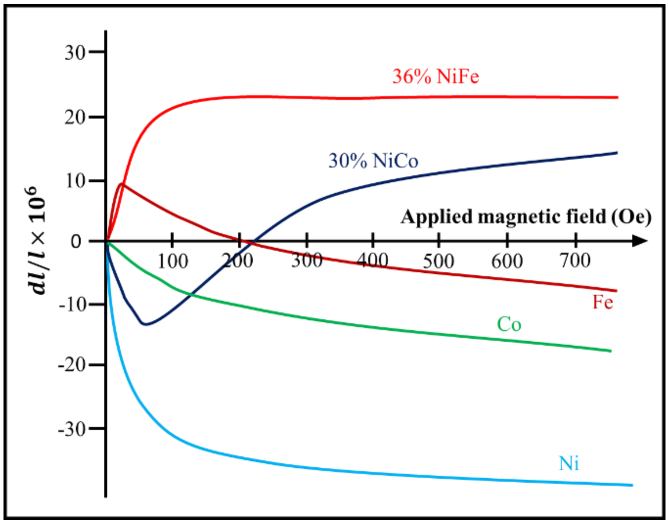

Figure 11: Magnetostriction trends of some common substances as a function of applied magnetic field. [E.W. Lee, *Rep. Progr. Phys.*, **1955**, 18, p. 184][42]

All magnetostrictive effects have the opposite effect. Longitudinal magnetostriction (also known as the Joule effect) is reversed in the Villary effect (Villary 1865),[45] a change in magnetization caused by an external strain. If we consider polycrystalline iron, the initial expansion occurs in the same field region where the domain boundary shift occurs. This expansion is followed by a gradual contraction at higher fields, starting at a magnetic field strength approximately equal to the ‘knee’ of the magnetization curve, i.e., the field strength at which the boundary shift is almost complete and the rotation process is just beginning. Contraction continues until rotation is complete and saturation magnetization and saturation magnetostriction are reached at the same field strength. During these processes, the volume of matter remains practically constant. At very high magnetic fields it expands further (in iron). This expansion is proportional to the strength of the magnetic field and differs in that at low fields magnetostriction occurs without volume change, whereas at high fields it is predominantly a volume effect and the expansion is equal in all directions. It is natural to associate this bulk strain with the increase in spontaneous magnetization induced by the magnetic field. It should be noted that we are dealing with two completely different magnetization processes. The first is simply to tune the magnetization vector of the domain, while the second requires increasing the spontaneous magnetization of the domain itself. The alignment process changes the direction of the domain magnetization vectors. The crystal orientation does not change. Therefore, it should be possible to describe the magnetostriction curves by assuming that below the Curie temperature all domains are spontaneously distorted by the spontaneous magnetization within each domain. The simplest assumption is that the stress within each domain varies only with the orientation of the domain magnetization with respect to a single fixed axis. This is the direction of the applied magnetic field and can be assumed to match the direction of observation. If the angle between the magnetization of the domain and this axis is θ, then $dl/l = f(\theta)$. The 180° change of θ should not change dl/l, i.e., wall motion does not produce any magnetostrictive change in dimensions, so the simplest form of dl/l is obtained by setting $f(\theta) = A\cos^2\theta$, where A is a constant for the material. It is common to measure magnetostriction from a hypothetical demagnetized state with dl/l arbitrarily set to zero. This hypothetical demagnetized state is defined as the state in which the domain magnetization vectors are evenly distributed in all possible directions within the sphere. The mean value of $\cos^2\theta$ for such a distribution is $1/3$. Hence,

$$\frac{dl}{l} = A(cos^2\theta - \frac{1}{3}) \tag{19}$$

The magnetostrictive saturation value is reached when $\theta = 0$ for all domain vectors. Thus, for a single domain case, we can write:

$$\frac{dl}{l} = \frac{3}{3}\lambda_S(cos^2\theta - \frac{1}{3}) \tag{20}$$

where, λ_S is a constant representing the total strain when the material is initially magnetized to saturation in a hypothetical demagnetized state. This means that magnetostriction can be described by a single constant. In particular, if the measurement direction is fixed and the material is saturated in each direction by applying a large magnetic field, the change in magnetostriction with the direction of saturation magnetization should be expressed by a simple $\cos^2 \theta$ curve. This holds fairly well for polycrystalline samples that do not exhibit preferred orientations of crystallographic axes.

According to Becker's calculations,[46] the magnetostriction constants for a body-centered lattice can be written as:

$$\lambda_{100} = \frac{2SI_s^2}{c_{11} - c_{12}}, \lambda_{111} = \frac{4}{3}\frac{SI_s^2}{c_{44}} \tag{21}$$

where, λ is the magnetically induced strain along respective crystallographic direction, I_S is the spontaneous magnetization equal to $N.\mu$, where N is the number of interacting dipoles per unit volume with moment μ, S is a constant dependent on the geometry of the crystal lattice, which is 0.4 for the body-centered and 0.6 for face-centered cubes and c_{11}, c_{12}, and c_{44} are representative elastic constants. While, for a face-centered cubic the constants are simply half of these.

Material	c_{11}	c_{12}	c_{44}	λ_{100}	λ_{111}	K_1	K^0	ΔK
	$dyn\ cm^{-2} \times 10^{12}$			$\times 10^6$		$ergs\ cm^{-3} \times 10^4$		
Fe	2.41	1.46	1.12	20.7	-21.2	+47	47.14	-0.14
Ni	2.50	1.60	1.185	-45.9	-24.3	5.9	-6.01	+0.11

Table 1: Values of magnetostriction constants for Iron and Nickel. Here, K^0 represents the unstrained crystal while ΔK refers to the anisotropy caused by magnetostriction and K_1 is the measured anisotropy (K^0+ ΔK).[42]

There are several factors affecting the magnetostriction constants including temperature, composition of alloys and crystallographic order in alloys, due to chapter length limits they are not explained here but can play a crucial role in modifying the magnetostrictive response of a material.

1.3. Multiferroic/Magnetoelectric materials

Long-range order in condensed matter is the origin of many functional properties of materials that fascinates researchers and have technological applications. Not surprisingly, much of the research effort to date has been devoted to discovering new states of matter and improving the properties of ordered matter.[47] One example is the emerging interest in a special class of material systems characterized by the simultaneous presence of magnetic and ferroelectric orderings, called magnetoelectric multiferroics.[48–50] By definition, a multiferroic material has coexistence of two or more primary ferroic order parameters in the same phase. They represent a much smaller subset of magnetic and ferroelectric systems, as they are systems that satisfy the requirements of both the presence of magnetism (time-reversal symmetry breaking) and ferroelectricity (space-reversal symmetry breaking) at the same time via magnetoelectric coupling.[51,52] Magnetoelectric effects have been extensively explored in some single-phase natural materials, in which ferromagnetism and ferroelectricity occur independently, but they are rare.[53] A well-known example of single-phase multiferroic is $BiFeO_3$, which is a ferroelectric-antiferromagnet at room temperature.[54–57] The canting of antiferromagnetically aligned spins via Dzaloshinski-Moriya (DM) interaction results in a weak ferromagnetism in BFO, [58–60] whereas in bulk crystals these canted magnetic moments are arranged in a cycloidal arrangement with a period of ~62 nm, leading to macroscopic magnetization cancellation.[61] Although, despite many years of intensive efforts on single-phase multiferroic materials, achieving controllable switching/modulation of substantial net polarization (magnetization) by magnetic (electric) fields remains a challenge, especially at room temperature. Therefore, applications of single-phase multiferroics in magnetoelectric devices remain a long-term goal.

On the other hand, compared with single-phase multiferroics, artificial multiferroic heterostructures integrating separately the magnetic and ferroelectric materials (or composite multiferroics) exhibit strong magnetoelectric effects at room temperature and flexibility in material selection. Their properties make them likely to be used in magnetoelectric devices in the near future. In multiferroic heterostructures, the magnetoelectric effect also depends on the coupling between the four fundamental degrees of freedom (spin, orbit, charge and lattice), but across the interface of the constituent magnetic and ferroelectric phases. The coexistence of spontaneous polarization (ferroelectricity) and spontaneous magnetization (ferromagnetism) enables the coupling between polarization (P) and magnetic field (H), known as **direct magnetoelectric effect** ($\mathit{\Delta} P = \alpha_H \mathit{\Delta} H$), where α_H is an effective coupling coefficient. Conversely, the coupling between magnetization (M) and electric field strength (E) is known as **converse magnetoelectric effect** ($\mu_0 \mathit{\Delta} M = \alpha_E \mathit{\Delta} E$), where α_E is an effective coupling coefficient and μ_0 denotes the vacuum permeability, the coupling mechanisms be seen in figure 12.

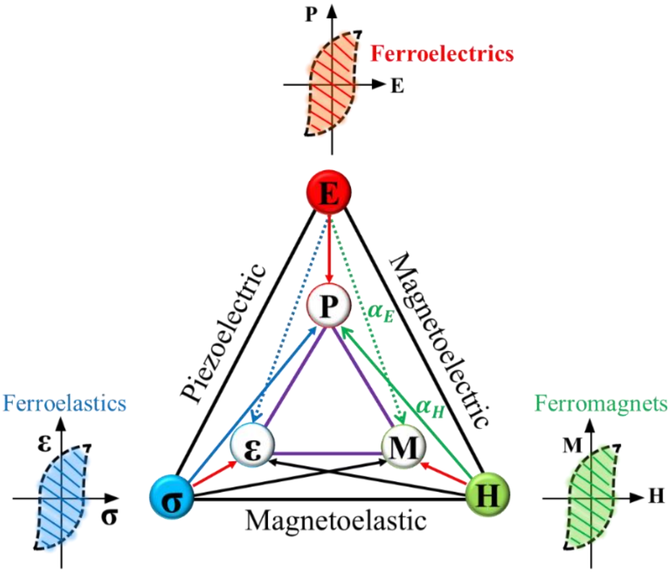

Figure 12: Schematics of coupling between elastic, magnetic and electric properties in multiferroic heterostructures, showing order parameters in outer-triangle and conjugate fields in in the inner-one. [J. P. Velev et. al., *Philos. Trans. R. Soc. A Math. Phys. Eng. Sci.* **2011**, 369, 3069][62]

1.3.1. Magnetoelectric coupling effects

It is important to understand the coupling mechanism between magnetism and ferroelectricity at the interface of a multiferroic heterostructures. Besides, interesting physical phenomena arising from the interfacial coupling between electric polarization and magnetization can lead to new functionalities at interfaces, it is reported that the magnetoelectric coupling in composite structures depends on interactions of charge, spin, lattice, and orbital degrees of freedom at the phase interfaces:[63] charge mediated effects (arising from electrostatic interactions), strain-mediated effects (this includes the transmission of stress across the interface), exchange-bias mediated effects (with changes in exchange interaction), and chemistry-mediated effects (movement of ions across the interface), as depicted in figure 13.

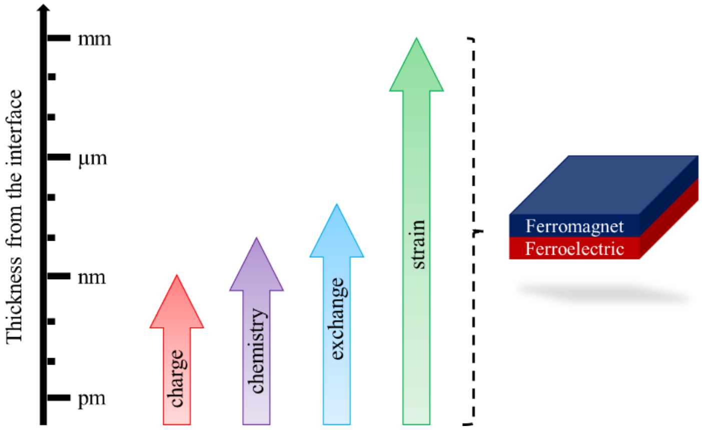

Figure 13: Typical length scales of various coupling mechanisms at interfaces between multiferroic heterostructures.

These phenomena have different characteristic length scales, but can often occur simultaneously. An important challenge is therefore to elucidate the different origins of the magnetoelectric coupling observed within the system. The mechanisms are explained below in brief:

- **Charge-mediated effects:** Whenever an electric field is applied, the electrons in the material experiences a force that changes the density in order to shield the external field. This re-arrangement results in the accumulation or depletion of electrons at the interface, and since charge carriers are also responsible for the magnetic properties of materials, field effects can in principle be used to manipulate magnetism. Since the electrons are spin-polarized, local changes in electron density at the Fermi level alter the magnetic properties at the interface. In metals, the free electron density is about 10^{22} cm^{-3} and the characteristic shield length is of the order of a single unit cell (about 3 Å for iron).[64] Therefore, significant magnetoelectric coupling can only be achieved on length scales below 1 nanometer,[63] confining it to the first atomic layer of the interface.

- **Chemistry-mediated effects:** These effect results through the movement of ions across the interface (electromechanics). This effect can occur at the oxide/ferromagnetic interface and is caused by chemical reaction between the metal and oxygen under the application of an electric field. This causes a reversible change in the chemical composition of the ferromagnetic material and hence, ion migration extends far beyond the interface and can affect the magnetic layer on the order of tens of nanometers.[63] As it has been reported that electric fields in systems such as Co/Gd_2O_3[65] and $NiCo/HfO_2$[66]

have induced reversible oxygen ion migration across the interface and also change magnetic properties such as saturation magnetization and magnetic anisotropy. A similar thing can happen in ferromagnetic oxides, whose properties can be strongly influenced by the presence of oxygen vacancies.

- **Exchange bias-mediated effects:** Exchange bias can occur in magnetic heterostructures composed of a multiferroic (ferroelectric and antiferromagnetic) part coupled with a ferromagnetic one. Exchange bias is a uniaxial coupling between ferromagnetic and antiferromagnetic layers, usually obtained after a magnetic field cooling procedure. In case of multiferroic/ferromagnetic heterostructures, the antiferromagnetic properties can be modified via electric field, thus changing the interfacial exchange bias.

- **Strain-mediated effects:** Among other coupling mechanisms, strain/stress transfer is the most efficient way to achieve magnetoelectric coupling. This is the only effect conditioning in macroscopic length scales, resulting in pronounced modulation of magnetic properties with external stimuli like visible light illumination and electric fields. It consists in using the piezoelectric properties of substrate to change the magnetization of metal film through inverse magnetostriction effect. The strain induced in ferroelectric substrate either by visible light illumination (photostriction) or under the application of an electric field propagates across the interface into the magnetic film, affecting the magnetic properties. The mechanism of photostriction and magnetostriction has been already discussed in section 1.1.1 and 1.2.2, respectively. The ferroelectric domain structure of substrate also plays an important role in strain-mediated effects. [67] The shape of the ferroelectric domains can be imprinted on the ferromagnetic domains, and the behavior under applied electric field (such as residual and transient effects) can strongly depend on the switching process of the ferroelectric domains.

- **Morphology-mediated effects:** Apart from these mechanisms, our group showed a novel study reporting on the effects of morphological modifications on ferromagnetic response of a multiferroic heterostructure.[29,68] They reported corrugated morphology behavior (appearing of several cracks in a disordered patterns) upon electrical biasing of the sample, which vanishes after polarizing the sample in other direction. These surface cracks are reversible and reproducible, after sweeping the voltage several times, the cracks opened deterministically always in the same place and closes without any sign of fatigue by smoothening the surface. The cracks affected the anisotropy of the ferromagnetic layer deposited on top by changing the remanent magnetization and non-volatile rotation of magnetic domains. Despite a huge amount of work already devoted to other magnetoelectric mechanisms in multiferroics, the effect of morphology has never been considered in details. Therefore, in upcoming years these electrically-induced morphology-mediated effects could be an excellent tool to tune the magnetoelectric coupling in multiferroics.

In case of PMN-PT/Ni and PMN-PT/Fe samples that we have used in this thesis, the mechanism that could explain the observed magnetoelectric coupling is related to strain-mediated and electromechanical effects. In fact, the thickness of the iron and nickel layers greatly exceeds the length of the charge shielding length, so the charge-mediated coupling is not responsible for the giant magnetic changes that we have observed. On the other hand, pure iron and nickel are not antiferromagnetic, so exchange bias should be ruled out. However, the modifications of X-ray absorption (XAS) spectra in some specific case of PMN-PT/Fe samples have shown chemical modifications of iron under illumination of a visible light pointing towards the chemistry-mediated ion-migration effects across the interface. All this will be discussed in the following chapters.

1.4. Bibliography

[1] Dragan Damjanovic, *Reports Prog. Phys.* **1998**, *61*, 1267.

[2] J. F. Scott, *Science (80-.).* **2007**, *315*, 954.

[3] G. A. Samara, in (Eds.: H. Ehrenreich, F.B.T.-S.S.P. Spaepen), Academic Press, **2001**, pp. 239–458.

[4] W. P. Mason, *J. Acoust. Soc. Am.* **1981**, *70*, 1561.

[5] S. KATZIR, *Arch. Hist. Exact Sci.* **2003**, *57*, 61.

[6] S. Bhagavantam, P. V Pantulu, *Proc. Indian Acad. Sci. - Sect. A* **1967**, *66*, 33.

[7] J. Valasek, *Phys. Rev.* **1921**, *17*, 475.

[8] W. Wang, J. Li, H. Liu, S. Ge, *Adv. Sci.* **2021**, *8*, 2003074.

[9] M. E. Lines, A. M. Glass, *Principles and Applications of Ferroelectrics and Related*

Materials, Oxford University Press, **2001**.

[10] D. Damjanovic, *J. Am. Ceram. Soc.* **2005**, *88*, 2663.

[11] S. Singh, J. P. Remeika, J. R. Potopowicz, *Appl. Phys. Lett.* **2003**, *20*, 135.

[12] P. V Lenzo, E. G. Spencer, A. A. Ballman, *Appl. Phys. Lett.* **2004**, *11*, 23.

[13] R. W. Boyd, *Nonlinear Optics*, Academic Press, **2020**.

[14] W. P. Dempsey, S. E. Fraser, P. Pantazis, *BioEssays* **2012**, *34*, 351.

[15] H. Huang, *Nat. Photonics* **2010**, *4*, 134.

[16] I. Grinberg, D. V. West, M. Torres, G. Gou, D. M. Stein, L. Wu, G. Chen, E. M. Gallo, A. R. Akbashev, P. K. Davies, J. E. Spanier, A. M. Rappe, *Nature* **2013**, *503*, 509.

[17] C. Paillard, X. Bai, I. C. Infante, M. Guennou, G. Geneste, M. Alexe, J. Kreisel, B. Dkhil, *Adv. Mater.* **2016**, *28*, 5153.

[18] C. Paillard, B. Xu, B. Dkhil, G. Geneste, L. Bellaiche, *Phys. Rev. Lett.* **2016**, *116*, 247401.

[19] W. H. Liew, Y. Chen, M. Alexe, K. Yao, *Small* **2022**, *18*, 2106275.

[20] Z. L. Wang, Z. C. Kang, *Functional and Smart Materials*, Springer New York, NY, **1998**.

[21] Vladimir M. Fridkin, *Photoferroelectrics*, Springer Berlin, Heidelberg, **1979**.

[22] I. Tatsuzaki, K. Itoh, S. Ueda, Y. Shindo, *Phys. Rev. Lett.* **1966**, *17*, 198.

[23] R. E. Pasynkov, *Ferroelectrics* **1973**, *6*, 19.

[24] P. Poosanaas, K. Uchino, *Mater. Chem. Phys.* **1999**, *61*, 36.

[25] F. Li, S. Zhang, D. Damjanovic, L.-Q. Chen, T. R. Shrout, *Adv. Funct. Mater.* **2018**, *28*, 1870262.

[26] O. Noblanc, P. Gaucher, G. Calvarin, *J. Appl. Phys.* **1996**, *79*, 4291.

[27] Y. Zhang, D. Xue, H. Wu, X. Ding, T. Lookman, X. Ren, *Acta Mater.* **2014**, *71*, 176.

[28] B. Noheda, D. E. Cox, G. Shirane, J. Gao, Z.-G. Ye, *Phys. Rev. B* **2002**, *66*, 54104.

[29] F. Motti, G. Vinai, V. Bonanni, V. Polewczyk, P. Mantegazza, T. Forrest, F. Maccherozzi, S. Benedetti, C. Rinaldi, M. Cantoni, D. Cassese, S. Prato, S. S. Dhesi, G. Rossi, G. Panaccione, P. Torelli, *Phys. Rev. Mater.* **2020**, *4*, 114418.

[30] J. Heidler, M. Fechner, R. V Chopdekar, C. Piamonteze, J. Dreiser, C. A. Jenkins, E. Arenholz, S. Rusponi, H. Brune, N. A. Spaldin, F. Nolting, *Phys. Rev. B* **2016**, *94*, 14401.

[31] S. Zhang, Y. G. Zhao, P. S. Li, J. J. Yang, S. Rizwan, J. X. Zhang, J. Seidel, T. L. Qu, Y. J. Yang, Z. L. Luo, Q. He, T. Zou, Q. P. Chen, J. W. Wang, L. F. Yang, Y. Sun, Y. Z. Wu, X. Xiao, X. F. Jin, J. Huang, C. Gao, X. F. Han, R. Ramesh, *Phys. Rev. Lett.* **2012**,

108, 137203.

[32] K. Uchino, M. Aizawa, *Jpn. J. Appl. Phys.* **1985**, *24*, 139.

[33] K. Uchino, M. Aizawa, L. S. Nomura, *Ferroelectrics* **1985**, *64*, 199.

[34] B. Kundys, M. Viret, D. Colson, D. O. Kundys, *Nat. Mater.* **2010**, *9*, 803.

[35] W. Jin Hu, Z. Wang, W. Yu, T. Wu, *Nat. Commun.* **2016**, *7*, 10808.

[36] A. S. Makhort, F. Chevrier, D. Kundys, B. Doudin, B. Kundys, *Phys. Rev. Mater.* **2018**, *2*, 3.

[37] S. Chikazumi, *Physics of Ferromagnetism*, Oxford University Press, **1997**.

[38] B. D. Cullity, C. D. Graham, *Introduction to Magnetic Materials*, John Wiley \& Sons, **2011**.

[39] A. Goldman, *Handbook of Modern Ferromagnetic Materials*, Springer Science \& Business Media, **2012**.

[40] D. Wei, *Micromagnetics and Recording Materials*, Springer Science \& Business Media, **2012**.

[41] S. Blundell, *Magnetism in Condensed Matter*, OUP Oxford, **2001**.

[42] E W Lee, *Reports Prog. Phys.* **1955**, *18*, 184.

[43] E. Du Trémolet de Lacheisserie, *Magnetostriction : Theory and Applications of Magnetoelasticity*, CRC Press, Boca Raton SE -, **1993**.

[44] J. Salach, R. Szewczyk, A. Bieńkowski, *J. Electr. Eng.* **2013**, *61*.

[45] E. Villari, *Ann. Phys.* **1865**, *202*, 87.

[46] R. Becker, *Zeitschrift für Phys.* **1930**, *62*, 253.

[47] M. Trassin, *J. Phys. Condens. Matter* **2015**, *28*, 33001.

[48] M. Fiebig, T. Lottermoser, D. Meier, M. Trassin, *Nat. Rev. Mater.* **2016**, *1*, 16046.

[49] W. Eerenstein, N. D. Mathur, J. F. Scott, *Nature* **2006**, *442*, 759.

[50] C. A. Fernandes Vaz, U. Staub, *J. Mater. Chem. C* **2013**, *1*, 6731.

[51] M. Fiebig, *J. Phys. D. Appl. Phys.* **2005**, *38*, R123.

[52] S. Dong, J.-M. Liu, S.-W. Cheong, Z. Ren, *Adv. Phys.* **2015**, *64*, 519.

[53] N. A. Hill, *J. Phys. Chem. B* **2000**, *104*, 6694.

[54] C.-Y. Kuo, Z. Hu, J. C. Yang, S.-C. Liao, Y. L. Huang, R. K. Vasudevan, M. B. Okatan, S. Jesse, S. V Kalinin, L. Li, H. J. Liu, C.-H. Lai, T. W. Pi, S. Agrestini, K. Chen, P. Ohresser, A. Tanaka, L. H. Tjeng, Y. H. Chu, *Nat. Commun.* **2016**, *7*, 12712.

[55] G. Catalan, J. F. Scott, *Adv. Mater.* **2009**, *21*, 2463.

[56] D. Sando, A. Barthélémy, M. Bibes, *J. Phys. Condens. Matter* **2014**, *26*, 473201.

[57] J.-G. Park, M. D. Le, J. Jeong, S. Lee, *J. Phys. Condens. Matter* **2014**, *26*, 433202.

[58] I. Dzyaloshinsky, *J. Phys. Chem. Solids* **1958**, *4*, 241.

[59] T. Moriya, *Phys. Rev.* **1960**, *120*, 91.

[60] I. A. Sergienko, E. Dagotto, *Phys. Rev. B* **2006**, *73*, 94434.

[61] H. Feng, *J. Magn. Magn. Mater.* **2010**, *322*, 1765.

[62] J. P. Velev, S. S. Jaswal, E. Y. Tsymbal, *Philos. Trans. R. Soc. A Math. Phys. Eng. Sci.* **2011**, *369*, 3069.

[63] C. Song, B. Cui, F. Li, X. Zhou, F. Pan, *Prog. Mater. Sci.* **2017**, *87*, 33.

[64] F. Matsukura, Y. Tokura, H. Ohno, *Nat. Nanotechnol.* **2015**, *10*, 209.

[65] C. Bi, Y. Liu, T. Newhouse-Illige, M. Xu, M. Rosales, J. W. Freeland, O. Mryasov, S. Zhang, S. G. E. te Velthuis, W. G. Wang, *Phys. Rev. Lett.* **2014**, *113*, 267202.

[66] X. Zhou, Y. Yan, M. Jiang, B. Cui, F. Pan, C. Song, *J. Phys. Chem. C* **2016**, *120*, 1633.

[67] J.-M. Hu, T. Nan, N. X. Sun, L.-Q. Chen, *MRS Bull.* **2015**, *40*, 728.

[68] G. Vinai, F. Motti, V. Bonanni, A. Y. Petrov, S. Benedetti, C. Rinaldi, M. Stella, D. Cassese, S. Prato, M. Cantoni, G. Rossi, G. Panaccione, P. Torelli, *Adv. Electron. Mater.* **2019**, *5*, 1970033.

Chapter 2

Experimental Station and Techniques

2.1. NFFA-Trieste facility and APE-HE Beamline

Nanoscience Foundries & Fine Analysis (NFFA)-Trieste[1] is a project of the MIUR (Italian ministry of University and Research) which is intended to create a demonstrator for a larger project NFFA-EU which is a Horizon 2020 integration project coordinated by CNR-IOM providing transnational open access to a distributed nanoscience infrastructure (more than 20 partners all over Europe), where many nano-foundries are co-located with Analytical Large-Scale facilities. NFFA-Trieste is an open access infrastructure for conducting nanoscience experiments including growth of samples, characterization and advanced spectroscopy using synchrotron radiation and pulsed laser sources with a single-entry point (www.trieste.nffa.it). Most of the experiments described in this study were performed in the framework of NFFA-Trieste project.

The Advanced Photoelectric Effect (APE) beamline located at the Elettra synchrotron Trieste uses photons emitted by two insertion devices located in section number 9 of the storage ring that are arranged in a zig-zag configuration, resulting in two slightly diverging beams (with a small angle of 2 milliradian in the horizontal plane) ending up in two different branches, that can operate independently.[2] One is named ‘‘Low-energy’’ (LE, operating at photon energies between 10 and 100 eV) and is specialized for spin and angle-resolved photoemission spectroscopy. The second one is called as "High energy" (HE, working in the photon energy range of 150 to 1200 eV) and is specialized for performing soft x-rays spectroscopic measurements, including X-ray Photoelectron spectroscopy (XPS), X-ray Absorption spectroscopy (XAS) and X-ray Magnetic Circular Dichroism (XMCD). Most of the measurements discussed in this thesis were performed at the HE branch of the APE beamline. The graphical representation of the two branches of APE beamline and nearby experimental stations that have been used in this project work are shown in the figure 14.

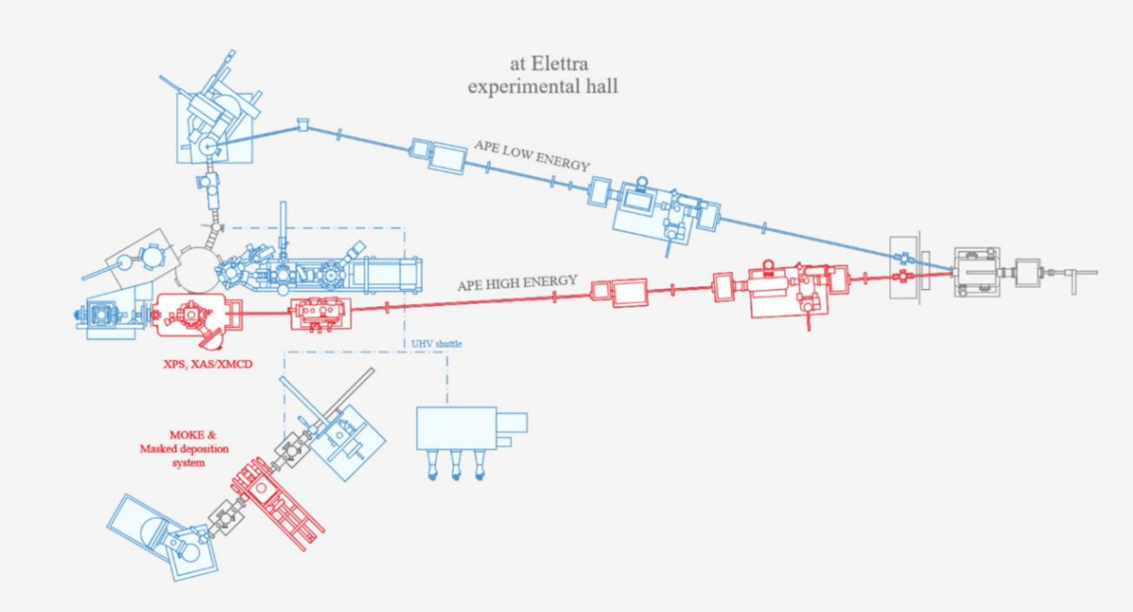

Figure 14: A sketch of the instrumentation available within NFFA-Trieste. The two independently working beamlines (APE-HE and APE-LE) are shown, along with the UHV endstation (XPS, XAS/XMCD) of APE-HE. Sidewise, the Masked deposition chamber and table-top MOKE facility are also shown. The setups described in the text and used for measurements in this thesis project are highlighted in red color.

The undulator connected to the APE-HE branch is an APPLE-II with 36 periods of 2.16 cm each, able to polarize the photon flux in horizontal, vertical or circular polarization by changing the vertical gap and the longitudinal phase between the magnetic arrays (see figure 15). The undulator beam is horizontally deflected onto a planar grating monochromator by a spherical mirror, covering an energy range of 140-1500 eV. The monochromators for both APE-HE and APE-LE are Plane Grating Monochromators (PGM) consisting in two chambers, one for gratings and one for spherical refocusing mirrors. The monochromator spherical mirror focuses the light onto the exit slit in the vertical plane. The horizontal and vertical size of the beam on the sample can be adjusted up to 100 μm using two sets of independently movable slits for horizontal and vertical cutting of the beams, respectively. The resolving power at APE-HE beamline that can be achieved is close to $E/\Delta E > 8000$ at 400 eV, $E/\Delta E > 3000$ above 900 eV, with the photon flux exceeding 5×10^{10} photons/sec at the best resolution in the range of 200–450 eV, that decreases down to 10^{10} photons/sec at 1200 eV.

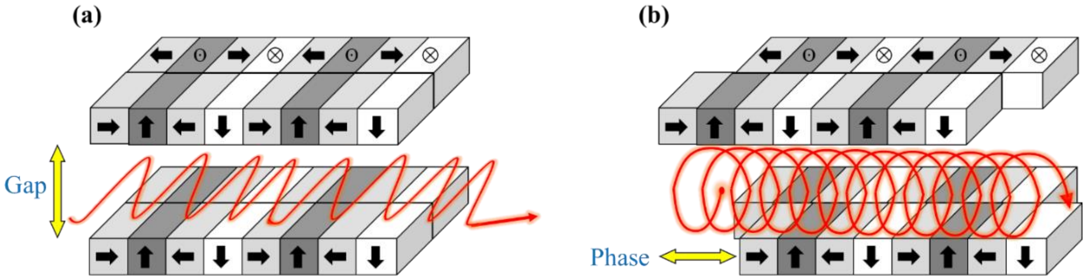

Figure 15: A schematic presentation of APPLE-II undulator of APE-HE beamline. By adjusting the parameters (horizontal and vertical distances i.e., gap and phase, respectively), we can tune the photon energy range of the harmonics and the beam polarization. The small black arrows indicate the direction of the magnetic dipole, while red lines indicate the electron trajectories: **(a)** for horizontal polarization and **(b)** circular polarization.

The APE-HE endstation consists of an Ultra-High Vacuum (UHV) chamber and a second chamber for intermediate vacuum dedicated to host reaction cell for spectroscopic measurements in ambient pressure conditions. The measurements that will be discussed in this thesis were all taken in the UHV chamber, where the sample is placed on a manipulator with four degrees of freedom (x, y, z translations and rotation around a vertical axis), shown in figure 16a. The manipulator is equipped with 3 stages: the cryogenic low-temperature stage (LT), which can be cooled down to 50 K during the measurements, the rotating one (RT), which can rotate the sample surface around an axis parallel to the photon beam, and the high temperature stage (HT), which can be heated up to 500 K during the measurement.

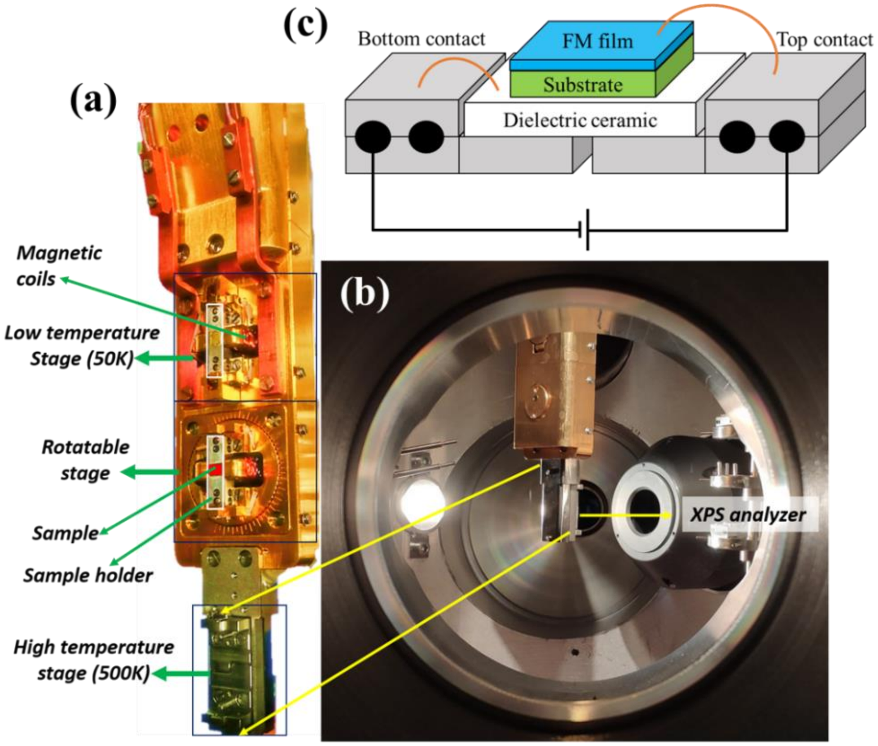

Figure 16: (a) Photograph of the manipulator of APE-HE endstation with various components and stages for placing and characterizing the sample; **(b)** inside view of the UHV chamber, the x-ray beam enters in the chamber from a flange opposite to the view-port from which the photo was taken along with the analyzer for XPS measurements; **(c)** schematic of the specifically designed sample holder for *in-situ* electrical poling, used for out-of-plane polarization of ferroelectric substrates. The top and bottom electrical contacts are usually made with a small drop of silver paint to stick gold wires (shown in orange).

All absorption measurements shown in this study were made in total electron yield (TEY) mode, using a Keithley 6514 picoammeter to measure the drain current from the sample going through ground, although measurements in total fluorescent yield (TFY) can also be made using a photon detector. The same TEY measures are taken simultaneously from a fine gold-plated grid (mesh) placed in front of the endstation to normalize the photon flux during the absorption spectra. A small electromagnet mounted on the manipulator is used to apply in-plane magnetic field pulses parallel to the sample surface in the LT and RT stages, generating magnetic fields up to 800 Oe. This is used to perform x-ray magnetic circular dichroism (XMCD) measurements: the spectra are recorded at remanence after applying alternating field pulses (positive and negative) at each energy point of the measured spectrum to switch the magnetization of the sample at each photon energy value.

Concerning the in situ electrical poling (figure 16c), each manipulator stage has two electrically independent pins used for TEY measurements. The specific sample holder maintains the two contacts insulated with the sample in measurement position thanks to the dielectric ceramic, allowing the application of voltage through the sample. Voltage and current sweeping-cycles are performed and simultaneously recorded using a Keithley 6487 picoammeter/voltage source. The UHV chamber at the end station is therefore fully equipped for *in-operando* characterization, where spectroscopic measurements are performed with a combination of applied electric and magnetic fields. For the experiments described in the following chapters, we attached the bottom unpolished side of the ferroelectric substrate to the sample holder with silver paint, working as an electrical connection with the first lead of the sample holder. For some specific samples, we have prepared a back electrode of Au deposited using magnetron sputtering and then we stick it with silver paint on the sample holder. On the other side, the top surface of all the samples was connected with a gold wire to the second part of the sample holder, attached with a small drop of silver paint. The top magnetic film (metallic) is acting as top electrode while the ferroelectric crystal acts as the insulator between the top and bottom contacts, in this way is possible to apply a voltage across the thickness of the sample. Current v/s Voltage/Electric field characteristics of the sample have been measured directly before and after spectroscopic measurements *in-situ*. For the spectroscopic measurements using TEY detection, we disconnect the voltage source and measure the drain current through the pin connected to the surface of the sample. For carrying out the XPS measurements, we used a Scienta Omicron R3000 electron analyzer which is mounted in the UHV chamber (see figure 16b). The samples have been measured in the normal emission configuration. The XPS detector consists of a 2D delay line with a spatial resolution of 30 x 30 μm^2. The achievable energy resolution at a throughput energy of 50 eV is 50 meV.

2.2. Molecular Beam Epitaxy (MBE) Cluster

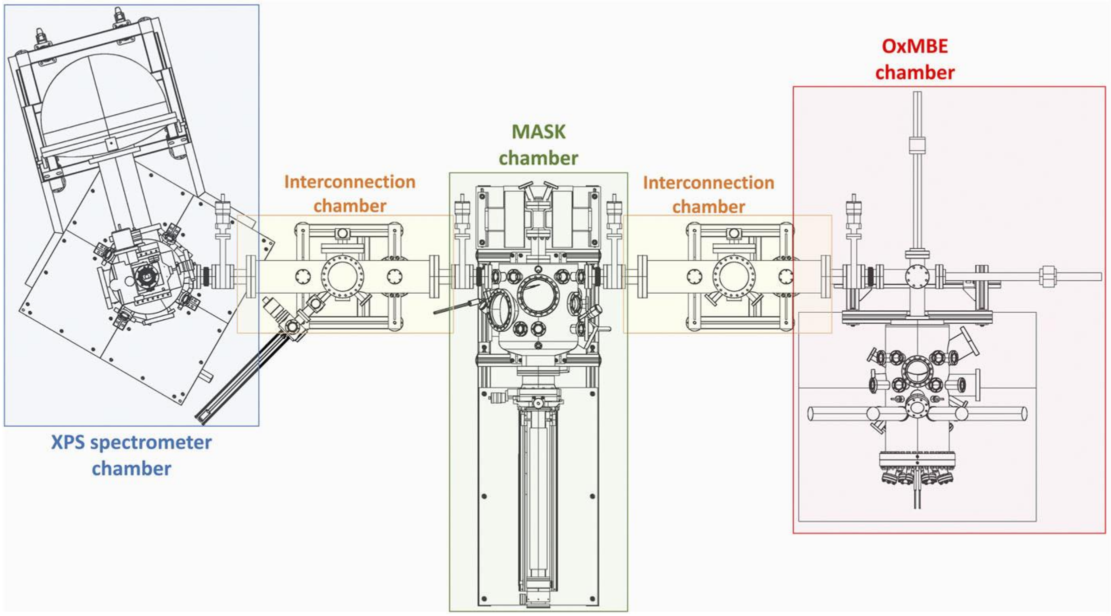

Figure 17: Top view representation of the MBE-Cluster: Oxide MBE chamber (highlighted in red), MASK chamber (green), XPS spectrometer chamber (blue), and the two home-built interconnection chambers (orange).

Most of the samples that will be discussed in this thesis were grown in a deposition chamber that belongs to a cluster of UHV chambers (base pressure of $\sim 10^{-10}$ mbar), where samples can be exchanged for growth and analysis. It is also located in the Elettra Experimental Hall near the APE beamlines, but not directly connected to them.[3] The cluster consists of three different chambers: one MBE chamber for growth of oxides (Ox-MBE), the second one is a deposition chamber used for metals, designed with the possibility of doing MOKE characterization in UHV conditions, and finally the third chamber for performing XPS analysis, see figure 17. Samples can be transferred between the three chambers maintaining the UHV conditions through compact transfer chambers. This allows for step by step sample characterizations of clean surfaces.

In the MASK deposition chamber, the manipulator hosts three stages: in the first one the sample can be heated up to 900 K by electron bombardment and used for high temperature annealing and MBE deposition. Stable rates of sublimation or evaporation can be obtained and the molecular flux can be controlled by physical shutters on the way to the sample substrate. The suitable rate of evaporation, and hence deposition, is typically of the order of few Å/min. This allows a layer by layer growth of the thin film with a fine control of the thickness of the film. A retractable

Quartz Crystal Microbalance (QCM) is used to calibrate the evaporation rate before and after each deposition, in order to evaluate the thickness of the deposited film. The second stage is equipped with a shadow mask system that enables direct deposition of micrometer-sized patterned films. It can be used to attach electrodes or markers *in-situ* to the surface of grown samples. The chamber is also equipped with a sputtering system for surface cleaning and a Low Energy Electron Diffraction (LEED) - Auger apparatus that allows for surface electronic characterization. Finally, a third stage for performing longitudinal MOKE characterization is present in the chamber. The sample can be moved within a narrow section (glass nozzle) of the vacuum chamber that fits in the gap of an electromagnet capable of generating a magnetic field up to 8 kOe parallel to the sample surface. A cooling transfer line mounted to the manipulator can cool the samples down to 5 K in case of liquid He cooling, Samples can be rotated by 360° in azimuth, allowing full in-plane anisotropy characterization.

The theory and experimental setup of MOKE technique is discussed in the next section.

2.3. Experimental Techniques

2.3.1. Magneto-Optical Kerr Effect (MOKE)

The Magneto-Optical Kerr Effect exploits the changes in polarization of an incident light as it is reflected by a magnetic material. If the incident light is linearly polarized, the reflected light will be elliptically polarized, with the long axis rotated from the incident polarization (see figure 18). This effect is equivalent to the Faraday effect, with the latter case measured in transmission rather than reflection.

The Kerr effect can be quantified by two parameters: Kerr rotation (the alteration of the direction of polarization of linearly polarized light) and Ellipticity (a measure of the extent to which circularly polarized light becomes elliptical); generally, having very small values (less than 1°).

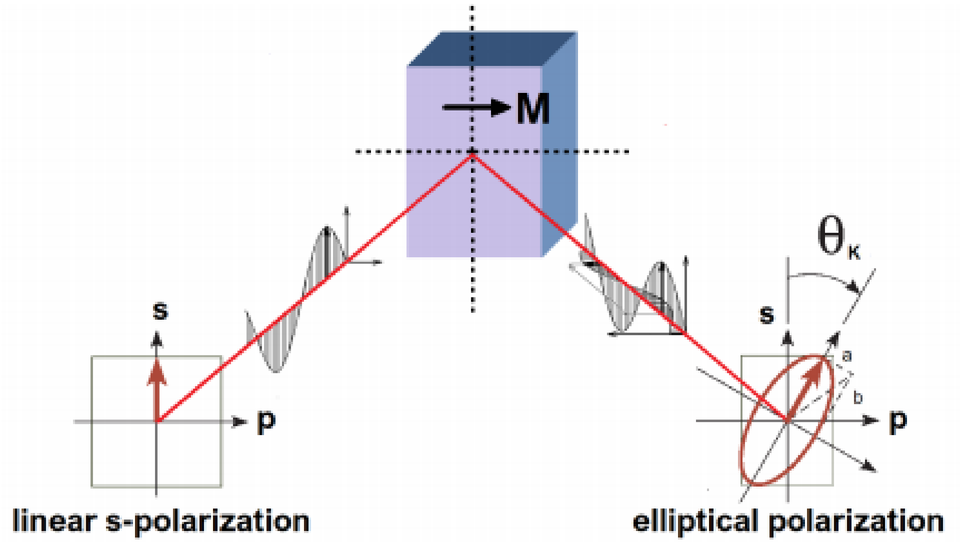

Figure 18: A schematic representation of MOKE; a linearly polarized light impinges a magnetized sample and is reflected back, rotating the principal axis of θ_K and becoming elliptical polarized, with ellipticity $\varepsilon_K = arctg\frac{a}{b}$.

The magneto-optical Kerr effect is attributed to the inter-band transitions excited by visible light; when a macroscopic magnetic order is present (that is, when the system has a net magnetization, which can be reversed in presence of an applied magnetic field), the magnetic material reflects the joint density of states (JDOS). When an electromagnetic wave interacts with matter, the electric field of light causes the movement of electrons within the matter. A linearly polarized radiation can be described as the superposition of two circularly polarized beams of opposite helicity (left-handed and right-handed). Therefore, the oscillation of a bound electron that has absorbed a photon can be described in terms of its polarization. For a non-magnetic material, in the absence of an external magnetic field, the radii of both trajectories of an excited electron moving in a left or right circular motion are equal. On the other hand, when a magnetic field is applied along the direction of wave propagation, an additional Lorentz force acts differently on electrons with either left or right circular motion, resulting in a difference in the radii of the two trajectories. This implies a difference in permittivity and refractive index probed by the two opposite polarizations, which leads to a difference in propagation velocities. In addition to this, magnetic materials give an auxiliary signal much more intense than this, and hence can be detected by MOKE. As a result, the outgoing (reflected) radiation has a new polarization state that changes due to its interaction with the material, and one can measure the ellipticity (ε_K) and rotation of the principal axis are measured by a small angle called the Kerr angle (θ_K). The Kerr ellipticity is caused by the difference in absorption rates of the medium for the two circularly polarized modes. Formally, these effects are represented by the off-diagonal elements of the dielectric tensor and are roughly proportional to the magnetization. After determining the experimental geometry and scattering plane, the polarization can be either parallel (p-polarization) or perpendicular (s-polarization) to its propagation and by measuring the changes in these components between incident and reflected light, we can obtain information about the Kerr parameters and even about the magnetization of the sample.

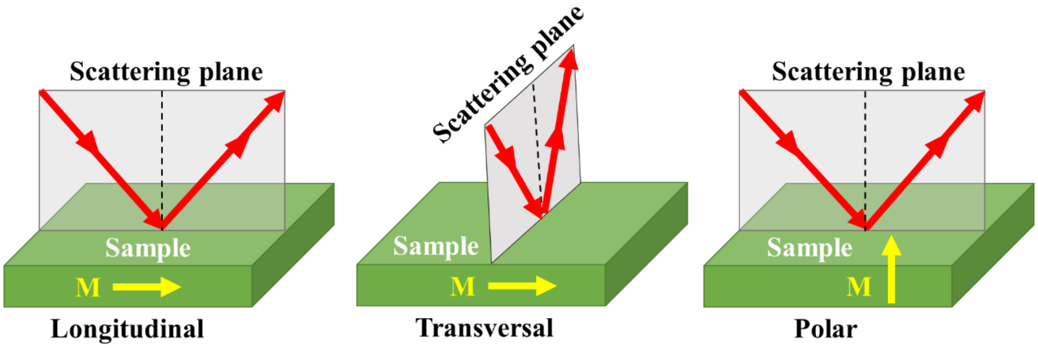

Figure 19: Three possible MOKE geometric configurations with different orientation between the sample magnetization **M** with respect to the incident light.

Three possible geometrical configurations of MOKE can be distinguished (see figure 19), depending on the relative direction between the direction of the applied magnetic field with respect to the sample surface and the incident light: Longitudinal (field parallel to the sample surface and to the incidence plane), Transverse (field parallel to the surface but perpendicular to the incidence plane) and Polar (field perpendicular to the surface of the sample). Each of them responds to different components of the magnetization vector and hence give information about in-plane or out-of-plane magnetization.

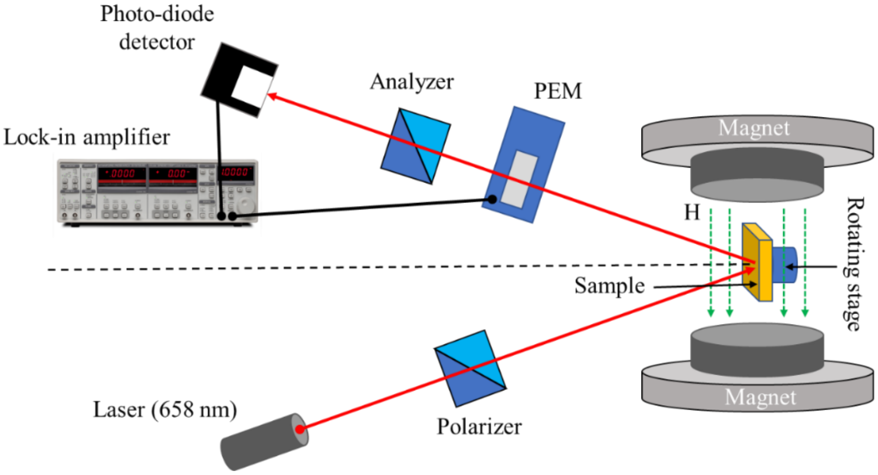

Figure 20: Longitudinal table-top MOKE setup. The red (658 nm) laser beam, passing through a polarizer maximizing the linear component, impinges on the sample surface. The reflected beam passes through a PEM and a second polarizer (analyzer), reaching the photo-diode detector. The reference frequency signal of the PEM and the output signal of the detector are sent to a lock-in amplifier, where the output signal is recorded via software.

The setup used during this thesis is based on longitudinal MOKE configuration, allowing in-plane hysteresis loops to be recorded for different rotations of the sample within the surface plane (see figure 20). A red laser (with wavelength of 658 nm) is used as the light source, becoming s-polarized after passing through a Glan-Thompson crystal acting as polarizer. The light beam impinges the sample with a plane of incidence normal to the sample surface and is reflected along the symmetrical direction. The sample is placed between the poles of an electromagnet with coils capable of generating a variable magnetic field of up to 8 kOe parallel to the plane of incidence. The sample can be rotated about the surface normal (azimuthal angle), allowing the measurement of the in-plane magnetic anisotropy. Before reaching the analyzer, the light beam passes through a photo-elastic modulator (PEM) that oscillates at a precisely tuned frequency (50 kHz) and uses a lock-in amplifier to modulate the phase of the beam. PEMs are being used only in few labs as it is expensive but has wide applications in high-sensitivity optical sensing and ellipsometry techniques,[4,5] thanks to their advantages including wide acceptance angle, low power consumption, and high measurement speed.[6,7] The analyzer is the a second Glan-Thompson crystal oriented close to the p-direction, in order to have only the signal close to the extinction measured on the detector. The light intensity is finally converted into an electrical signal by a photodiode. A lock-in amplifier takes the PEM frequency as an input signal, collects only the signal at that frequency from the detector and rejects noise at all other frequencies. The Kerr ellipticity signal is recorded as a function of the applied magnetic field and processed by a specific software to record the hysteresis loops.

2.3.2. X-ray Absorption Spectroscopy (XAS)

XAS is measured using Total Electron Yield (TEY) detection method, that counts the all the emitted electrons, by measuring the drain current that compensates this flow of charge. This is a very practical technique because requires only a picoammeter connected to the surface of the sample (shown in figure 21a). When a photon is impinged to the sample, it transfers its energy and momentum to one electron of the sample and promotes it to a higher energy empty state and creates a hole in the initial ground state (figure 21b-1). This core hole is spontaneously filled by the process of fluorescence decay of an electron from the higher state, resulting in auger decay of the core hole and excitation of Auger electron absorbing the photon released while auger decay process (see figure 21b-2).

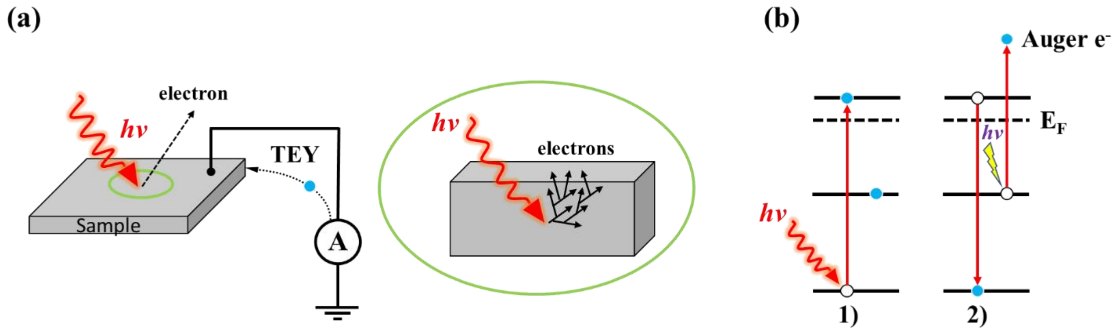

Figure 21: (a) A basic schematic scheme of total electron yield (TEY) method. The primary Auger electrons cause a low energy cascade through inelastic scattering processes on the way to the surface. **(b-1)** A photon is absorbed by the photo-electron and promoted to the higher valence state creating a core-hole, **(b-2)** filled by the process of fluorescence decay of an electron from the higher state, resulting in auger decay of the core hole and excitation of Auger electron.

XAS measures the absorption coefficient *(μ)* of a sample as a function of incident radiant energy ***(I_o)***. It obeys the Beer-Lambert equation for homogeneous isotropic materials, as follows;

$$\boldsymbol{I} = \boldsymbol{I_o} e^{-\mu D} \tag{22}$$

where, *D* is the thickness of the sample and ***I*** is the transmitted beam intensity. The coefficient (μ) for crystalline solids are obtained from the sum of the absorption cross-sections (σ_i) associated with *n* different chemical elements in the unit cell,

$$\mu = \frac{1}{V}\sum_{i=1}^{n}\sigma_i \tag{23}$$

where, *V* is the volume of the unit cell. Experimentally, μ can be determined as the ratio of the beam intensities with and without the sample. In the non-resonant regime, the absorption coefficient decreases with increasing photon energy. However, when the excitation energy is comparable to the binding energy of the core electrons, there is a net increase in absorption, giving rise to an absorption edge. Depending on the energy range, the XAS spectrum is split into two regions: Near-Edge X-ray Absorption Fine Structure (NEXAFS or XANES), which covers the energetic range starting from few eV before the absorption edge to around 50 eV above it, and the Extended X-Ray Absorption Fine Structure (EXAFS), whose upper limit goes from the NEXAFS region to a few hundred eV above the absorption edge. The NEXAFS region is further divided into pre-edge, main-edge, and post-edge regions from which various information about the electronic structure of the sample can be obtained. During the whole thesis, the absorption techniques used has been NEXAFS; in the following, it will be shortened to XAS.

2.3.2.1. Theoretical description of XAS spectroscopy

XAS spectrum of a 3d transition metal atom can be described using a so-called *construction picture*. Figure 22 shows resonant X-ray absorption processes at the L_2 and L_3 edges. In the initial ground state, the *2p* orbitals are fully occupied and no spin-orbit interaction effects are observed. In the excited final state, a *2p* core hole is formed, producing a configuration with an orbital angular momentum $L = 1$, and spin $S = 1/2$. The spin-orbit coupling between them creates two different levels, $J = 3/2$ and $J = 1/2$ (as J is defined as $J = |L - S|$). The resulting electronic transitions corresponding to the $2p_{3/2}$ (L_3) and $2p_{1/2}$ (L_2) states are observed as two peaks in the XAS spectrum and their intensities depend on the transition probabilities.

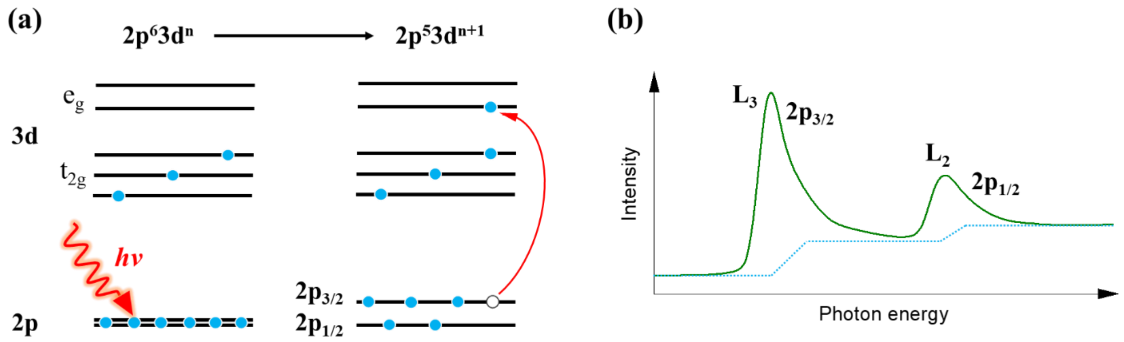

Figure 22: (a) Resonant x-ray absorption process at the *L-edge* in the electron configuration picture. Initially, *2p* orbital are fully occupied and no spin-orbit effect occurs; in case of excitation of an electron, a core-hole is formed and 2p states are spin-orbit split. **(b)** Example of a XAS line shape with two main peaks at the L-edge. The dashed line corresponds to the contribution of the photoelectron excitations into continuum states.

In quantum mechanics, the probability of transition ($W_{i\to f}$) between an initial state $|i\rangle$ and a final one $|f\rangle$ by means of a perturbation is given by the well-known *Fermi golden rule*:[8]

$$W_{i\to f}=\frac{2\pi}{\hbar}|\langle\psi_f|H|\psi_i\rangle|^2\rho(E_f)\delta(E_f-E_i-\hbar\omega) \tag{24}$$

where, E_i and E_f are the energies corresponding to $|\psi_i\rangle$ and $|\psi_f\rangle$, $\rho(E_f)$ is the final-state energy density, the Dirac delta function represents energy conservation, and H is the perturbed Hamiltonian describing electromagnetic radiation. H can be written in the dipole approximation as $H=e_q.\boldsymbol{r}$, where e_q is the photon polarization vector and $\boldsymbol{r}$ is the electron position vector. The photon transfers an angular momentum $q\hbar$ to the electron: $q=0$ refers to the linear polarization of the light, while $q=+1$ and $q=-1$ refer to the right and left circular polarization, respectively. Therefore, the transition probability is related to the propagation direction of the incoming light, with respect to the sample coordinate system, as well as its electric polarization. The initial and final states $|\psi_i\rangle$ and $|\psi_f\rangle$ are identified by the quantum numbers n, s, m_s, l, m_l of the core state and valence state considered. Transitions from $|\psi_i\rangle$ to $|\psi_f\rangle$ are allowed for those matrix elements in Eq. (3) that are different from zero, identified by specific *dipole selection rules*. An interesting information about the absorption process is that, the spectral line shape is contained in the matrix elements. As a powerful consequence of group theory, the Wigner-Eckart theorem[9] states that a matrix element like this can be computed as the product of two elements:

the "radial" part, which determines the line strength, and the "angular" part, which takes into account the symmetry of the two states and is responsible for the selection rules.

Having decided to use the dipole approximation, the main question is how to describe the initial and final state wave-functions. A first intuitive interpretation can be made using independent particle model. The absorption process vacates electrons from the core level (usually where the spin-orbit interaction splits into two lines) and promotes it into an empty higher valence state. Since, we consider the particles independently, we assume that the presence of core holes does not change the empty energy levels, nor the extra electrons in the valence band. The absorption spectrum is simply obtained from the (mathematical) convolution of the core level lines (in principle infinitely narrow) with the empty density of states (DOS), extended by instrumental resolution and core-hole lifetime. More specifically, in practice, we inspect only the empty states with symmetries allowed by the selection rules, which can differ in the two components of the doublet. The independent particle picture provide insight into the physical meaning of XAS spectra, but not much more. In fact, the core hole wavefunction strongly overlaps with the valence states, not only does it perturb them (i.e. the additional potential generated by the holes must be used to calculate DOS), but the actual final state is the typical effect by the combination of the core-hole and valence state wavefunctions, a typical effect of electronic correlations. This is particularly true for the *L* edges of transition metals, like those presented in this thesis. The electronic interactions are described by the Slater-Condon parameters,[10] which are basically direct and exchange integrals between single-particle atomic orbitals, and the energy levels of the system are given by combinations of these parameters. The idea of understanding the absorption spectrum is to calculate the energies of the possible initial and final configuration terms and then of the allowed transitions between the initial ground state and the final state. Regarding the final state, it is important to note that not only the spin-orbit coupling of core holes but also the electrostatic interactions between core holes and valence electrons should be considered. The latter is generally not just a small perturbation and should be treated on the same basis as other perturbations (in a so-called intermediate coupling scheme), so that the eigenstates of the final state are not just the term $^{2S+1}L_J$.

The model presented so far consider individual atoms with defined energy levels. For solids, the situation is complicated by neighboring atoms that change their energy state. For example, in 3D transition metals, the *d* levels form a set of states described by the valence band and thus cannot be labeled with the same quantum number. The strength of the interaction between the neighbors is described by the crystal field parameters,[11] the number of which increases for lower symmetry. In determining the electronic structure, their relative strength compared to the Slater-Condon parameters is crucial. In the atomistic limit, the effect of crystal consists only of small atomic-level splitting, whereas in the opposite case of strong crystal fields, the eigenstates are characterized by irreducible representations of symmetry groups and arise from the mixing of different atomic terms. This behavior is summarized in the well-known Tanabe-Sugano diagram.[12] The presence of ligands around the absorbing atom has another consequence: charge transfer effects.[13] Charge transfer effects are important for reproducing the correct line-shape, especially peak broadening, and can cause the presence of faint satellite peaks in XAS. Besides being an element-specific technique, XAS is also a very useful tool to study the magnetic properties of the transition metals, exploiting the circular polarization of light as well as the definite spin-symmetry of the valence states, which characterizes the ferromagnets.

2.3.3. X-ray Magnetic Circular Dichroism (XMCD)

X-ray magnetic circular dichroism (XMCD) is the difference between two XAS spectra taken with opposite circularly polarized light (with $q = +1$ and $q = -1$). The result is a non-zero curve if the beam impinges on a magnetic material with its macroscopic magnetization axis oriented along the photon beam propagation. In the case of the 2p − 3d transition ($L_{2,3}$ edges of the transition metals) the $2p$ levels are split in two by the spin-orbit interaction ($2p_{3/2}$ and $2p_{1/2}$). X-rays with $q = \pm 1$ will promote transitions in which $\Delta m_l = \pm 1$. On the other hand, the spin moment will be preserved, $\Delta m_s = 0$. Dichroism originates from the fact that the 3d electrons in the magnetic material have a well-defined m_s value (i.e. the valence band is spin-polarized) and the $2p$ electrons do not (they have a defined value of m_j instead). In a simplified 100% spin polarization case, in which only spin-up d electrons are considered, it results as:

$$W^{q}_{2p,j\rightarrow 3d,\uparrow} \propto \sum_{m_j m_l} \left|\langle 2p, j, m_j | \overrightarrow{e_q}.\vec{r} | 3d, m_l, \uparrow \rangle\right|^2 \tag{25}$$

For the fixed q and spin ↑ of the 3d states, the transition probabilities are different for two different j values (corresponding to L_2 and L_3 edges). Switching the value of q (which experimentally means changing the circularity of the x-ray beam) increases the intensity of one edge and decreases the intensity of other, so the difference produces a XMCD spectral shape with one positive and one negative peak (see figure 23) in correspondence to the two edges. It can be proved that a photon with positive helicity (q = +1) excites preferentially spin-up electrons (~ 62.5% in percentage) at the L_3 edge, whereas the same photon excites only ~ 25% spin-up at the L_2 edge. On the contrary a photon with negative helicity (q = −1) excites preferentially spin-up electrons at the L_2 edge (~ 75%), and only ~ 37.5% spin-up at the L_3 edge.[14]

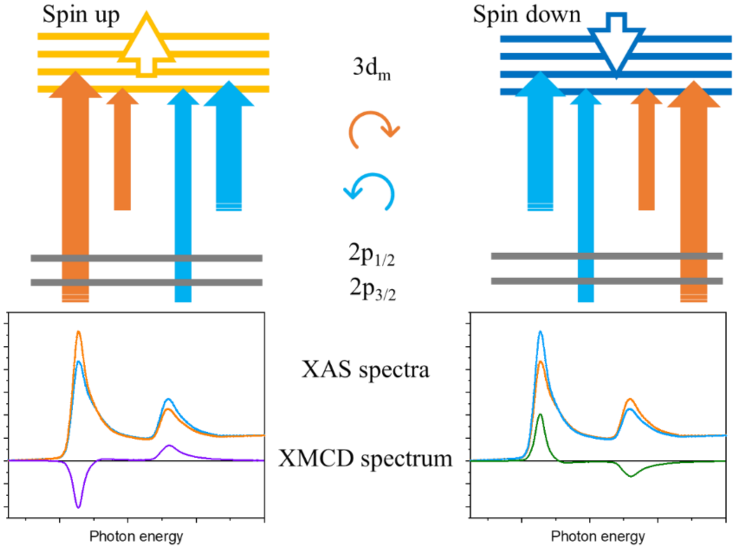

Figure 23: The schematic presentation of XMCD phenomenon in the independent-particle picture (above) and corresponding examples of XMCD spectra (below). The width of the arrows corresponds to the intensity of the transitions. Orange and blue colors correspond to opposite helicity of the photon, light orange and dark blue to opposite orientation of the spin.

The magnitude, peak energy position and shape of the XMCD curves provide information about the magnetic properties of the material. In particular, it is sensitive to the component of the magnetization **M** along the photon propagation direction L_{ph}. It can be written as;

$$\boldsymbol{\Delta I} = I^{+} - I^{-} = I^{\uparrow L_{ph}\uparrow M} - I^{\downarrow L_{ph}\uparrow M} \tag{26}$$

where the arrows correspond to the alignment of L_{ph} and M with respect to each other. The XMCD measurements discussed in this thesis were performed at APE-HE beamline by keeping the photon helicity fixed and reversing the magnetization direction of the sample. From a geometrical point of view, the intensity of a XMCD spectrum is proportional to:

$$\Delta I_{XMCD} \propto P_{circ}\mathbf{m} \cdot L_{ph} = P_{circ}\langle m \rangle cos\theta \tag{27}$$

where, P_{circ} is the degree of circular photon polarization, $\langle m \rangle$ is the expectation value of the magnetic moment of the $3d$ shell and θ is the angle between the directions of the photon angular momentum L_{ph} and $\mathbf{m}$.

Spectroscopic investigations of the magnetic properties of a specific element allow the quantitative determination of several information on the magnetic properties of a certain material, which no other experimental technique can provide in an element sensitive way. Without entering into the details of the physical principles behind the interpretation of the absorption spectra, a specific data treatment widely used to obtain this information, known as *sum rules*,[15–17] is based on these three aspects:

1. The integral of the isotropic XAS spectrum is proportional to the number of holes in the valence states n_h.
2. The integral of the XMCD spectrum is related to the average of the orbital angular momentum L_Z. To obtain a number in physical units, n_h has to be known.
3. If it is possible to clearly subdivide the XMCD spectrum in a L_2 and a L_3 parts, their integrals can be combined to obtain the average of the effective spin angular momentum S_{eff}^{z}. It is "effective" since it contains also a "magnetic dipole term", which is usually small but cannot be always neglected.[18]

These rules make XMCD a very powerful tool for studying magnetism in transition metal and also for calculating the spin and orbital magnetic moment. Another unique feature of this technique is its sensitivity and specificity to elements. In alloys, it can be used to determine the magnetic behavior of different components[19] or to selectively investigate the induced magnetism of interfacial non-magnetic materials.[20] Finally, by measuring the TEY signal at the photon energy at resonance with the maximum of the dichroic signal and varying the applied magnetic field, we can measure the element-sensitive hysteresis loop, which can be particularly informative in presence of interfaces or induced magnetism phenomena.

2.3.4. X-ray Diffraction (XRD)

X-ray diffraction (XRD) is a highly versatile non-destructive analytical technique used to analyze the crystal structure of solids. XRD has traditionally been used for bulk sample analysis, but with the advent of new optical systems, thin film analysis can also be performed using XRD. The technique uses Bragg's law of diffraction ($n\lambda = 2dsin\theta$) and requires high energy hard x-rays, as they have an extremely small wavelength, to discern details on the atomic level (see figure 24). This law relates the wavelength to the diffraction angle and the atomic lattice spacing in a crystal sample (called the d-spacing). By using a fixed wavelength (i.e. monochromatic X-rays), the d-spacing can be determined for a particular angle. Rotating the sample or detector through a range of angles allows measurement of the entire configuration of the material.

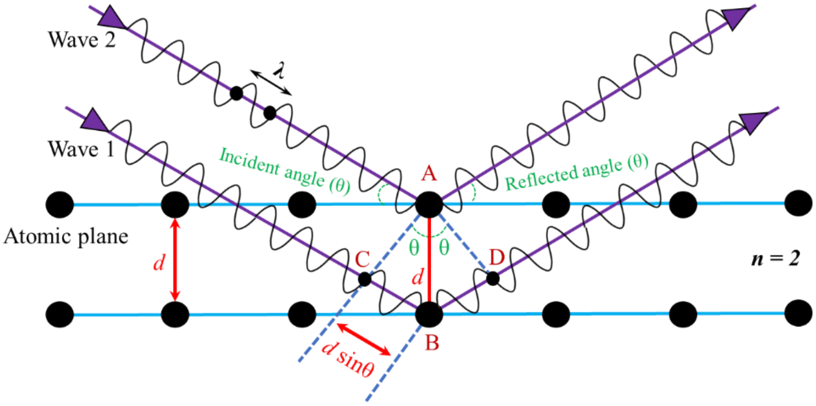

Figure 24: Bragg diffraction; waves 1 and 2, in phase with each other, glance off atoms **A** and **B** of a crystal that has a separation distance ***d*** between its atomic, or lattice, planes. The reflected (glancing) angle θ, as shown by experiment, is equal to the incident angle θ. The condition for the two waves to stay in phase after both are reflected is that the path length CBD be a whole number (***n***) of wavelengths (λ), or ***nλ***. But, from geometry, **CB** and **BD** are equal to each other and to the distance ***d*** times the sine of the reflected angle θ, or d sinθ. Thus, ***nλ = 2d sin θ***, which is the Bragg law. As may be seen from the diagram, when $n = 2$, there is only one wavelength along path **CB**; also, the reflected angle will be smaller than that for, say, $n = 3$. Waves reflected through an angle corresponding to $n = 1$ are said to be in the first order of reflection, the angle corresponding to $n = 2$ is the second order, and so on. For any other angle (corresponding to fractional n), the reflected waves will be out of phase and destructive interference will occur, annihilating them.

At the facility of NFFA-Trieste at MM building of Elettra Sincrotrone, the structural properties of pristine and electrically polarized PMN-PT substrates were determined by means of a four-circle X-ray diffractometer, which is a commercial PANalytical X'Pert diffractometer based on copper cathode technology and designed to allow the analysis of a wide range of materials, from micrometer powders to thin films and/or nano-engineered heterostructures, through the use of appropriate modules that optimize the experimental configuration. In particular, we use a Ge 4-bounce double monochromator that allows the selection of only one wavelength $K\alpha_1$ ($\lambda = 1.54056$ Å) of the copper source, in order to enable the structural analysis of hetero-epitaxial structures with very high resolution. Another configuration permits the analysis of materials with a low power diffraction mode using a simple collimator that greatly increases the number of incident photons, at the expenses of the energy resolution of the source. At these two limit configurations, an intermediate configuration can be also added by the use of a hybrid module composed of single monochromator and converging mirror which allows a reasonable energy resolution of the source (i.e. a single wavelength Kα_1) and a considerable increase of the incident photons compared with the configuration with the Ge-monochromator (i.e. a factor 50-60 in number of photons). The positioning of the samples can be achieved and remotely controlled in all the three dimensions (x, y, and z) and also at different azimuthal angles (Φ, and Ψ, and ω), so as to allow also the two-dimensional structural mapping of samples (see figure 25).

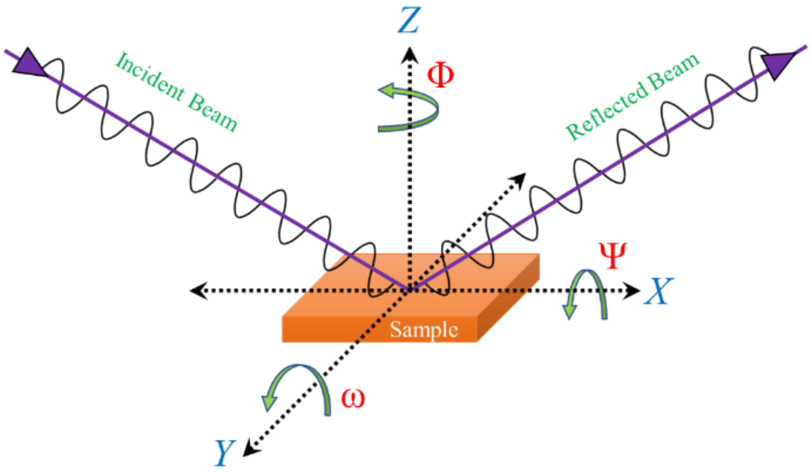

Figure 25: Definition of the sample three dimensional linear movements (X, Y, and Z) and tilting azimuthal angles (Φ, and Ψ, and ω) used for XRD measurements.

The symmetric 2θ-omega and asymmetric 2D-Reciprocal Space Maps (RSM) were measured for bare and FM layer capped different PMN-PT substrates, that helped us in understanding the crystalline structure, strain and orientation of ferroelectric domains in bare and FM layer capped PMN-PT single crystals which greatly influences the properties of a magnetic material deposited on top. These measurements will be discussed in details in the later chapters.

2.3.5. Others

- **Electrical and Photovoltaic-current measurements**

I(E) curves and transport measurements were performed at the APE-HE beamline using a Keithley 6485 picoammeter/voltage source. For the specific study of analyzing the multiferroic properties under light illumination, these measurements were recorded both in absence and presence of 405 nm blue laser illumination. A 405 nm wavelength continuous laser source with variable power (0-800 mW cm^{-2}) from RGB Lasersystems was used to illuminate the whole sample surface. The I(E) curves were measured by recording the current flowing through the thickness of the sample under the application of an out-of-plane voltage of ±300 V (6 kV cm^{-1}). Photocurrent measurements were taken by recording the current under the application of 1 V, modulating the laser intensity during the measurement. The set of measurements was taken in air during MOKE measurements as well as in UHV conditions during in-situ XAS/XMCD characterizations, showing no relevant differences in the electrical response.

- **OPA setup for photocurrent measurements**

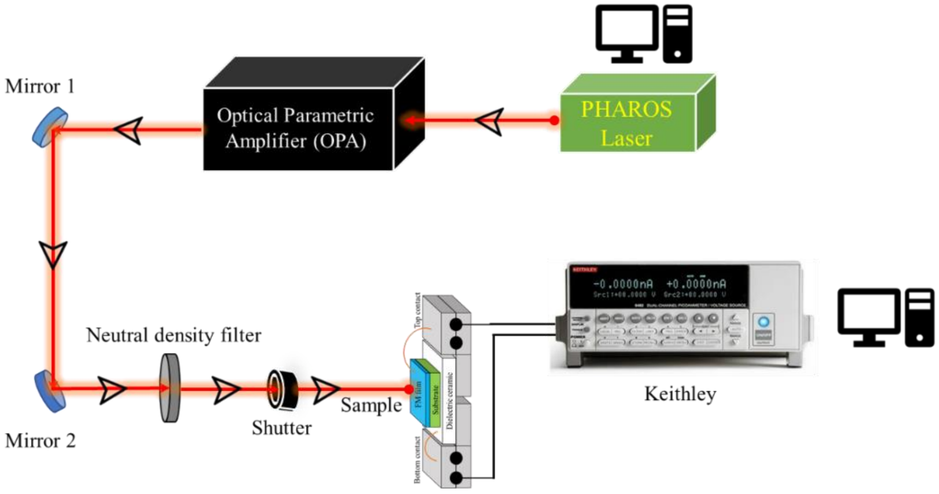

Figure 26: A schematic representation of the photocurrent measurements under variable wavelengths illumination (λ ranging from 360 to 660 nm), produced by OPA.

The setup for photocurrent measurements is shown in figure 26. The measurements were performed under different light wavelength illuminations by using an ORPHEUS collinear Optical Parametric Amplifier (OPA) tool manufactured by Light Conversion company at the Spin Polarized Research Instrument in the Nanoscale and Time (SPRINT) Laboratory situated at the FERMI Experimental Hall. The laser source is a Yb:KGW integrated femtosecond laser system (PHAROS, Light Conversion), producing around 300 fs pulses at 1030 nm, with a repetition rate of 50 kHz, with an average power of 20 W and a maximal energy-per-pulse equal to 400 μJ. The laser seeds an OPA, with a tunable output in the range of 210-2500 nm. A fixed pinhole shutter ensures the same optical spot dimension on the sample, and all the used wavelengths were calibrated to have the same fluence on the sample of 480 mW cm^{-2}. The photocurrent curves will be presented and explained in details in the following chapters.

- **Ferroelectric-strain measurements**

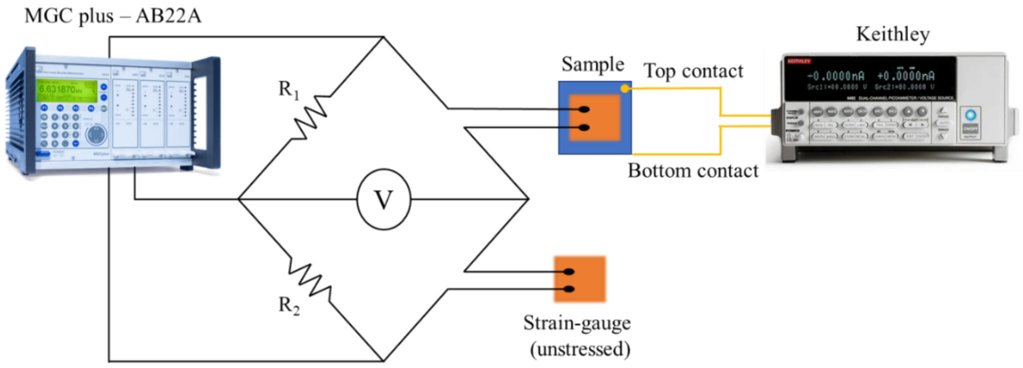

Figure 27: A schematic representation of components and electrical connections based on Wheatstone bridge used for preparing the setup of strain-gauge measurements.

The piezoelectric strain measurements of PMN-PT ferroelectrics were carried out at the Magnetism group of Advanced Materials and Life Science Division of Istituto Nazionale di Ricerca Metrological (INRiM), Torino. The measurements were performed using a simple electronic setup based on the principle of Wheatstone bridge (shown in figure 27), two known electrical resistances (R_1, and R_2) and a reference unstressed strain-gauge were connected along with the sample on top of which we attached another strain-gauge (the strain-gauge was basically a $5 \times 5\ \text{mm}^2$ flexible piece of Kapton tape with an in-built electronic circuit, it changes the dimensions and hence resistance according to the strain/stress induced in the sample). Initially, when there was no strain, the value of sample offset for strain is calibrated according to the background strain of unstressed reference strain-gauge in order to balance the resistances of the two parallel branches of Wheatstone bridge setup by adjusting the known resistances of R_1 and R_2. Once a voltage is applied through the thickness of the sample using the Keithley 6485 picoammeter/voltage source, due to piezo-elasticity of ferroelectrics a strain is induced in PMN-PT which modifies the resistance of the strain-gauge attached to the sample and hence the calibrated corresponding value of strain output was shown by MGC plus – AB22A data acquisition system. The typical strain v/s electric filed ferroelectric butterfly curves were obtained for all the different PMN-PT substrates, showing a maxima and minima of strain at the electric coercive field and saturation of ferroelectric domains, respectively. The curves will be shown in the following chapters.

- **Micro-Raman Analysis**

Raman spectroscopy is a non-destructive analytical technique where inelastically scattered light is used to determine the vibrational mode energy of a sample.[21–24] It is commonly used to provide a compositional fingerprint based upon the interaction of light with the chemical bonds within a material. The technique relies upon measuring the frequency spectrum of the radiation scattered by a sample after illuminating it with a high intensity monochromatic laser light source. The majority of the scattered light is of the same wavelength as the laser source (elastic scattering) and does not provide useful information – this is called *Rayleigh Scattering*.[21,23] However, a small amount of light (typically ~0.000001%) is inelastically scattered at different wavelengths, which depend upon the chemical structure of the analyte – this is called as *Raman Scattering*[21]; Raman-scattered radiation has frequencies lower and higher than the incident radiation, giving Stokes and anti-Stokes bands, respectively. A Raman spectrum features a number of peaks with different intensities and wavelength positions of the scattered light. The inelastic peaks appear at frequencies that differ from the incident one by the so-called Raman shift: this quantity is independent of the excitation frequency and corresponds, for each peak, to the energy of a specific molecular bond vibration or phonon mode in a crystal lattice. Laser light is a plane wave (transverse mode), thus the polarization vector is necessarily orthogonal to the propagation direction and hence, the polarization vectors of the incident and scattered light are in the y-z plane. Another important information is the intensity of each phonon mode, which is usually dependent on the scattering geometry. In particular, its dependence on the relative angle between light polarization and specific sample's crystallographic directions can be compared to theoretical calculations and unveil precious information of the symmetry of phonon modes, thus on the symmetry of the crystal (i.e., crystal structure).[25,26]

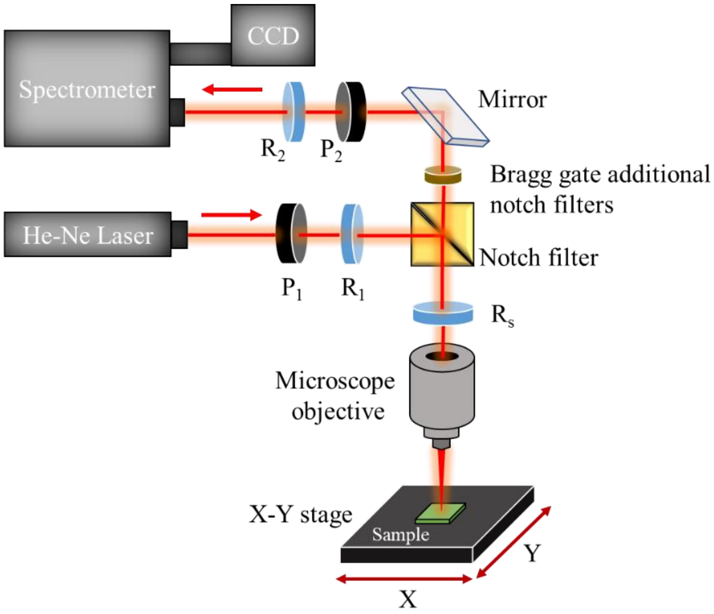

Figure 28: Schematics of a typical micro-Raman setup for polarization-resolved measurements in backscattering mode. The polarizers and half-plate retarders are indicated by Pi and Ri, respectively.

The Raman setup is presented in figure 28. For our experiments, Raman spectra were collected in the backscattering geometry using a Horiba (LabRAM HR-Evolution) Raman microscope equipped with a He-Ne laser of 632.8 nm wavelength yielding the output power of 20 mW. The beam passes through a polarizer (P_1) to purify its polarization and eliminate small depolarizing effects which can arise from the laser itself or from the optical elements in the beam path. After this, we used a lambda half-plate (R_1), which axis is positioned at an angle $\theta/2$ with respect to the axis of P_1 to rotate the incident light polarization. The polarization of the laser beam coming out from R_1 will form an angle θ with the optical axis of P_1. The beam is then guided towards the sample with a polarization conserving notch filter, reflecting the incident light (and transmitting the light at different wavelengths), and focalized with a microscope objective.[27,28] An additional polarization rotator is positioned on the microscope head, being crossed in one direction by the incident light, in the opposite direction by the scattered light: it rotates the incoming polarization of a given angle φ, and rotates the scattered light backwards of the same angle. From a symmetry point of view, this element is equivalent to a rotation of the sample about the microscope axis: using a rotator is more convenient than rotating the sample, as it ensures the measurement is always carried out on the same sample spot. As the diffraction-limited spot size is approximately given by the excitation wavelength divided by the numerical aperture (NA) of the objective, a short wavelength and a high NA (>0.8) objective are ideal to measure nanostructures with sub-micrometric resolution. The sample was placed on a 2D X-Y piezoelectric stage in such a way that it can be scanned automatically in-plane with high precision. In our case, the spot size of beam on the sample was confined to approximately 3 μm by using a 632.8 nm line of a He-Ne laser and a 20x objective with 3 mm focal length. In this configuration we carried out single spectra and 2D map measurements by scanning the sample surface over an area of 130×130 μm^2 with 5 μm step size. In the backscattering geometry detection mode, the inelastically scattered signal is collected by the same objective and passes through the notch filter. The signal is then guided by a set of mirrors to a dispersive spectrometer. Before entering into the spectrometer, a second polarizer (P_2) was used to select the scattered radiation with components of the polarization either parallel or perpendicular to the polarization of the excitation beam, followed by a second lambda half-plate (R_2) to rotate the light polarization backwards, as so to enter the spectrometer with a fixed polarization configuration. The spectrometer (800 mm focal length) was equipped with a 600 grooves/mm diffraction grating, providing a high spectral resolution almost equal to 3±1 cm^{-1}. It is important to remove the contribution from the elastically scattered light from the spectrum as the spontaneous Raman scattering is typically very weak; as a result, the main difficulty is to separate out the weak inelastically scattered light from the intense Rayleigh scattered light (commonly referred as "laser rejection"). In our case, it was removed by a state-of-the-art optical filtering device based on three BragGrate Notch filters, thus allowing to collect the Raman signal down to very low wavenumbers (about 10 cm^{-1}). Finally, a Peltier cooled CCD was used to collect the Raman scattered light signals.

2.4. Bibliography

[1] NFFA trieste, “NFFA Trieste,” can be found under https://www.trieste.nffa.eu/techniques/characterization/xrd/, **n.d.**

[2] G. Panaccione, I. Vobornik, J. Fujii, D. Krizmancic, E. Annese, L. Giovanelli, F. Maccherozzi, F. Salvador, A. De Luisa, D. Benedetti, A. Gruden, P. Bertoch, F. Polack, D. Cocco, G. Sostero, B. Diviacco, M. Hochstrasser, U. Maier, D. Pescia, C. H. Back, T. Greber, J. Osterwalder, M. Galaktionov, M. Sancrotti, G. Rossi, *Rev. Sci. Instrum.* **2009**, *80*, 43105.

[3] G. Vinai, F. Motti, A. Y. Petrov, V. Polewczyk, V. Bonanni, R. Edla, B. Gobaut, J. Fujii, F. Suran, D. Benedetti, F. Salvador, A. Fondacaro, G. Rossi, G. Panaccione, B. A. Davidson, P. Torelli, *Rev. Sci. Instrum.* **2020**, *91*, 85109.

[4] W. Al-Basheer, in *Nonlinear Opt. Appl. XI*, SPIE, **2019**, pp. 150–155.

[5] P. Mukherjee, N. Hagen, Y. Otani, in *Biomed. Imaging Sens. Conf.*, SPIE, **2018**, pp. 101–103.

[6] J. C. Cheng, L. A. Nafie, S. D. Allen, A. I. Braunstein, *Appl. Opt.* **1976**, *15*, 1960.

[7] D. B. Chenault, R. A. Chipman, *Appl. Opt.* **1993**, *32*, 3513.

[8] F. De Groot, A. Kotani, *Core Level Spectroscopy of Solids*, Taylor \& Francis Group, **2008**.

[9] J. Hunt, *Stud. Hist. Philos. Sci. Part A* **2021**, *87*, 28.

[10] J. Verbeek, J. H. Van Lenthe, *Int. J. Quantum Chem.* **1991**, *40*, 201.

[11] R. C. Johnson, *J. Chem. Educ.* **1965**, *42*, 147.

[12] R. A. Howald, *Chem. Educ.* **2001**, *6*, 78.

[13] R. Otero, A. L. Vázquez de Parga, J. M. Gallego, *Surf. Sci. Rep.* **2017**, *72*, 105.

[14] J. Stöhr, H. C. Siegmann, *Magnetism: From Fundamentals to Nanoscale Dynamics*, Springer, **2006**.

[15] W. L. O’Brien, B. P. Tonner, *Phys. Rev. B* **1994**, *50*, 12672.

[16] J. Stöhr, *J. Electron Spectros. Relat. Phenomena* **1995**, *75*, 253.

[17] C. T. Chen, Y. U. Idzerda, H.-J. Lin, N. V Smith, G. Meigs, E. Chaban, G. H. Ho, E. Pellegrin, F. Sette, *Phys. Rev. Lett.* **1995**, *75*, 152.

[18] G. Shibata, M. Kitamura, M. Minohara, K. Yoshimatsu, T. Kadono, K. Ishigami, T. Harano, Y. Takahashi, S. Sakamoto, Y. Nonaka, K. Ikeda, Z. Chi, M. Furuse, S. Fuchino, M. Okano, J. Fujihira, A. Uchida, K. Watanabe, H. Fujihira, S. Fujihira, A. Tanaka, H. Kumigashira, T. Koide, A. Fujimori, *npj Quantum Mater.* **2018**, *3*, 3.

[19] C. Stamm, J.-U. Thiele, T. Kachel, I. Radu, P. Ramm, M. Kosuth, J. Minár, H. Ebert, H. A. Dürr, W. Eberhardt, C. H. Back, *Phys. Rev. B* **2008**, *77*, 184401.

[20] F. Maccherozzi, M. Sperl, G. Panaccione, J. Minár, S. Polesya, H. Ebert, U. Wurstbauer, M. Hochstrasser, G. Rossi, G. Woltersdorf, W. Wegscheider, C. H. Back, *Phys. Rev. Lett.* **2008**, *101*, 267201.

[21] N. Colthup, *Introduction to Infrared and Raman Spectroscopy*, Elsevier, **2012**.

[22] P. L. Stiles, J. A. Dieringer, N. C. Shah, R. P. Van Duyne, *Annu. Rev. Anal. Chem.* **2008**, *1*, 601.

[23] E B Hanlon, R Manoharan, T-W Koo, K E Shafer, J T Motz, M Fitzmaurice, J R Kramer, I Itzkan, R R Dasari, M S Feld, *Phys. Med. Biol.* **2000**, *45*, R1.

[24] R. S. Das, Y. K. Agrawal, *Vib. Spectrosc.* **2011**, *57*, 163.

[25] C. Fasolato, I. Zardo, M. De Luca, in (Eds.: N. Fukata, R. Rurali), Springer Singapore, Singapore, **2021**, pp. 307–348.

[26] V. Piergrossi, C. Fasolato, F. Capitani, G. Monteleone, P. Postorino, P. Gislon, *Int. J. Environ. Sci. Technol.* **2019**, *16*, 1227.

[27] S. Jimenez-Sandoval, *Microelectronics J.* **2000**, *31*, 419.

[28] Z. Xu, Z. He, Y. Song, X. Fu, M. Rommel, X. Luo, A. Hartmaier, J. Zhang, F. Fang, *Micromachines* **2018**, *9*, DOI 10.3390/mi9070361.

Chapter 3

Visible light induced photostriction and triggered magnetostriction in PMN-PT/Ni heterostructure

The data presented in this chapter have been published as a full article in Advanced Materials Interfaces.

DOI of the article: *https://doi.org/10.1002/admi.202201337* *(Adv. Mater. Interfaces* **2022**, *9,* 2201337*).*

The article has been selected for the front cover of the issue: *https://doi.org/10.1002/admi.202270196*

This chapter presents the effects of light illumination on ferroelectric and magnetic properties of PMN-PT/Ni multiferroic heterostructure. The first introductory section of this chapter describes briefly the concepts related to physical properties of the materials that have been used for the study, followed by an overview on the state-of-the-art literature. The scope is also to highlight the novelty and importance of the presented work, which emphasizes on the photostrictive effect induced by laser illumination in the PMN-PT ferroelectric substrate and its effect on the nickel thin film via inverse magnetostriction mechanism. The experimental results of the study are presented in section 3.2 followed by their discussion. Finally, the conclusion and future possible developments are discussed in the section 3.3.

3.1. Introduction

Whenever a FE material is illuminated by light with above-bandgap photon energy, free charge carriers are generated across the material via bulk photovoltaic effect (BPVE), which modifies the internal electric field of the sample[1–4]. The BPVE occurs in solids with broken inversion symmetry and refer to the generation of a direct current due to uniform illumination of light, without the need for a heterostructure or interface that separates the photogenerated charge carriers, a distinctive feature of the traditional photovoltaic effect. The superposition in FE materials of BPVE with inverse piezoelectric effect leads to light-induced non-thermal strain in the material (i.e., expansion or contraction under light), known as the photostrictive effect (see chapter 1 for a more detailed description).[5–8] The photostriction phenomenon was observed in four main groups of materials: ferroelectrics, polar, and non-polar semiconductors, as well as in organic-based materials. Since then, the main attention was renewed towards the ferroelectric and inorganic based materials. The largest values of photostriction are observed in organic materials, but their generally slow response time limits their potential application; on the other hand, photovoltaic ferroelectrics have relatively fast response time but low magnitude of photostrictive effect. The discovery of photostriction in FE was firstly reported by Tatsuzaki *et al.*[9] in 1966 for SbSI crystals, where they showed that the combination of BPVE and inverse piezoelectric effect allows using light to modify strain, with SbSI behaving as a photo-piezoelectric material. Specifically, the SbSI length was modified along the polar *c* axis when illuminated uniformly under visible light ranging from 580 to 740 nm, with a nonlinear dependence, see figure 29. This amonotonous dependence is due to the presence of two competitive contributions in the ferroelectric regime: electric field redistribution, leading to increment of electric field, and the electric field screening by photo-induced charge carriers, leading to a decrease of the electric field in the crystals. In confirmation of this assumption, the photostriction sign changes its sign in the ferroelectric region at ~650 nm, in close correspondence to the maximum value of photoconductivity. The reported photostriction was in the order of 10^{-5}. The sign of modulation of length was found to be opposite to the case of thermal expansion, proving the purely optically driven origin of the strain modification under light. The photoinduced strain was found to be positive below the phase transition point (T_C) i.e., 22° C, where the crystal has both photosensitive and ferroelectric properties, while much smaller variations of strain were detected close to the paraelectric regime (25°C), confirming its relation to the electrically polar state.

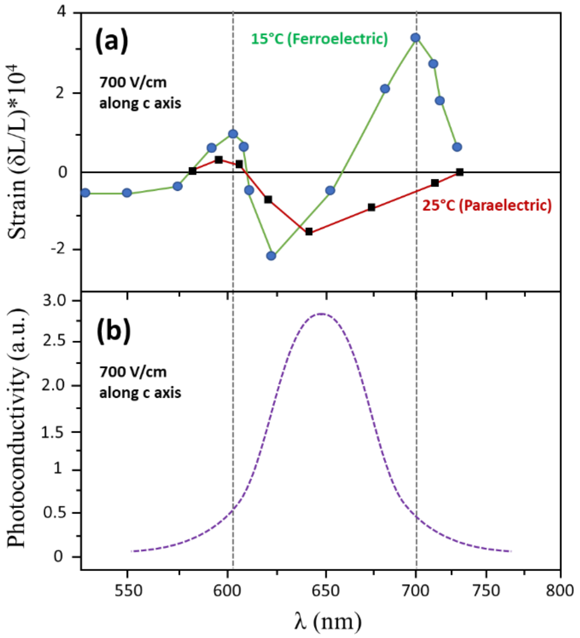

Figure 29: (a) Photostriction in SbSI single crystal upon illumination of different wavelength as the function of temperature: in ferroelectric (15° C) and near para-electric regimes (25° C) and **(b)** photoconductivity as the function of wavelength.[9,10]

Despite its remarkable photovoltaic and photostrictive properties, the SbSI crystals are not appealing for room temperature applications due to low ferroelectric Curie temperature ($T_C = 21.85\ °\mathrm{C}$). Since then, several studies have focused on photostrictive effects in different FE materials and thin films with the aim of maximizing both the photostrictive properties and the Curie temperature. Among them, we can cite $Pb_{(1-x)}La_x(Zr_yTi_{(1-y)})_{(1-x/4)}O_3$ (PLZT),[5,11] $BiFeO_3$ (BFO),[7,12,13] and $BaTiO_3$ (BTO).[14] Multiferroic BFO was the first compound in which fast (below 100 μs) photostriction was reported, attracting the attention of the optical scientific community.[13,15,16] As photostriction depends on the light penetration depth, the response time and magnitude can be further improved in thin films;[17] for instance, the photostrictive response in BFO thin films was reported to be in the picoseconds range.[12]

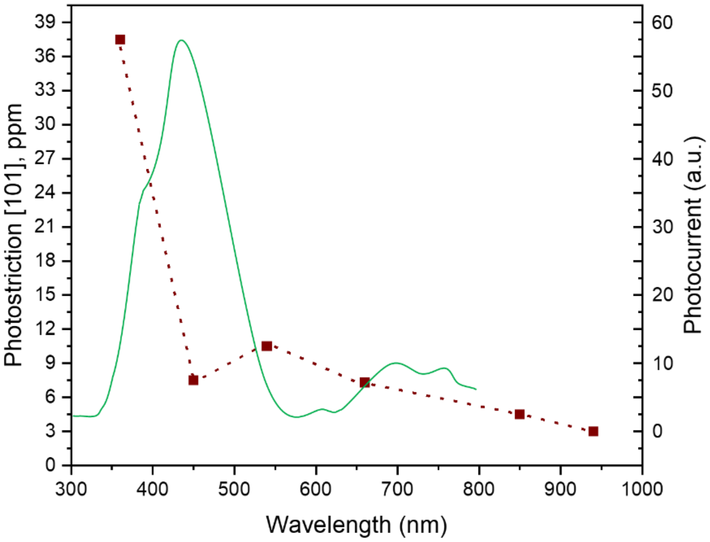

Figure 30: Wavelength dependence of photostriction (brown) and photocurrent (green) in single crystal of $BiFeO_3$.[8]

Also in the case of BFO, the photostrictive effect showed an amonotonous dependence (figure 30)[18] due to the combination of optical rectification[12] and light-induced charge generation[13]. Since BFO is multiferroic with antiferromagnetic order, this can potentially directly couple ferroelectric photostriction to its magnetic properties via elastic interactions. It has been reported that the photostriction of BFO single crystal decreases in presence of a magnetic field.[7]

While $PbTiO_3$ has also been reported to have fast photostrictive effect in tens on picoseconds scale,[19] $Pb(Mg_{1/3}Nb_{2/3})O_3$-$_x PbTiO_3$ (PMN-PT) resulted particularly interesting due to its endurance to polarization switching and relatively low cost.[20–22] PMN-$_x$PT crystals exhibit variations in structural and electromechanical properties as a function of PT concentration. In the case of PMN-$_{0.4}$PT, the structure lies near the morphotropic phase boundary, with a tetragonal structure at room temperature.[23] PT concentration impacts directly the optical properties of PMN-PT crystals,[24–26] with the refractive index increasing with the increase in PT content.[24,27] BPVE directly depends on the refractive index and hence on the band gap energy of FE substrates.[28] Very recently Liew *et al.*[29] used light illumination on a PMN-PT cantilever, showing a detectable deflection due to photostriction. Interestingly, the authors proposed a photostrictive model for which photostriction does not require BPVE and converse piezoelectricity to coexist globally in pristine PMN-PT, but only locally for each FE domain.

Since in FE the photo-ferroelectric properties are inherently a result of the coupling between its optical and mechanical functionalities, this opens an avenue for light-controlled applications in optical and magnetic straintronics if coupled with magnetostrictive elements. Specifically, in multiferroic heterostructures, light-induced FE strain modulation proved to be an effective way for tailoring the FM interfacial properties,[30–36] not being affected by aging and fatigue processes typical of voltage-controlled FE polarization switching.[37] For instance, in 2016 Iurchuk *et al.*[30] reported the optical writing and electrical erasing of the magnetic state for hybrid Au/BFO/Ni structure under 404 nm laser illumination, with the residual photostriction depending on BFO ferroelectric state. The ability of functional materials to recover to the initial state is of paramount importance, as the authors observed that ferroelectric or elastic orderings lead to values of residual states that depend on the history of the sample (spontaneous polarization). The observed photo-polarization causes a strain induced distortion at the interface with Ni, optically modifying its magnetic properties with up to 75% change in coercive field under illumination. Concerning PMN-PT/FM heterostructures, state-of-the-art literature still presents very few experimental publications, with all characterizations of both FE and FM parts based on magnetometric and electric measurements only. Among them, it is worth citing Zuo *et al.*, which showed that UV illumination on PMN-$_{0.3}$PT (011) reversibly switches the magnetization of interfacial Ni from easy to hard axis as a function of the FE polarization state.[31] Additionally, with electric field polarization, they reported that PMN-PT/Ni heterostructure exhibits controllable magnetization switching behaviors under the illumination of a proper light intensity.

Many of these studies concerning multiferroic heterostructures involve 3d transition FM materials (Fe, Co, Ni and their alloys), being the most economic and device-oriented solution. Furthermore, they all present large Curie temperatures and can be deposited using industry-appropriate techniques.

In this spirit, during the thesis several heterostructures were deposited and characterized with different FM materials, namely Fe, Ni and CoFeB, and PMN-$_x$PT substrates with different compositions and crystallographic orientations, to determine which combination of substrates and thin films leads to a maximization of the interfacial coupling and light-induced inverse magnetostriction. Among them, Ni thin films as ferromagnetic layer and PMN-$_{0.4}$PT as ferroelectric substrate proved to be the best combination in presence of light illumination.

The following paragraphs will describe the in-depth characterizations of PMN-$_{0.4}$PT/Ni heterostructures, combining electrical, magnetic, photo-transport and spectroscopic analysis in the three polarization states of the substrate, in presence and absence of visible light illumination.

3.2. Results and discussions

As introduced in the previous paragraph, here we present the electrical, structural, magnetic and spectroscopic investigation on the light-induced photovoltaic/photostrictive properties of a PMN-$_{0.4}$PT (001) substrate and on their induced reversible effects on the magnetic properties of an interfacial Ni thin. This was done by combining several different experimental characterizations, which will be described step by step in the following of the chapter.

3.2.1. Photocurrent measurements of PMN-PT substrate via Optical Parametric Amplifier (OPA)

In order to determine the ideal illumination wavelength to maximize the photoinduced effects on PMN-PT, photocurrent measurements were performed as a function of photon energy by using an Optical Parametric Amplifier (OPA) setup at SPRINT (see paragraph 2.3.5 for technical details). The sample was placed on specifically designed sample holder enabling us to apply a voltage through the thickness of the sample, measuring the output current (figure 16c). The unpolished back side of the pristine PMN-PT substrate was glued to the holder by silver paint that acted as the bottom electrode; an AuRh film of 5 nm deposited on top of it acted as top electrode. The schematic representation of the setup is shown in figure 31.

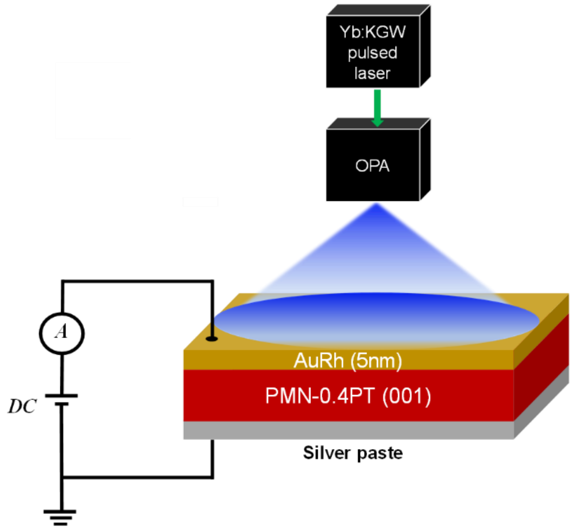

Figure 31: A schematic representation of the photocurrent measurements of PMN-$_{0.4}$PT (001) pristine substrate under variable wavelengths illumination (λ ranging from 360 to 660 nm), produced by OPA using the laser Yb:KGW integrated femtosecond laser source.

The measurements were recorded by applying a steady voltage of 1 V through the thickness of the PMN-$_{0.4}$PT (001) substrate, measuring the output current using a Keithley 6485 picoammeter/voltage source while irradiating the sample with a collimated beam of the same size of the substrate (around 2.5 × 2.5 mm^2) from the front side of the sample. The obtained photocurrent evolution upon 2 minutes illumination as a function of wavelengths (and corresponding photon energies) is shown in figure 32. The fluence was kept constant at 480 mW cm^{-2} for all wavelengths. Figure 32a shows the measured photocurrent after opening the shutter of the OPA setup for a selection of wavelengths.

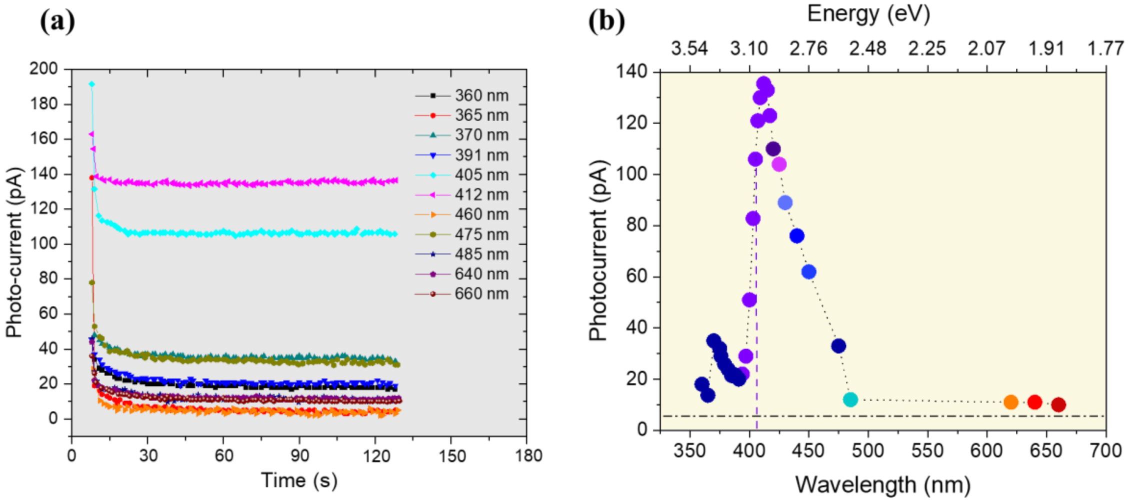

Figure 32: (a) Photocurrent measurements under illumination at different wavelengths and **(b)** stable photocurrent values of PMN-$_{0.4}$PT (001) substrate as a function of wavelength - photon energy. The vertical dotted line in **(b)** corresponds to the photocurrent at 405 nm, i.e. the wavelength used for continuous illumination in all the following characterizations. The horizontal line corresponds to the background photocurrent in the absence of light.

By plotting the stable value of photocurrent for all the measured wavelengths, it is possible to determine the photocurrent - wavelength dependence. The maximum of photocurrent was found in correspondence to a wavelength of 412 nm, corresponding to approximately a photon energy of 3.01 eV, while a detectable photocurrent was observed over a fairly wide energy range of energies, spreading from 2.61 to 3.35 eV, consistently with the range of band gap reported for different crystals of PMN-$_x$PT crystals.[24]

Some important considerations should be done here.

This measurement proves the variation of current passing through the sample under bias in presence of light illumination. It is therefore not a direct photovoltaic measure, neither a BPVE one, which require the measure of a photoinduced electric field in the sample. Nonetheless, a common definition of BPVE is the "generation of a steady photocurrent and above-bandgap photovoltage in a single-phase homogeneous material lacking inversion symmetry",[38] in contrast with the standard photovoltaic effect on p-n junctions. The photocurrent measures done with OPA prove the first requirement, while the second one requires measures at zero voltage. This aspect will be better analyzed in voltage dependent measurements under continuous light illumination.

For the moment, we can consider the presence of a net stable photocurrent sufficient for implying the presence of BPVE.

In second instance, the wavelength dependence of photocurrent does not correspond to the same trend of photostriction (see the discussion of the previous paragraph). Nonetheless, the presence of photon-generated charges is a mandatory required for photostriction. In lack of a direct wavelength dependence of the latter, we selected as wavelength for the following experiments a value close to the maximum of photocurrent. All the following light illuminations on PMN-PT/Ni heterostructures were done with a continuous 405 nm laser of tunable power, i.e. at a wavelength to the peak of observed photocurrent.

Finally, all photocurrent measurements were taken under pulsed illumination. In FE materials, static measurements of BPVE have similar trends under both pulsed and continuous laser illuminations.[39] We therefore consider this wavelength dependence to be representative of the PMN-PT response also in the case of continuous illumination, as it will be shown in the following paragraphs.

3.2.2. Magneto-optic Kerr effect (MOKE) and X-ray magnetic circular dichroism (XMCD) spectroscopy of pristine PMN-PT/Ni heterostructure

From the result presented in the previous section, it is evident that visible light illumination of proper wavelength is modifying the ferroelectric properties of pristine PMN-PT substrate, showing a net photocurrent, pre-requirement for the photostrictive effect. Once selected the wavelength for light illumination as 405 nm, we moved to study the effects of photocurrent (and therefore photostriction) of PMN-PT on the interfacial Ni layer. This transition metal was chosen among all others available at the deposition chambers due to his large magnetostrictive value among 3d transition ferromagnets (see figure 11 in paragraph 1.2.2. for details).

A 10 nm thick Ni layer was deposited by e-beam evaporation on top of an unpolarized one-sided polished (001) PMN-$_{0.4}$PT 2.5 × 2.5 mm^2 substrate of 0.5 mm thickness from SurfaceNet GmbH supplier, at a base pressure below 1×10^{-7} mbar. At the same pressure, the prepared sample was then capped with an 8 nm thick layer of Au to prevent Ni oxidation and to act as the top electrode for electrical measurements. Then, the unpolished backside of the substrate was coated with a 5 nm thick layer of gold-rhodium (AuRh) using magnetic field sputtering, acting as the backside electrode. All the depositions were performed at room temperature.

After deposition, the samples were first characterized by MOKE magnetometry both with and without the illumination of 405 nm visible light. The magnetic hysteresis loops of pristine PMN-PT/Ni heterostructure were measured by applying an in-plane magnetic field along four different directions according to the crystallographic axis of the ferroelectric substrate. The observed coercive field (H_C) is almost isotropic, with H_C values ranging from 19 Oe along the [100] PMN-PT axis and 23 Oe along the [010] axis, while no changes were observed in the magnetic remanence (M_r/M_s). The recorded loops and polar plots for H_C are shown in figure 33.

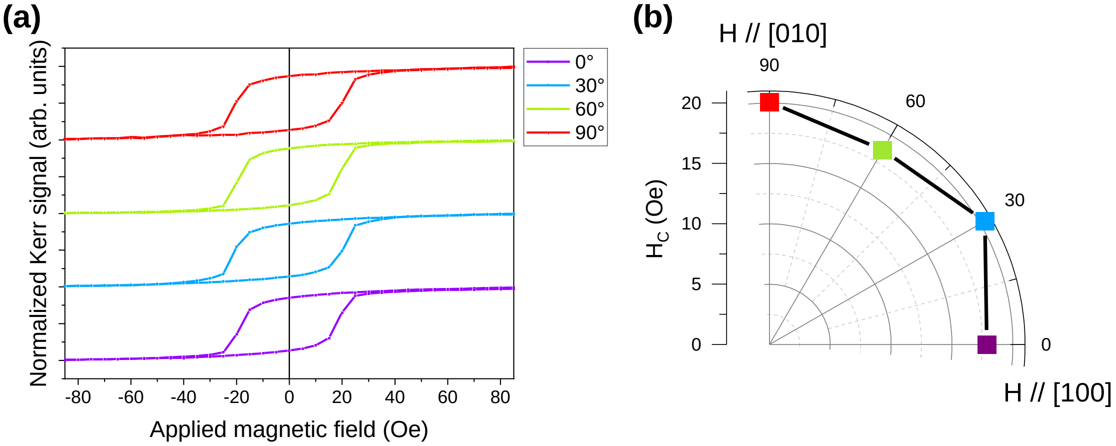

Figure 33: Hysteresis loop (a) and polar plot (b) of the pristine PMN-PT/Ni heterostructure. These measurements showed an in-plane isotropic behavior.

The effects of visible light illumination were then measured by illuminating the sample from the front side, the schematics is shown in figure 34.

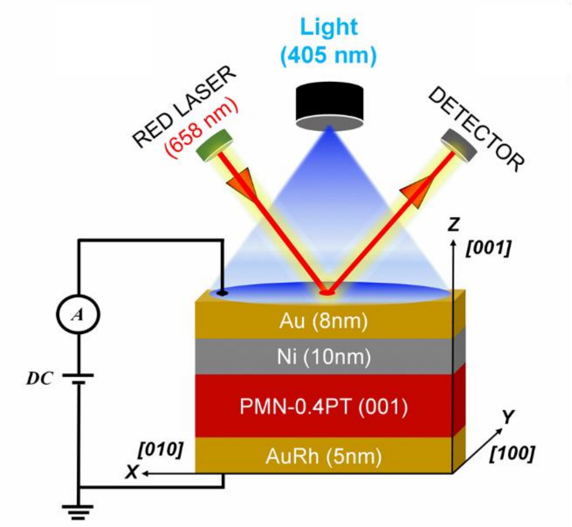

Figure 34: Schematic representation of the PMN-$_{0.4}$PT/Ni heterostructure and experimental setup. A He-Ne laser is used for the MOKE measurements, while a continuous 405 nm laser is illuminating the whole sample surface.

In literature, similar characterizations on multiferroic heterostructures are reported with the illumination being either on the backside electrode or on the side.[40] A comparison between illumination from frontside and backside will be shown later in this paragraph.

Hysteresis loops were recorded as the function of increasing irradiance for the case of applied magnetic field *H* along the [100] and [010] directions. In both cases, a monotonous reduction of the coercive field was observed as a function of the light intensity, as shown in figure 35.

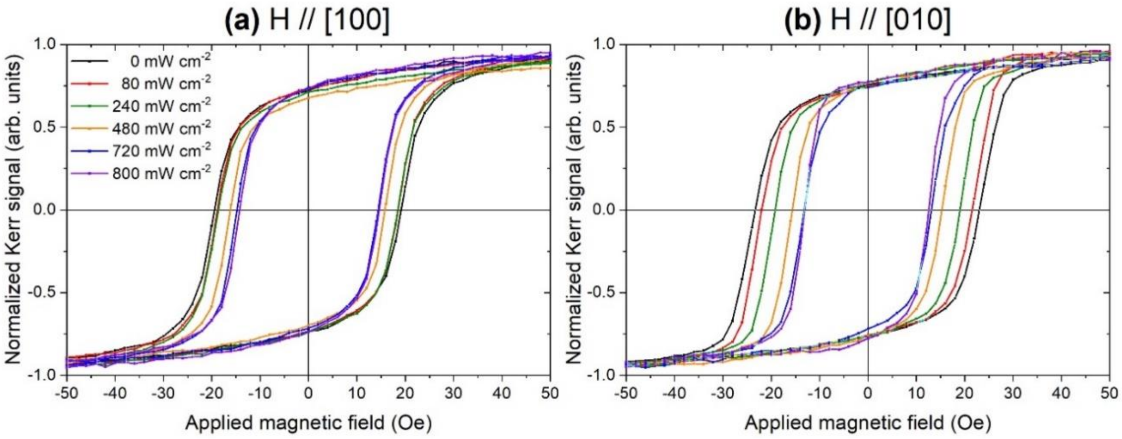

Figure 35: Hysteresis loops measured with the magnetic field applied along the PMN-PT (100) and (010) axis under light illumination of variable power (0–800 mW cm^{-2}).

The reductions of coercive field under 405 nm laser illumination were almost linearly linked to the fluence of light, although the modifications were different along [100] and [010] directions (see figure 35). This can be due to the fact that the effect of light is more sensitive to one particular direction when compared to others due to different magnetic anisotropy contributions of Ni and the effectiveness of photostriction of the substrate in a particular direction.

The magnetic changes under laser illumination were fully reversible and reproducible, with the magnetic signal fully restored after switching the laser off. This can be clearly seen in figure 36, which shows the hysteresis loops both in absence and presence of laser illumination with the magnetic field applied along [010]. It is clearly visible how the coercive field, after being reduced of around 45% under 800 mW cm^{-2} illumination, comes back to its initial value after turning off the laser, proving the process to be a fully reversible.

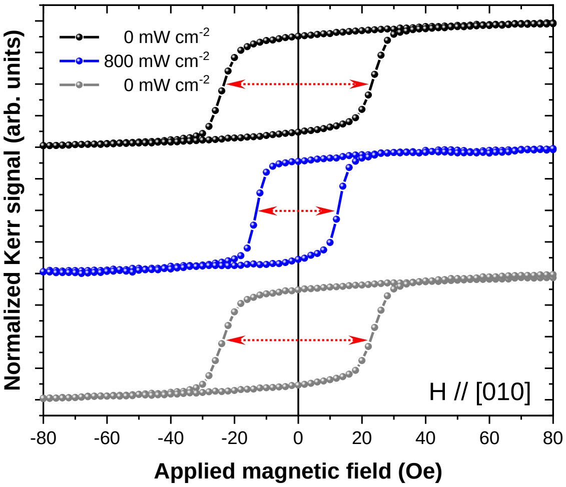

Figure 36: Hysteresis loops of the PMN-PT/Ni heterostructure with no light and under 800 mW cm^{-2} light illumination. The coercive field reduction is fully reversible and reproducible after turning off the illumination.

Finally, figure 37 shows the variation of coercive field as a function of the illuminated electrode in the case of magnetic field along (010) axis. It is quite evident that laser illumination from the backside electrode has less impact on the coercive field modification of Ni compared to the front electrode case, despite maintaining a similar trend. We attribute this to the fact that when the light is being illuminated on the top electrode, which is composed by 8 nm of Au and 10 nm of Ni, the absorption coefficients of Au and Ni are 6.0656×10^5 and 8.1604×10^5 cm^{-1}, by using the formula,[24]

$$\alpha = \frac{4\pi k}{\lambda} \tag{28}$$

where α is the absorption coefficient, k is the extinction coefficient and λ is the light wavelength, we calculate a transmittance percentage in the range of 40-50% for 405 nm illumination. Similar percentages are reported in the articles of N. Ahmad *et al*.[41] and DS Gosh *et al*.[42] Regarding the PMN-PT single crystals, they are considered light transparent in the range from 400 to 5800 nm at room temperature.[43] It is difficult to evaluate with precision the absorption coefficient of PMN-PT because it depends on several parameters, like doping concentration of PT in the material, presence of defects, the light illumination wavelength, etc. In literature one can find a value which ranges from 25 to 40 cm^{-1} for a wavelength of 400-410 nm.[44] With this value a transmittance percentage of roughly 60% [24,45] can be estimated for our crystal. While illuminating from the back, although there are no optical calculations reported for AuRh yet but as it is a metallic alloy, the most of the irradiance of light is expected to be stopped due to high reflectance and low transmittance, therefore giving less interfacial changes at Ni and PMN-PT that results less modification in the Ni magnetic properties. This was experimentally verified by comparing sample illumination from either front or backside, as shown in figure 37. The similar trend and slightly larger modification of coercive field in case of backside illumination confirm that both setups allow the laser illumination to shine the whole volume of the crystal, allowing BPVE to take place.

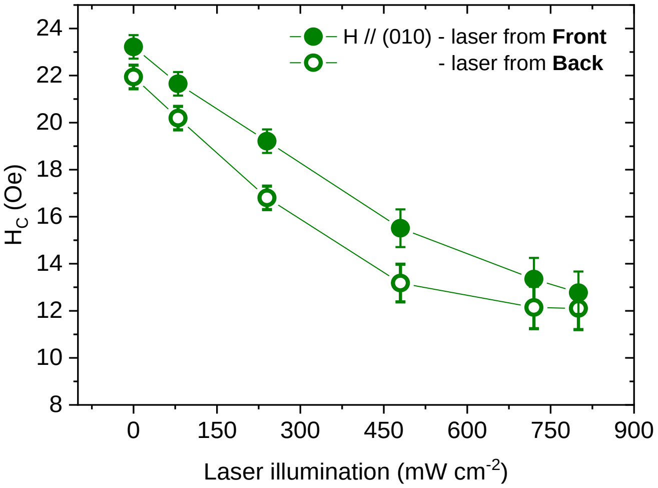

Figure 37: Plot showing the variation of coercive field as a function of irradiance of light impinging from the front electrode (full circles) and from the back one (empty circles).

After MOKE characterizations, absorption spectroscopic measurements were carried out at APE-HE beamline in TEY detection mode, as described in section 2.2.1 of the previous chapter. XAS spectrum at the Ni $L_{2,3}$ edges were recorded and then compared with reference metallic nickel[46] (brown) and NiO[47] (green) spectra (see figure 38). The spectrum of the sample was mostly metallic, but presented some features due to surface oxidation forming NiO, due to a non-ideal Au capping. The detailed features like double peaks of L_2 edge and presence of a shoulder on the right side of L_3 edge are the characteristic symbols of a partial oxidation of nickel.[48]

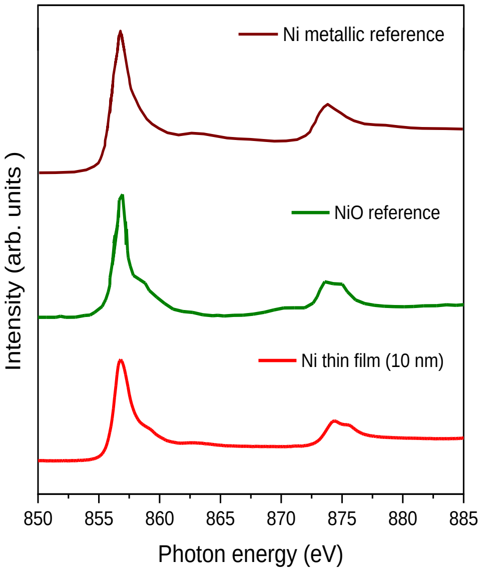

Figure 38: X-ray absorption spectra probed at Ni $L_{2,3}$ edges compared with bulk metallic nickel[46] and NiO[47].

After this, the XAS and XMCD spectra were collected at several different zones of the sample surface, showing no variations of both chemical and magnetic properties, sign of a homogeneous Ni layer. The XMCD measurements were taken both in presence and absence of laser illumination, with the laser at maximum power illuminating through a UV transparent viewport placed in the endstation of the beamline. The resulting intensity on the sample (700 mW cm^{-2}), with part of the intensity absorbed/reflected by the viewport, was evaluated via 3A broadband 10 µW to 3 W thermopile sensor produced by Ophir Optronics. The spectra measured at three different zones of the sample are shown in figure 39.

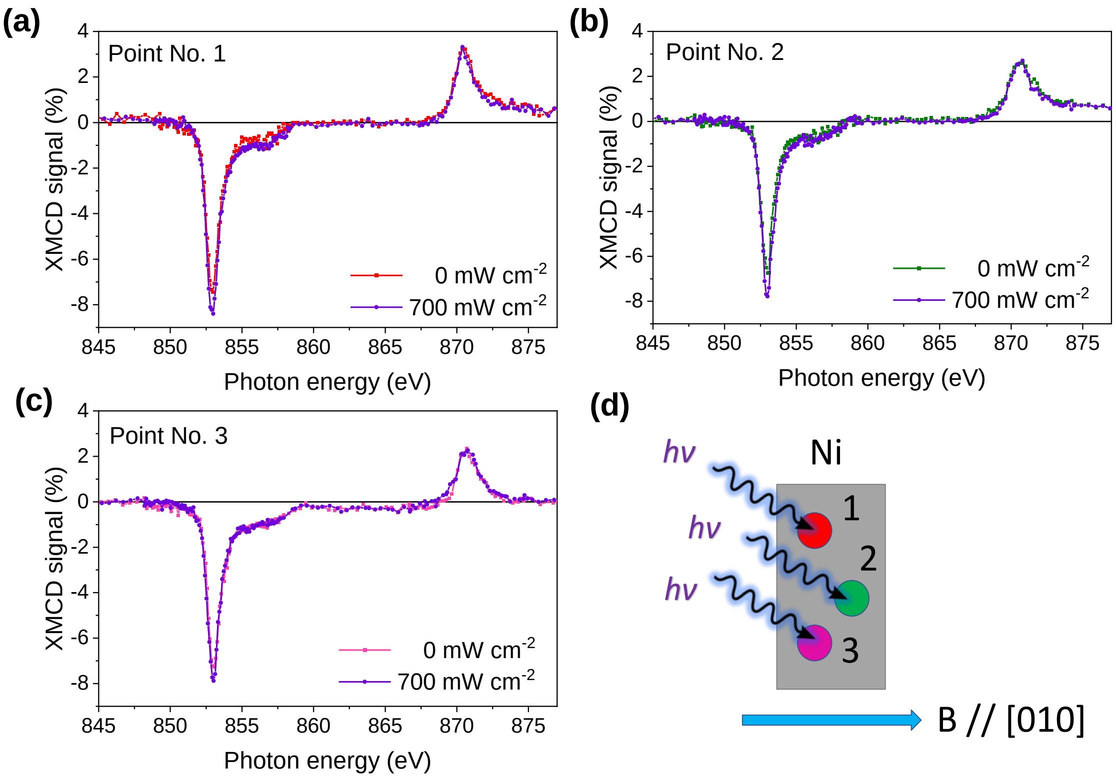

Figure 39: (a,b,c) XMCD dichroic signal at Ni $L_{2,3}$ edges for three zones of the sample as shown in figure **(d)**.

As it can be seen, for all the different probed areas a clear increase of the L_3 edge was found under illumination, while no changes were recorded at the L_2 edge. Figure 40 shows the XMCD spectra averaged over these three measurements.

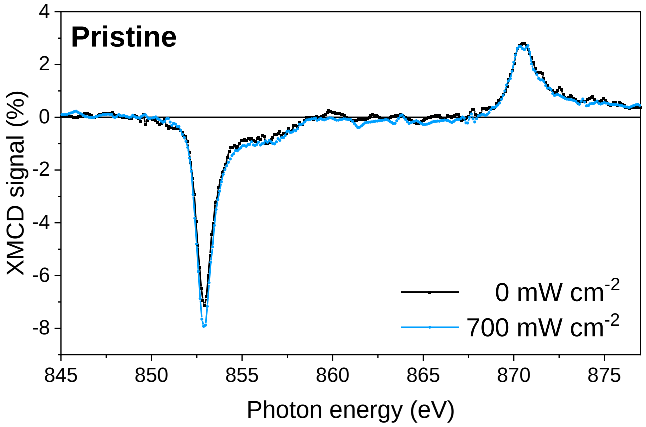

Figure 40: XMCD dichroic signal at Ni $L_{2,3}$ edges in case of pristine PMN-PT/Ni, in absence and presence of light of 700 mW cm^{-2}, applying the magnetic field along [010].

The spectrum shows an L_3 edge XMCD intensity of (7.1 ± 0.1)% with no light and (7.9 ± 0.1)% under illumination, while the dichroic signal at L_2 edge does not change. These signals have been corrected for the 75% degree of circular polarization of the incoming X-rays, as well as the 45° incidence angle. The change in the intensity of L_3 edge and not in L_2 under light illumination is an indication of a modification of the orbital properties of Ni in presence of illumination.[49] This can be quantified via XMCD sum rules calculation[50,51] in order to evaluate the spin (m_{spin}) and orbital (m_{orb}) magnetic moments of Ni for the two cases. In the following, the procedure for sum rules calculation without illumination is quickly described. Sum rules require few steps of data treatment on the experimental curves, since they use three parameters obtained from the integral of the averaged XAS and XMCD spectra. Firstly, a two-step function is subtracted from the [0 to 1] normalized XAS spectrum to remove the L_3 and L_2 edge jumps and to make the background flat for the integration and account for the background of 2*p* → 4(*sp*) transitions.[47] The thresholds for the two-step function are set in correspondence to the peak positions of the L_3 and L_2 edges. The end points of the spectrum were also not flat, so we have used an accordingly increasing values of step function to make it almost flat after subtraction. The two-step like function and the integration of the XAS spectra, after removal of edge-jump is shown in figure 41.

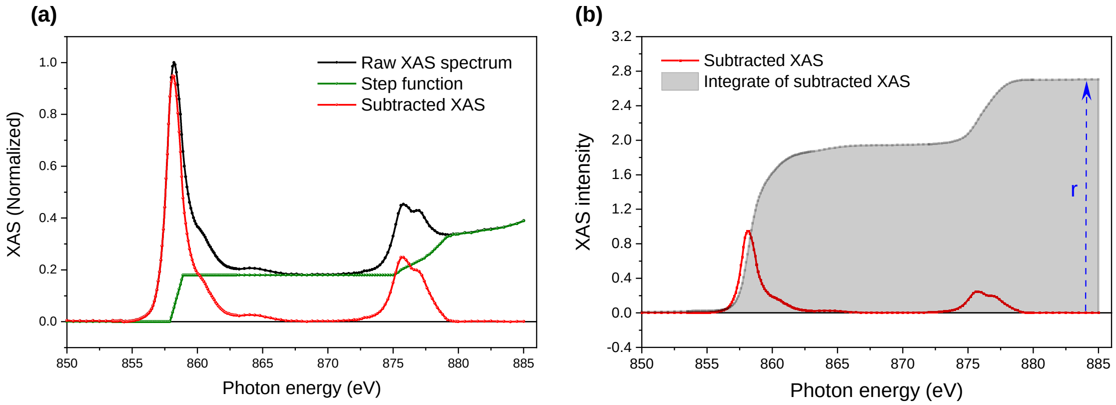

Figure 41: (a) XAS spectra acquired at Ni $L_{2,3}$ edges along with two-step like function and the step function subtracted XAS. **(b)** Integral of subtracted XAS spectrum.

The *r* value labeled in the figure is parameter needed in the sum rules. After this, the integration of magnetic dichroic signal was carried out (see figure 42) to obtain two more parameters, *q* and *p*.

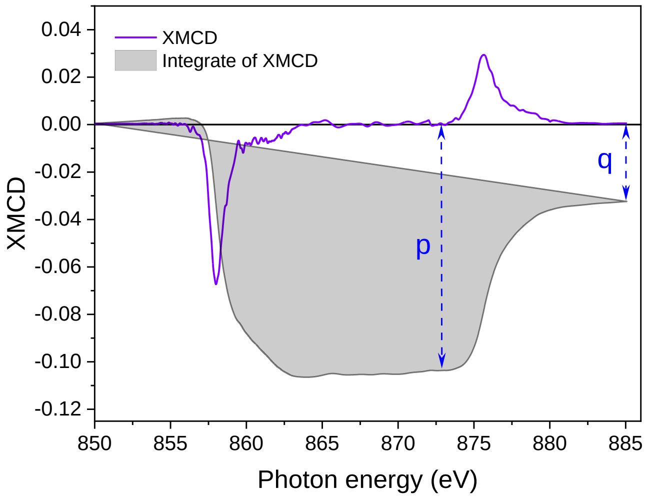

Figure 42: Ni $L_{2,3}$ edges XMCD spectrum and the integration for application in sum rule calculations

Using the values of *r*, *p*, and *q* (see table 2) the orbital and magnetic moments are calculated as,[50]

$$m_{orb} = \frac{-4q(10 - n_{3d})}{3r} \tag{29}$$

and

$$m_{spin} = \frac{-(6p - 4q)(10 - n_{3d})}{r} \tag{30}$$

where n_{3d} is the 3d electron occupation number of the Ni. By taking into account the partial oxidation and *ab-initio* calculations done by Linchtenstein and Katsnelson back in 1998,[52] a value of 8.4 was considered. The obtained values of individual spin and magnetic moments for the cases of light off and on are presented in the table below along with the total magnetic moment and their ratio.

Light intensity	r	p	q	$\boldsymbol{m_{orb}}$	$\boldsymbol{m_{spin}}$	$\boldsymbol{m_{tot}}$	$\boldsymbol{m_{orb/spin}}$
0 mW cm^{-2}	2.8104	-0.1064	-0.0351	0.0266	0.2835	0.3102	0.0940
700 mW cm^{-2}	2.6998	-0.1314	-0.0505	0.0399	0.3474	0.3873	0.1149

Table 2: Table showing the values of the sum rules parameters (*r*, *p*, and *q*), and the calculated values of orbital and spin magnetic moments of Ni thin film with and without laser illumination.

These numbers are comparable to those reported for Ni thin films[53,54] and smaller than those reported for bulk Ni;[55,56] this can be attributed to the partial oxidation of the Ni surface. Here, the critical parameter is in any case the relative comparison of the ratio (m_{orb}/m_{spin}) in presence and absence of light illumination. The relativistic increase of this ratio in presence of light illumination represents the interfacial induced effect by the photostriction of PMN-PT substrate upon light exposure, which is fully reversible and reproducible after tuning off/on the light. The variation of Ni orbital moment upon illumination is a direct spectroscopic evidence of the light induced interfacial strain modifications, therefore connecting the effects of photostriction in PMN-PT substrate to the magnetostriction in Ni thin film.

3.2.3. Photocurrent under continuous laser illumination on pristine and electrically polarized PMN-PT/Ni

The PMN-PT/Ni heterostructure was polarized out-of-plane by sweeping an electric field up to ±6 kV cm^{-1} through the thickness of the sample. The backside of PMN-PT was glued with silver paint and the Au capping acted as top electrode, connected with a thin gold wire. The I(E) curves were recorded by sweeping the electric field along the [001] crystallographic direction from −6 to +6 kV cm^{-1} and then back to zero. The resulting curve is shown in figure 43a. Current-voltage characteristics show well pronounced peaks in correspondence of polarization switching of about ±150 V (corresponding to an electric field of 1.5 kV cm^{-1}), showing stable and reproducible ferroelectric transitions, consistently with what previously reported by our group on similar substrates.[20,57] In fact, the applied electric field causes the displacement of the ions in the ferroelectric and a consequent current flow $\left(j = \frac{\delta P}{\delta t}\right)$. Once switched, the polarization remains stable, as it can be seen from the repeated curves P_{up} and P_{down} in the inset of figure 43a, where no peak is found once the polarization is set. Then the integral, represented by the area under the I(E) curve, is proportional to the polarization P. The obtained strain v/s electric field curve for PMN-PT ferroelectric substrate (which resembles the shape of a butterfly) is shown in figure 43b, it originates generally from three types of effects; normal converse piezoelectric effect of the lattice, and other two comes from switching and movement of domain walls. The strain was found to be maximum near the coercive field values of ferroelectric domains switching for both the positive and negative polarities (84 ppm and 113 ppm for ±1.8 kV cm^{-1}, respectively), and also the nature (compressive or tensile) was inverted at the same point.

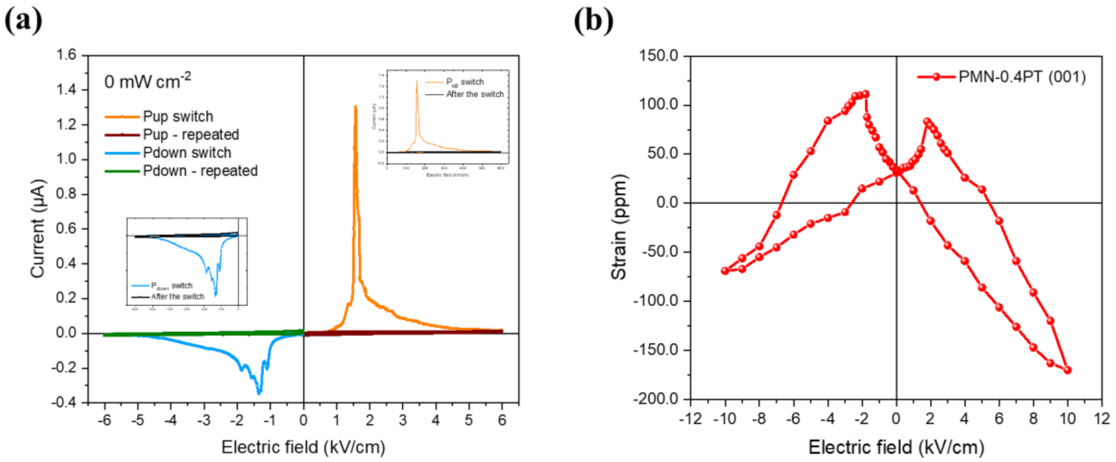

Figure 43: (a) I(V) curves measured across the thickness of PMN-PT substrate. The peaks in the first positive and negative sweep cycles testify the switching of out-of-plane polarization. Repeating the same half cycles twice resulted in no peak, proving that the electrical polarization is remanent (inset). **(b)** Strain-electric field hysteresis loop for PMN-$_{0.4}$PT (001) ferroelectric.

The I(E) curves were then recorded in presence of 405 nm light illumination at different illumination intensities (figure 44a). The laser illumination induced significant changes in the curves. The most noticeable one is the presence of an additional linear slope as a function of the applied bias, whose intensity increases with illumination irradiance. The presence of this slope is a clear sign of free charge carrier generation in the sample, i.e., induction of BPVE. The light induced additional current under 800 mW cm^{-2} illumination, given by the difference between I(E) under illumination and no light, as the function of electric field is shown in the figure 44b. This difference helps in understanding the effects of light illumination on PMN-PT during the polarization switching. Specifically, two main effects can be noticed here: *i*) a linear contribution under bias due to BPVE, and *ii*) an increase of photogenerated current in correspondence to the polarization switching bias. This second point is in agreement with recent photopolarization measurements on similar PMN-PT substrates,[58] where these combined effects were attributed to a net polarization increase when switching the FE state under illumination.

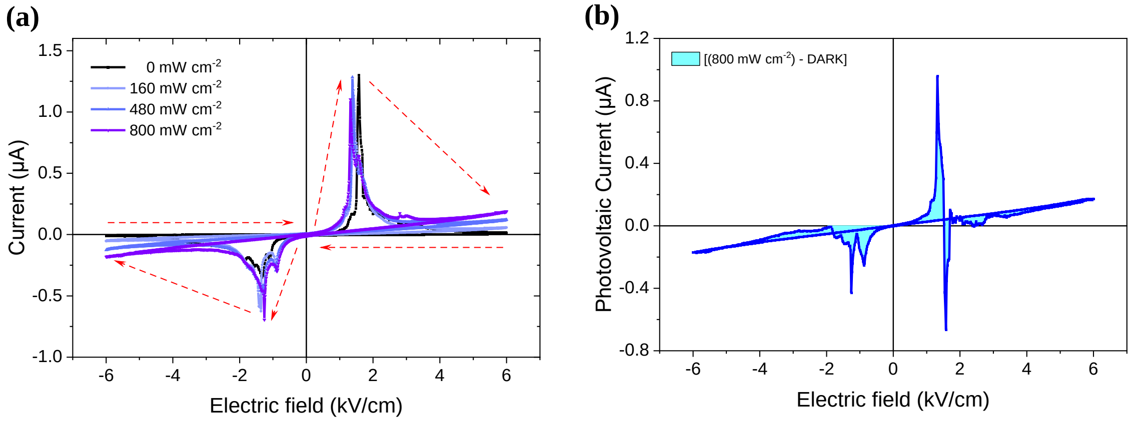

Figure 44: (a) Ferroelectric switching I(E) curves of the PMN-PT/Ni heterostructure under continuous 405 nm laser illumination of variable power (0–800 mW cm^{-2}). **(b)** Photovoltaic current generated in PMN-$_{0.4}$PT (001) substrate, obtained by subtracting the curve taken with no light from the one under 800 mW cm^{-2} illumination.

To determine the electrical state of the substrate under illumination, photocurrent measurements were performed on both pristine and on the two polarization states of PMN-PT. The laser irradiance was set to 800 mW cm^{-2}. The measurements were taken under 1 V of electric filed bias, starting in dark, then switching on the laser for 90 seconds, then switched off for 2 minutes. The resulting photocurrent curves are shown in figure 45a.

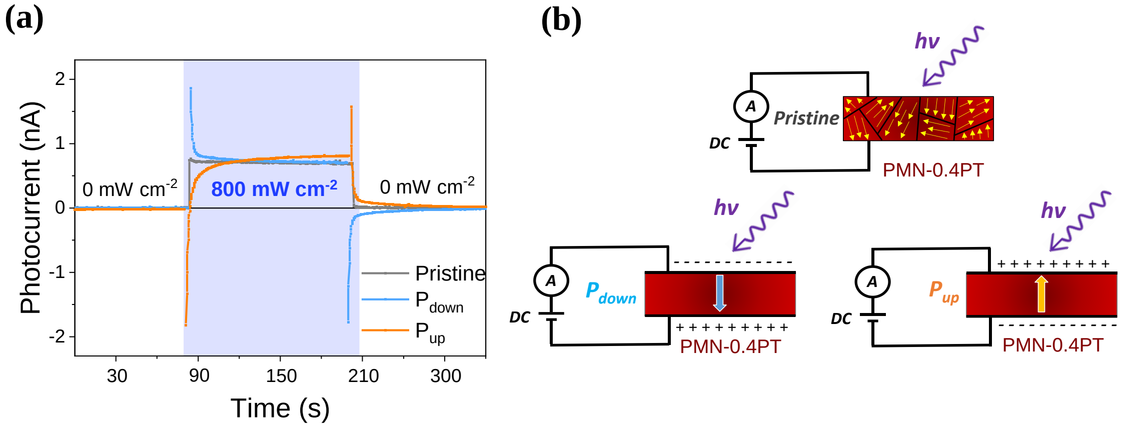

Figure 45: (a) Photocurrent evolution of the PMN-PT/Ni heterostructure as a function of time for three different polarization states (pristine, P_{down} and P_{up}) under 1 V bias. After the 90 s with no light, the sample is illuminated by the 405 nm continuous laser at 800 mW cm^{-2} power (blue area) for 90 s. When the laser is switched off, the photocurrent was measured for additional 120 s. **(b)** Schematic representation of the photocurrent measurements in the three PMN-PT ferroelectric configurations. In pristine state, randomly oriented ferroelectric domains give no net static charges, while for P_{down} and P_{up} states net accumulated charges are present on the top

and bottom electrode of PMN-PT. Under illumination, the filling of the conduction band with photogenerated current induces a variation of the resistance and results, in the case of polarized PMN-PT, in the discharging of the accumulated charges.

In the case of pristine sample, as the light was turned on, an increase in the sample current was observed, due to BPVE, with a value of around 0.7 nA. Once turned off the laser, the initial state was sharply restored. The reproducibility of the generation of a stable photocurrent in pristine PMN-PT was verified by switching on and off the laser several times, as shown in figure 46a. On the other hand, once the FE substrate is polarized, an additional slow dynamic with opposite trends was observed. As the light was turned on, a photocurrent peak of opposite sign (positive for P_{down}, negative for P_{up}) appeared, exponentially decaying toward a steady value comparable to the pristine one. Once the light was switched off, a similar transient effect, but opposite in sign, was observed for both cases, with a relaxation time quite comparable to the one under illumination. These transient effects were observed for all different irradiances of illumination, whose stable current was proportional to the light intensity, and are signature of the presence of a net electric dipole after sample polarization. The case of P_{down} is shown in figure 46b: as it can be seen, a positive peak of photocurrent was measured at each increase of illumination intensity. The steady state value of photocurrent maintained a linear trend for each illumination irradiance. Once the laser was turned off, a negative current was measured, which is the signature of a return to the initial state of charged capacitor due to the polarized state of the substrate.

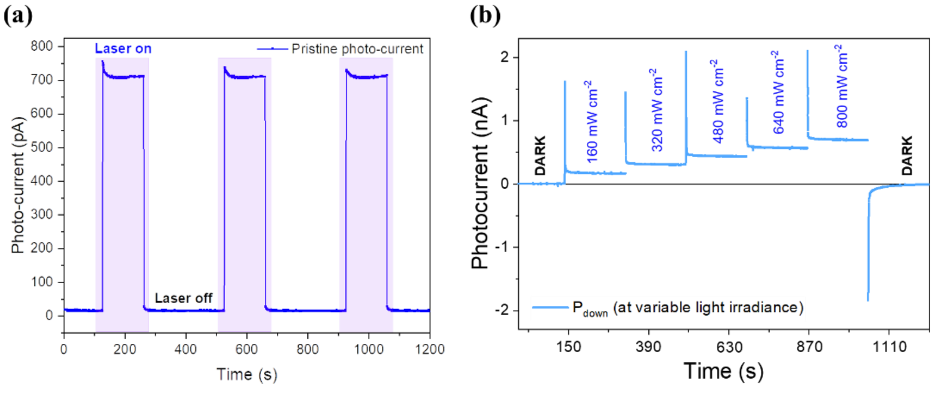

Figure 46: (a) Photocurrent measurement in pristine state of PMN-$_{0.4}$PT (001) under continuous 405 nm laser illumination testifying the reproducibility at 800 mW cm^{-2} and **(b)** P_{down} state under illumination at variable illumination intensities.

As it will be shown in the section 3.2.5 of XRD discussion, the majority of the ferroelectric domains in PMN-PT align along the [001] direction once polarized, with an electric dipole pointing up or down according to the polarization state (figure 45b). This was not the case when the substrate as in pristine state, since the randomly distributed FE domains led to a zero macroscopic electric dipole. When the light illumination is off, no free charge carriers are present in the conduction band of PMN-PT, but only accumulated charges on the electrodes due to the presence of a net electric dipole. When light is switched on, the bulk photovoltaic effect induces the generation of free charge carriers in the conduction band, leading to a net photocurrent. In the pristine case, as the light was turned on, an increase in the sample current was observed due to BPVE, with a value of around 0.7 nA. Once turned off the laser, the initial state was sharply restored. In the polarized state, the charges accumulated at the top and bottom electrodes due to electrical poling effects attract the light induced photogenerated charge carriers, creating a depletion across the electrodes that further triggers the depolarization field in the material,[59] having opposite polarity with respect to the ferroelectric dipole. The transient effects between the two steady states (high resistance in the absence of light, lower resistance under illumination due to photocurrent) is an indication of the current flowing from the accumulated charges on the electrodes, whose sign depends on the direction of the dipole (P_{up} or P_{down}). Once the light is turned off, the photovoltaic effect is stopped because of the non-availability of new photogenerated charge carriers. Therefore, a second transient peak of opposite sign takes place at this stage, with the recovery of the net electric dipole and its accumulated charges at the electrodes. For both polarization states of PMN-PT, the photocurrent reached its steady state after around 45 s, signature of a slow dynamic in the discharging of the substrate. This time dependence of polarized ferroelectrics under illumination is rarely reported in literature and is an additional proof of the structural order present in the polarized cases compared to the pristine case.

Quite recently similar transient effects upon light illumination have been attributed to a coupled mechanism of photovoltaics and pyroelectric effect,[60–62] with the latter linked to the sudden increase of temperature in the substrate induced by laser illumination, depending on its variation in time dT/dt. In our case, we can exclude the presence of any relevant pyroelectric effect in our sample by combining two experimental results. Firstly, no current spikes were measured in the pristine case. Secondly, no current variation at all was observed when under illumination with below-energy gap light, (i.e. red laser illumination) even in the polarized case, as can be seen in figure 47. As a final note, it is worth mentioning that the choice of materials for top and bottom electrodes (in our case Au/Ni and AuRh) plays a role in the intensity of the built-in electric field upon visible light illumination, with consequences on the intensity of both photocurrent and transient currents.[63]

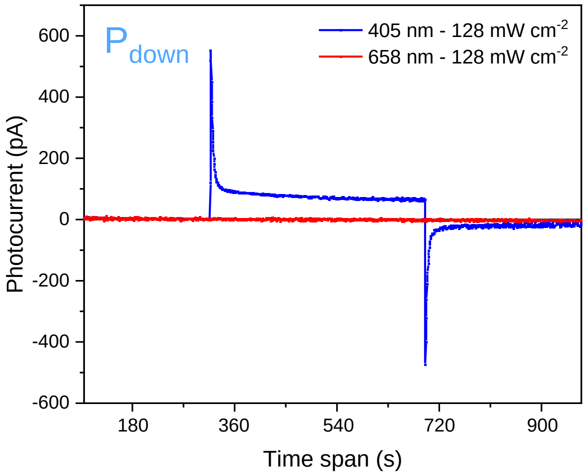

Figure 47: Photocurrent measurement in $_{\text{Pdown}}$ state of PMN-PT/Ni heterostructure under continuous 405 and 658 nm laser illumination of 128 mW cm^{-2} intensity.

Finally, it can be seen from the photocurrent curves of figure 45a that the steady intensity of photocurrent under light illumination is almost identical in the three states of polarization. This is important because it means that the amount of BPVE is unmodified after electrically polarizing the PMN-PT substrate, and therefore from the photocurrent point of view the three states are equivalent.

3.2.4. Visible light-induced effects on the magnetic properties of polarized PMN-PT/Ni

Since the electrical polarization of ferroelectric materials can significantly modify the magnetoelectric coupling at the interface with a ferromagnetic material, it is crucial to analyze the effects of laser illumination on PMN-PT/Ni heterostructures once polarized. Similarly, to the pristine case, the magnetic response of Ni under laser illumination was measured by combining MOKE and XMCD characterizations for both PMN-PT polarizations. In case of spectroscopic measurements, the electrical switching was done *in-operando* at the beamline endstation chamber without removing the sample from the measurement position, assuring the measures to be taken on the same area of the sample. Similarly, in the case of MOKE magnetometry, the samples were electrically switched in air, with the sample fixed to the sample holder in the measurement position. This was done by preparing a specific holder at the mechanical workshop of the institute, it can be seen in the picture 48. Two metallic plates were screwed on a plastic disc working as the top and bottom electrical connections that are attached to the sample using silver paint and Au wire, respectively for the bottom and top electrode. These metallic plates were isolated from the plastic sample holder using ceramic covering of the screws of the plates in order to avoid short-circuit of the electrical connections. The wires for electrical connections were attached to the bottom of the screws using the crocodile connectors. This specific design allowed us to switch the polarization state of the sample and perform MOKE measurements along different crystallographic directions without touching the sample, in order to eliminate any experimental artifact. Also, this allowed us to illuminate the laser from the back and perform magnetic and electrical characterizations.

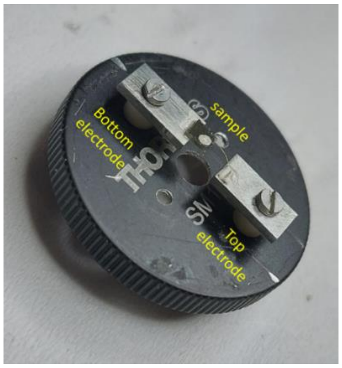

Figure 48: Specifically, designed sample holder for applying bias and perform MOKE measurements while illuminating the sample by visible light from the front or back.

The hysteresis loops recorded along [100] and [010] for the three ferroelectric states (pristine, P_{down} and P_{up}) are shown in figure 49.

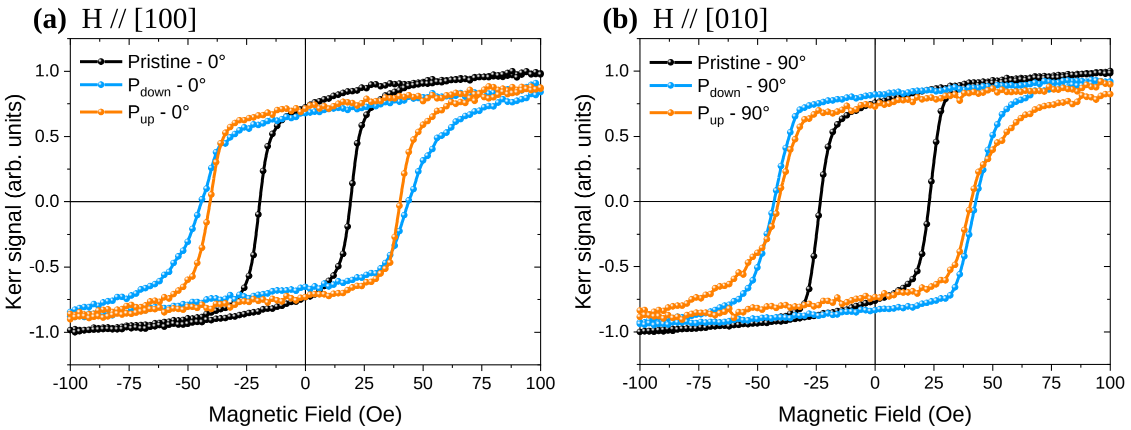

Figure 49: Ni hysteresis loops in the case of pristine and polarized (P_{down} and P_{up}) PMN-PT/Ni heterostructure for magnetic field along **(a)** [100] and **(b)** [010] crystallographic axes of PMN-PT substrate.

The intensity of the loops has been normalized between 0 and 1. A modification in coercive field can be clearly noticed while passing from pristine to electrically polarized cases. This is proof of an important modification of the magnetic anisotropy of the ferromagnetic part of a multiferroic heterostructure induced via electrical biasing, consistent with that reported in literature.[64,65] The coercive field was found to be 44.2 and 40.5 Oe respectively for P_{down} and P_{up} cases when the field was applied along [100] crystallographic axis of PMN-PT, while for the case of [010] the values were 43.4 and 40.9 Oe respectively. We attribute this increase of coercive field with respect to the pristine case to the structural modifications occurred in the PMN-PT due to electrical poling,[66] as it will be discussed and experimentally shown in the following section. This structural change led to a different distribution of lattice parameters at the interface with Ni, with an induced variation of interfacial strain, hence modifying the magnetocrystalline anisotropy. The sample was found to be still isotropic after electrical polarization for both P_{down} and P_{up} states.

The loops were then recorded in presence of laser illumination, can be seen in figure 50.

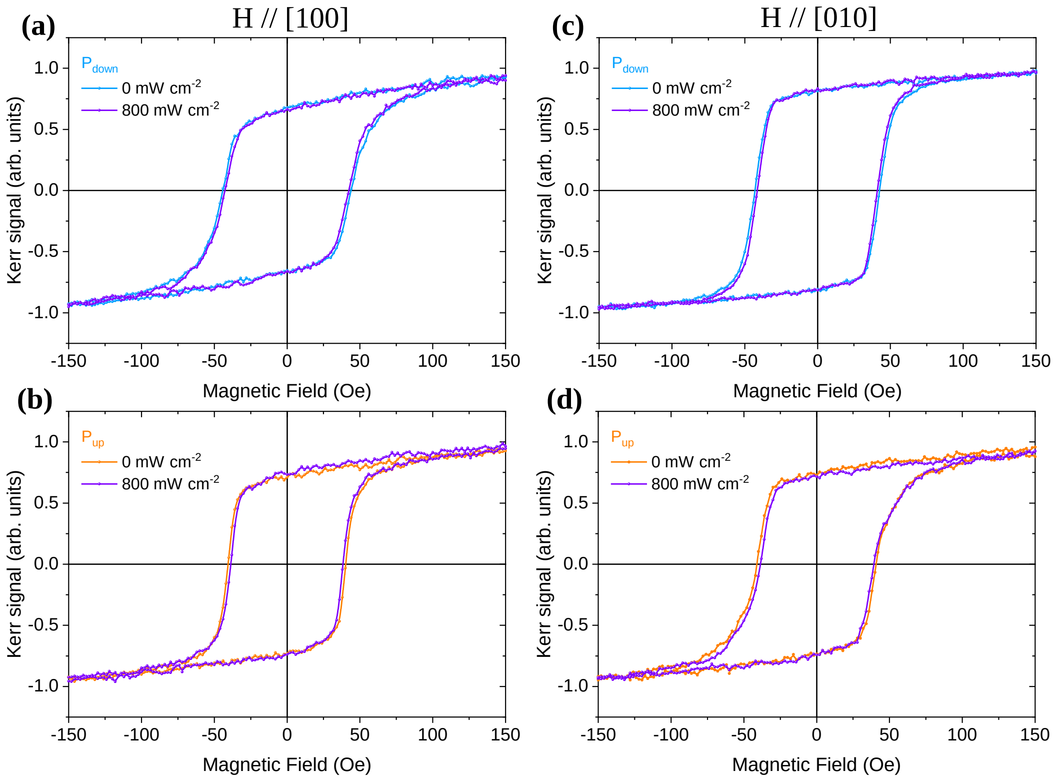

Figure 50: MOKE hysteresis loops of the electrically polarized Ni/PMN-PT heterostructure under dark and 800 mW cm^{-2} laser illumination. **(a, b)** P_{down} and P_{up} loops in case of magnetic field being parallel to [100] and **(c, d)** [010] axis of the substrate, respectively.

It can be seen from the above figure that the effects of light illumination were almost negligible on Ni for both polarization states and along different crystallographic directions of PMN-PT. The coercive field was found to be around 41 Oe for P_{down} and 39 for P_{up} states along [010] axis, leading to a much lower reduction of H_C under illumination as compared to the pristine case.

As for the pristine case, XMCD measurements were carried for both polarizations of the sample under illumination. As a first result, we can notice that XAS spectra were not modified after polarizing the substrate, discarding the possibility of any ion migration from/to the substrate upon polarization, as can be seen in figure 51. Since no spectral evolution was observed along the whole set of measurements, we consider the Ni layer chemically stable in all the studied conditions.

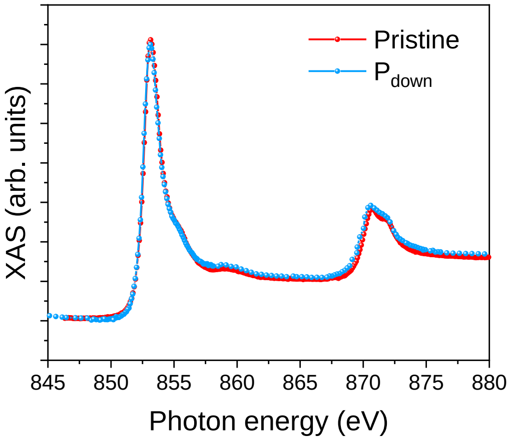

Figure 51: XAS at Ni $L_{2,3}$ edges for pristine and polarized PMN-PT/Ni heterostructure.

Concerning XMCD spectra, almost no detectable changes were found in the dichroic signal under the light illumination for both polarized cases (figure 52), with negligible variations for both P_{down} and P_{up} states. The relatively large noise of the measurements did not allow to properly evaluate the magnetic spin and orbital moments, whose variation, if any, was below our sensitivity.

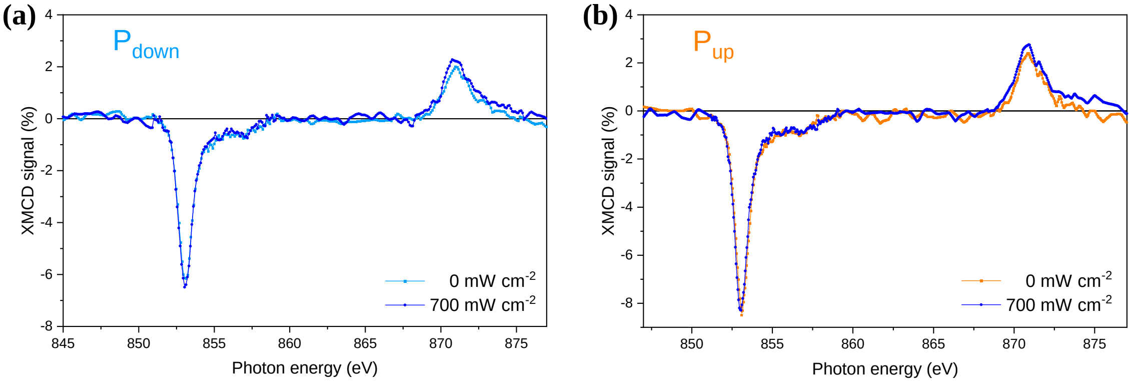

Figure 52: XMCD signal at Ni $L_{2,3}$ edges for the electrically polarized PMN-PT/Ni heterostructure (**a** – P_{down} and **b** - P_{up}) under 0 and 700 mW cm^{-2} laser illumination with the magnetic field applied along [010] axis of the substrate.

Both MOKE and XMCD characterizations show that polarized PMN-PT/Ni present much smaller light-induced modification of the magnetic properties compared to the pristine one, with no relevant differences between P_{up} and P_{down}. Since from the electrical point of view the three states were equivalent, the origin of such different behavior has to be found in the structural differences between pristine and polarized PMN-PT. This will be shown in the following paragraph.

3.2.5. Structural characterizations of PMN-PT substrate

The structural properties of PMN-PT crystals are quite complex and linked to their multidomain nature and composition-dependent phase diagram. In PMN-PT, the concentration of 40% PT corresponds to a majoritarian tetragonal phase,[22] just few percentages over the so-called morphotropic phase boundary, where tetragonal and rhombohedral phases coexist. These aspects will be discussed more in details in the following chapter. Here, a purely tetragonal structure of PMN-PT is used for simplicity, without affecting the analysis of the results.

Figure 53 shows the θ-2θ scan of (002) PMN-PT peak for pristine and P_{down} polarized state of the substrate.

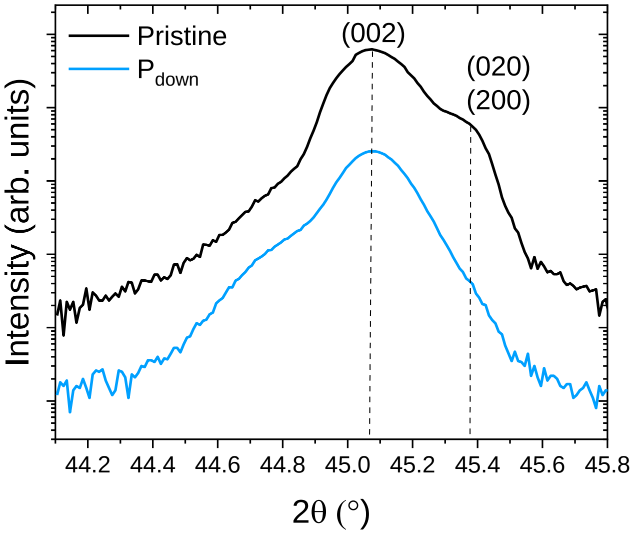

Figure 53: XRD θ-2θ scans for pristine and electrically polarized (out-of-plane - P_{down}) case of PMN-$_{0.4}$PT (001) substrate.

In the pristine state, two peaks are clearly visible, corresponding to the combination of in-plane (020/200) and out-of-plane (002) orientation of domains of the tetragonal unit cell. The difference in intensity between the two peaks is an indicator of a majoritarian population of out-of-plane domains before any voltage application, with nonetheless a non-negligible part of in-plane domains. After setting the polarization to P_{down}, *i.e.* to out-of-plane, the in-plane peak becomes less intense, changing the ratio between the two peaks. Our group previously reported that both the P_{up} and P_{down} states for the same PMN-PT composition are structurally identical.[22] This is consistent with the assumption of a tetragonal structure, since in this case switching from one polarization to the opposite one happens only via 180° rotations of the domains, with therefore no global changes in the in-plane strain.

Finally, reciprocal space maps were recorded around the (013) skew-symmetric reflection for both pristine and polarized cases to better evaluate the variations of domain populations after polarization switching. As it can be seen in figure 54a, the 2D map of pristine PMN-PT is very irregular, with a (013) peak quite broad and a second, less intense peak as satellite of the main one. On the other hand, the map of the P_{down} case (figure 54b) appears more regular, exhibiting a more ordered arrangement and better alignment of the domains, sign of a more homogeneous out-of-plane domain population.

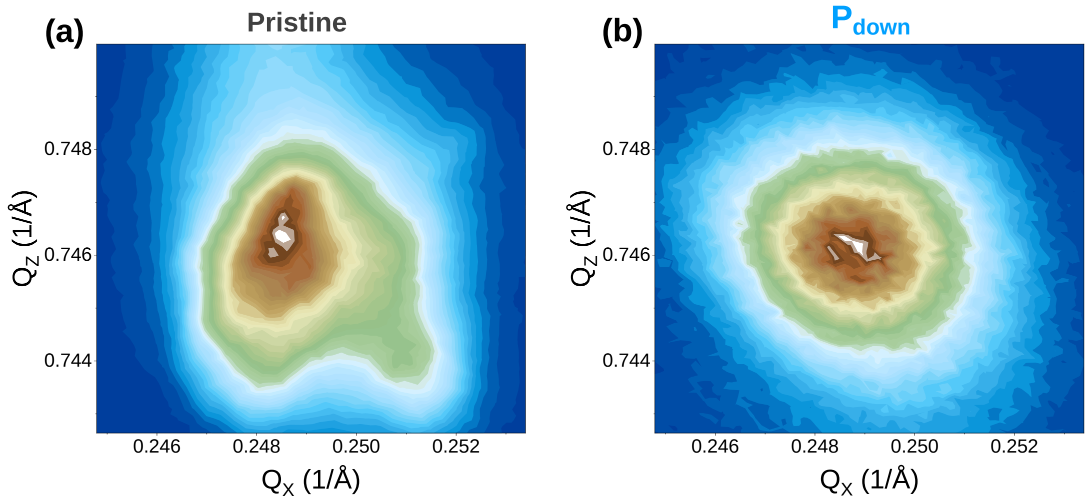

Figure 54: 2D reciprocal space XRD maps for **(a)** pristine and **(b)** P_{down} polarized PMN-$_{0.4}$PT substrate.

Two main conclusions can be drawn from these structural characterizations. Firstly, the modifications taking place in PMN-PT when passing from pristine to polarized state modify the interfacial structural parameters of the heterostructure, and therefore the strain of the thin Ni layer at the interface, with induced modifications in its magnetocrystalline anisotropy. Secondly, the variation of the domain composition between pristine and polarized substrate[68] is a fundamental information to properly understand the different behavior of magnetostrictive Ni layer under illumination. The pristine substrate presents a large portion of in-plane oriented domains, which on the other hand tends to vanish after setting the polarization. Our combination of magnetic, spectroscopic and structural characterizations for both pristine and polarized PMN-PT states shows that the in-plane portion of domains is the main responsible of the photostrictive response under illumination, whose effects propagate to the interfacial magnetostrictive Ni overlayer.

3.3. Conclusions and perspectives

The results presented in this study show visible light illumination as a promising additional stimulus to modify the magnetic and ferroelectric responses of PMN-PT (001) / ferromagnetic metal heterostructures. The effect of visible light illumination on pristine PMN-PT is a reduction of Ni coercive field, driven by the photostrictive contribution of the in-plain ferroelectric domains. Optical, non-thermal control of magnetism in multiferroic heterostructures is a novel and rarely investigated lever.

Our combined experimental analysis unambiguously shows the correlation between ferroelectric domain population and its sensitivity to photo-induced modifications on both ferroelectric and ferromagnetic components of the heterostructure. These results shed light on the delicate energy balance that leads to sizeable light-induced effects in multiferroic heterostructures, while confirming the need of spectroscopic characterizations for identifying the physical origin of interface behavior.

In light of the previous discussion, we can say that the findings of this study add a new lever in modifying the magnetoelectric coupling of multiferroic heterostructures. This paves the way towards using other photostrictive and magnetostrictive materials with optimized combined properties, for instance having faster response time and larger effects that can be suitable for technical applications. Among them, highly magnetostrictive FeGa layer could be one option to be deposited on top of a photo-ferroelectric material. Recently, I have been working and performing MOKE measurements on PMN-PT/FeGa heterostructures in collaboration with INRiM, Torino. The results under light illumination have to be still envisaged in details but shows one of the possibilities to use FeGa layer. In this study, we have used PMN-PT as it is a benchmark ferroelectric material due to high piezoelectric and electro-optic properties but from the panoramic perspective of the topic, people are also looking for lead free materials that can be used to induced photostrictive effects. We are also glancing at some of the possible substitutes like $KNbO_3$, SRO, CdS etc. that have been reported as a highly photostrictive materials. The photostriction is also found in organic materials, that accounts for many prominent examples with larger effects, in which the core mechanism is either light-induced chemical structural changes or different kind of molecular orientations (motion and alignment) under laser irradiation. Hypothetically, one can look for materials that are ferroelectric-photovoltaic and organic-based at the same time in order to have fast time response and bigger effects. Some of the examples to address this issue has been reported for metal organic systems, indeed reported to be ferroelectric. Another promising candidate can be molecular crystals: that are highly light-sensitive and electrically polar at the same time. In these molecular systems, the photostriction is accompanied with a change in magnetic properties, thus could be interesting in studying the magnetostrictive-photostrictive coupling. All this broaden the possibilities to be used for several technical aspects of light-controlled applications in both optics and magnetic straintronics using photostrictive effects.

3.4. Bibliography

[1] F. Wang, S. M. Young, F. Zheng, I. Grinberg, A. M. Rappe, *Nat. Commun.* **2016**, *7*, 10419.

[2] S. Y. Yang, J. Seidel, S. J. Byrnes, P. Shafer, C.-H. Yang, M. D. Rossell, P. Yu, Y.-H. Chu, J. F. Scott, J. W. Ager, L. W. Martin, R. Ramesh, *Nat. Nanotechnol.* **2010**, *5*, 143.

[3] R. Pandey, G. Vats, J. Yun, C. R. Bowen, A. W. Y. Ho-Baillie, J. Seidel, K. T. Butler, S. Il Seok, *Adv. Mater.* **2019**, *31*, 1807376.

[4] T. Choi, S. Lee, Y. J. Choi, V. Kiryukhin, S.-W. Cheong, *Science (80-.).* **2009**, *324*, 63.

[5] K. Uchino, M. Aizawa, L. S. Nomura, *Ferroelectrics* **1985**, *64*, 199.

[6] P. S. Brody, *Ferroelectrics* **1983**, *50*, 27.

[7] B. Kundys, M. Viret, D. Colson, D. O. Kundys, *Nat. Mater.* **2010**, *9*, 803.

[8] B. Kundys, M. Viret, C. Meny, V. Da Costa, D. Colson, B. Doudin, *Phys. Rev. B - Condens. Matter Mater. Phys.* **2012**, *85*, 1.

[9] I. Tatsuzaki, K. Itoh, S. Ueda, Y. Shindo, *Phys. Rev. Lett.* **1966**, *17*, 198.

[10] A. A. Grekov, E. D. Rogach, L. N. Syrkin, *Fiz. Tverd. Tela* **1970**, *14*, 3559.

[11] P. Poosanaas, A. Dogan, S. Thakoor, K. Uchino, *J. Appl. Phys.* **1998**, *84*, 1508.

[12] Z. Jin, Y. Xu, Z. Zhang, X. Lin, G. Ma, Z. Cheng, X. Wang, *Appl. Phys. Lett.* **2012**, *101*, 242902.

[13] H. Wen, P. Chen, M. P. Cosgriff, D. A. Walko, J. H. Lee, C. Adamo, R. D. Schaller, J. F. Ihlefeld, E. M. Dufresne, D. G. Schlom, P. G. Evans, J. W. Freeland, Y. Li, *Phys. Rev. Lett.* **2013**, *110*, 37601.

[14] C. Paillard, S. Prosandeev, L. Bellaiche, *Phys. Rev. B* **2017**, *96*, 45205.

[15] L. Y. Chen, J. C. Yang, C. W. Luo, C. W. Laing, K. H. Wu, J.-Y. Lin, T. M. Uen, J. Y. Juang, Y. H. Chu, T. Kobayashi, *Appl. Phys. Lett.* **2012**, *101*, 41902.

[16] P. Ruello, T. Pezeril, S. Avanesyan, G. Vaudel, V. Gusev, I. C. Infante, B. Dkhil, *Appl. Phys. Lett.* **2012**, *100*, 212906.

[17] D. Schick, M. Herzog, H. Wen, P. Chen, C. Adamo, P. Gaal, D. G. Schlom, P. G. Evans, Y. Li, M. Bargheer, *Phys. Rev. Lett.* **2014**, *112*, 97602.

[18] H. T. Yi, T. Choi, S. G. Choi, Y. S. Oh, S.-W. Cheong, *Adv. Mater.* **2011**, *23*, 3403.

[19] D. Daranciang, M. J. Highland, H. Wen, S. M. Young, N. C. Brandt, H. Y. Hwang, M. Vattilana, M. Nicoul, F. Quirin, J. Goodfellow, T. Qi, I. Grinberg, D. M. Fritz, M. Cammarata, D. Zhu, H. T. Lemke, D. A. Walko, E. M. Dufresne, Y. Li, J. Larsson, D. A. Reis, K. Sokolowski-Tinten, K. A. Nelson, A. M. Rappe, P. H. Fuoss, G. B. Stephenson, A. M. Lindenberg, *Phys. Rev. Lett.* **2012**, *108*, 87601.

[20] G. Vinai, F. Motti, V. Bonanni, A. Y. Petrov, S. Benedetti, C. Rinaldi, M. Stella, D. Cassese, S. Prato, M. Cantoni, G. Rossi, G. Panaccione, P. Torelli, *Adv. Electron. Mater.* **2019**, *5*, 1970033.

[21] A. J. Joseph, N. Sinha, S. Goel, A. Hussain, B. Kumar, *Arab. J. Chem.* **2020**, *13*, 2596.

[22] Z.-W. Yin, H.-S. Luo, P.-C. Wang, G.-S. Xu, *Ferroelectrics* **1999**, *229*, 207.

[23] Yiping Guo, Haosu Luo, Di Ling, Haiqing Xu, Tianhou He, Zhiwen Yin, *J. Phys. Condens. Matter* **2003**, *15*, L77.

[24] X. Wan, H. L. W. Chan, C. L. Choy, X. Zhao, H. Luo, *J. Appl. Phys.* **2004**, *96*, 1387.

[25] X. Wan, H. Xu, T. He, D. Lin, H. Luo, *J. Appl. Phys.* **2003**, *93*, 4766.

[26] C. He, F. Wang, D. Zhou, X. Zhao, D. Lin, H. Xu, T. He, H. Luo, *J. Phys. D. Appl. Phys.* **2006**, *39*, 4337.

[27] Y. H. Bing, R. Guo, A. S. Bhalla, *Ferroelectrics* **2000**, *242*, 1.

[28] A. Makhort, R. Gumeniuk, J.-F. Dayen, P. Dunne, U. Burkhardt, M. Viret, B. Doudin, B. Kundys, *Adv. Opt. Mater.* **2022**, *10*, 2102353.

[29] W. H. Liew, Y. Chen, M. Alexe, K. Yao, *Small* **2022**, *18*, 2106275.

[30] V. Iurchuk, D. Schick, J. Bran, D. Colson, A. Forget, D. Halley, A. Koc, M. Reinhardt, C. Kwamen, N. A. Morley, M. Bargheer, M. Viret, R. Gumeniuk, G. Schmerber, B. Doudin, B. Kundys, *Phys. Rev. Lett.* **2016**, *117*, 1.

[31] X. Zhang, X. Guo, B. Cui, J. Yun, J. Mao, Y. Zuo, L. Xi, *Appl. Phys. Lett.* **2020**, *116*, 132405.

[32] W. Eerenstein, M. Wiora, J. L. Prieto, J. F. Scott, N. D. Mathur, *Nat. Mater.* **2007**, *6*, 348.

[33] Y. Wang, F. Wang, S. W. Or, H. L. W. Chan, X. Zhao, H. Luo, *Appl. Phys. Lett.* **2008**, *93*, 113503.

[34] S. Y. Chen, D. H. Wang, Z. D. Han, C. L. Zhang, Y. W. Du, Z. G. Huang, *Appl. Phys. Lett.* **2009**, *95*, 22501.

[35] M. Zheng, H. Ni, X. Xu, Y. Qi, X. Li, J. Gao, *Phys. Rev. Appl.* **2018**, *9*, 44039.

[36] W. Jin Hu, Z. Wang, W. Yu, T. Wu, *Nat. Commun.* **2016**, *7*, 10808.

[37] Y. A. Genenko, J. Glaum, M. J. Hoffmann, K. Albe, *Mater. Sci. Eng. B* **2015**, *192*, 52.

[38] L. Z. Tan, F. Zheng, S. M. Young, F. Wang, S. Liu, A. M. Rappe, *npj Comput. Mater.* **2016**, *2*, 16026.

[39] Z. Lü, K. Zhao, H. Liu, N. Zhou, H. Zhao, L. Gao, S. Zhao, A. Wang, *Chin. Opt. Lett.* **2009**, *7*, 718.

[40] A. S. Makhort, F. Chevrier, D. Kundys, B. Doudin, B. Kundys, *Phys. Rev. Mater.* **2018**, *2*, 3.

[41] N. Ahmad, J. Stokes, N. A. Fox, M. Teng, M. J. Cryan, *Nano Energy* **2012**, *1*, 777.

[42] D. S. Ghosh, L. Martinez, S. Giurgola, P. Vergani, V. Pruneri, *Opt. Lett.* **2009**, *34*, 325.

[43] X. Wan, H. Luo, J. Wang, H. L. W. Chan, C. L. Choy, *Solid State Commun.* **2004**, *129*, 401.

[44] W. Long, X. Fan, P. Fang, X. Li, Z. Xi, *Crystals* **2021**, *11*, DOI 10.3390/cryst11080955.

[45] C. He, L. Luo, X. Zhao, H. Xu, X. Zhang, T. He, H. Luo, Z. Zhou, *J. Appl. Phys.* **2006**, *100*, 13112.

[46] Y. K. Chang, K. P. Lin, W. F. Pong, M.-H. Tsai, H. H. Hseih, J. Y. Pieh, P. K. Tseng, J. F. Lee, L. S. Hsu, *J. Appl. Phys.* **2000**, *87*, 1312.

[47] L. Soriano, M. Abbate, J. Vogel, J. C. Fuggle, A. Fernández, A. R. González-Elipe, M. Sacchi, J. M. Sanz, *Chem. Phys. Lett.* **1993**, *208*, 460.

[48] A. Dmitriyeva, V. Mikheev, S. Zarubin, A. Chouprik, G. Vinai, V. Polewczyk, P. Torelli, Y. Matveyev, C. Schlueter, I. Karateev, Q. Yang, Z. Chen, L. Tao, E. Y. Tsymbal, A. Zenkevich, *ACS Nano* **2021**, *15*, 14891.

[49] P. Gambardella, S. Rusponi, M. Veronese, S. S. Dhesi, C. Grazioli, A. Dallmeyer, I. Cabria, R. Zeller, P. H. Dederichs, K. Kern, C. Carbone, H. Brune, *Science (80-.).* **2003**, *300*, 1130.

[50] C. T. Chen, Y. U. Idzerda, H.-J. Lin, N. V Smith, G. Meigs, E. Chaban, G. H. Ho, E. Pellegrin, F. Sette, *Phys. Rev. Lett.* **1995**, *75*, 152.

[51] W. L. O’Brien, B. P. Tonner, *Phys. Rev. B* **1994**, *50*, 12672.

[52] A. I. Lichtenstein, M. I. Katsnelson, *Phys. Rev. B* **1998**, *57*, 6884.

[53] J. Vogel, G. Panaccione, M. Sacchi, *Phys. Rev. B* **1994**, *50*, 7157.

[54] S. S. Dhesi, H. A. Dürr, G. van der Laan, E. Dudzik, N. B. Brookes, *Phys. Rev. B* **1999**, *60*, 12852.

[55] O. Eriksson, B. Johansson, R. C. Albers, A. M. Boring, M. S. S. Brooks, *Phys. Rev. B* **1990**, *42*, 2707.

[56] H. Shiozawa, A. Briones-Leon, O. Domanov, G. Zechner, Y. Sato, K. Suenaga, T. Saito, M. Eisterer, E. Weschke, W. Lang, H. Peterlik, T. Pichler, *Sci. Rep.* **2015**, *5*, 15033.

[57] F. Motti, G. Vinai, V. Bonanni, V. Polewczyk, P. Mantegazza, T. Forrest, F. Maccherozzi, S. Benedetti, C. Rinaldi, M. Cantoni, D. Cassese, S. Prato, S. S. Dhesi, G. Rossi, G. Panaccione, P. Torelli, *Phys. Rev. Mater.* **2020**, *4*, 114418.

[58] A. S. Makhort, F. Chevrier, D. Kundys, B. Doudin, B. Kundys, *Phys. Rev. Mater.* **2018**, *2*, 12401.

[59] D. G. Popescu, M. A. Huşanu, L. Trupină, L. Hrib, L. Pintilie, A. Barinov, S. Lizzit, P. Lacovig, C. M. Teodorescu, *Phys. Chem. Chem. Phys.* **2015**, *17*, 509.

[60] A. Zenkevich, Y. Matveyev, K. Maksimova, R. Gaynutdinov, A. Tolstikhina, V. Fridkin,

Phys. Rev. B **2014**, *90*, 161409.

[61] A. M. Glass, D. von der Linde, T. J. Negran, *Appl. Phys. Lett.* **1974**, *25*, 233.

[62] N. Ma, K. Zhang, Y. Yang, *Adv. Mater.* **2017**, *29*, 1703694.

[63] Z. Lu, P. Li, J. Wan, Z. Huang, G. Tian, D. Pan, Z. Fan, X. Gao, J. Liu, *ACS Appl. Mater. Interfaces* **2017**, *9*, 27284.

[64] M. Liu, N. X. Sun, *Philos. Trans. R. Soc. A Math. Phys. Eng. Sci.* **2014**, *372*, 20120439.

[65] M. Liu, T. Nan, J.-M. Hu, S.-S. Zhao, Z. Zhou, C.-Y. Wang, Z.-D. Jiang, W. Ren, Z.-G. Ye, L.-Q. Chen, N. X. Sun, *NPG Asia Mater.* **2016**, *8*, e316.

[66] G. Vinai, B. Ressel, P. Torelli, F. Loi, B. Gobaut, R. Ciancio, B. Casarin, A. Caretta, L. Capasso, F. Parmigiani, F. Cugini, M. Solzi, M. Malvestuto, R. Ciprian, *Nanoscale* **2018**, *10*, 1326.

[67] G. Vinai, F. Motti, V. Bonanni, A. Y. Petrov, S. Benedetti, C. Rinaldi, M. Stella, D. Cassese, S. Prato, M. Cantoni, G. Rossi, G. Panaccione, P. Torelli, *Adv. Electron. Mater.* **2019**, *5*, 1900150.

[68] F. Motti, G. Vinai, A. Petrov, B. A. Davidson, B. Gobaut, A. Filippetti, G. Rossi, G. Panaccione, P. Torelli, *Phys. Rev. B* **2018**, *97*, 94423.

Chapter 4

Ferroelectric thermal treatments: an additional lever in PMN-PT/Fe heterostructure

This chapter provides an insight on the effects of thermal annealing cycles across PMN-PT ferroelectric Curie temperature on the structural and magnetic properties of PMN-PT/Fe multiferroic heterostructures. The objective is to analyze the effects of different time span annealing processes on the ferroelectric domain population of PMN-PT substrate, specifically how the thermal treatments affect the global and local structural order of the ferroelectric substrate and how these changes modify the magnetic anisotropy of interfacial Fe thin film. Similar to the previous chapters, this chapter is organized in sections, as follows: a brief introduction on the state-of-the art literature, followed by the experimental details and results of the study, with a final section on conclusions and future prospects.

4.1. Introduction

As presented along the previous chapters, multidomain PMN-PT single crystals gained a privileged position among all FE materials due to their extraordinarily large electromechanical relaxor properties.[1–3] For this reason, they are applied in medical ultrasound transducers, actuators, micropositioners and other devices. Nonetheless, one of their main flaw for technological implementation is the degradation of ferroic properties and mechanical aging observed under application of an external stimulus.[4–6] The origin of giant piezoelectric phenomenon in PMN-PT is complex and still not fully understood till date; it was initially explained by first-principle calculations with a model based on polarization vector rotation.[7] Whenever the FE domains are uniformly oriented and aligned, the highest values of piezoelectric coefficient are reached, with electromechanical deformations one order of magnitude larger than conventional PZT piezoelectric ceramics.[8,9] Therefore, an effective manipulation of FE domain size and direction can substantially modify the piezoelectric, dielectric, electromechanical and optical properties of these materials. As a result, many methods have been reported in last years to modify the FE domain structure and to play with domain wall engineering, including the use of electric polarization,[10–14] visible light illumination inducing photostriction effect,[15–21] and others.

These exceptional electromechanical properties in lead oxide-based solid solutions are particularly marked when in presence of a phase boundary between the rhombohedral (*R*) and tetragonal (*T*) phases, known as the morphotropic phase boundary (MPB).[22–24] The structural phase diagram of PMN-PT as a function of PT concentration, first presented in section 1.1.2 of chapter 1, is here presented in higher detail. Figure 55 presents the detailed phase diagram as shown by Noheda *et al.*[25] in 2002, where they characterized the structural phase diagram around the MPB region by means of x-ray synchrotron diffraction.

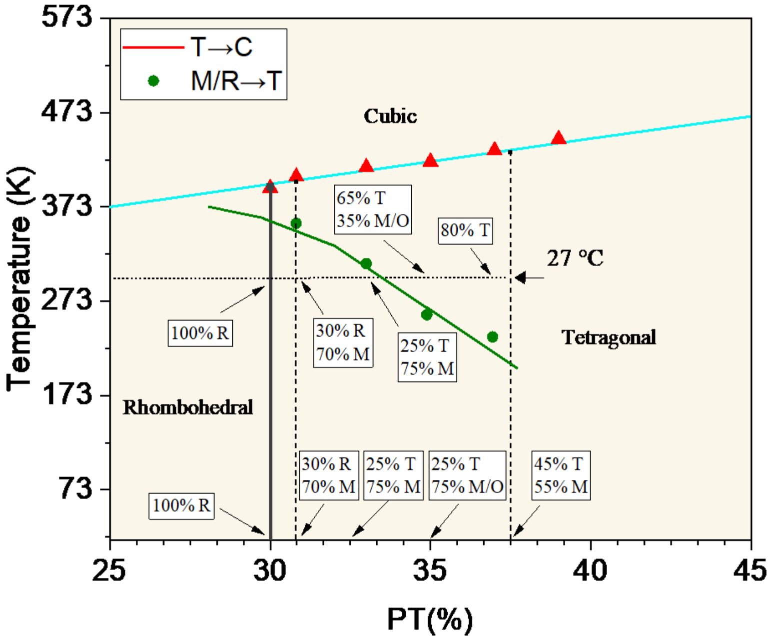

Figure 55: Phase composition schematics of PMN-$_x$PT system reported by Noheda *et al.*[25]

Hangbo *et al.*[26] also performed Landau-like phenomenological theory and calculated free-energy expansion parameters for PMN-$_{0.3}$PT using the temperature-dependent polarization curves along the out-of-plane [001] and in-plane [011] axis for the *R* and *T* phases. They found good agreement with experimental data in the temperature regions near the *T* and *R* phases, but had deviations at higher temperatures, i.e. in the cubic phase region. This was attributed to the fact that the model did not take into account the contribution of polar nanoregions (PNRs). PNRs are small uniformly polarized regions over a local, nanometric scale, present in PMN-PT crystals, which have been proved to play a key role in both piezoelectric and electromechanical giant responses.[27–30] Although the Landau theory failed to fully describe diffusive dielectric properties in relaxor ferroelectrics due to the presence of PNRs, it can be still adopted to describe the behavior of relaxor-based ferroelectrics in the ferroelectric regime. As already discussed, the large effective piezoelectric response is attributed to the easy rotation of polarization vector in the MPB composition, in which *R* and *T* phases coexist and bridging monoclinic phases can appear.[22,31,32] The temperature variations of the in-plane and out-of-plane unit cell parameters for the specific case of PMN-$_{0.36}$PT are presented in figure 56 as an example of the temperature dependent structural transitions that can take place in PMN-PT in presence of MPB.[32]

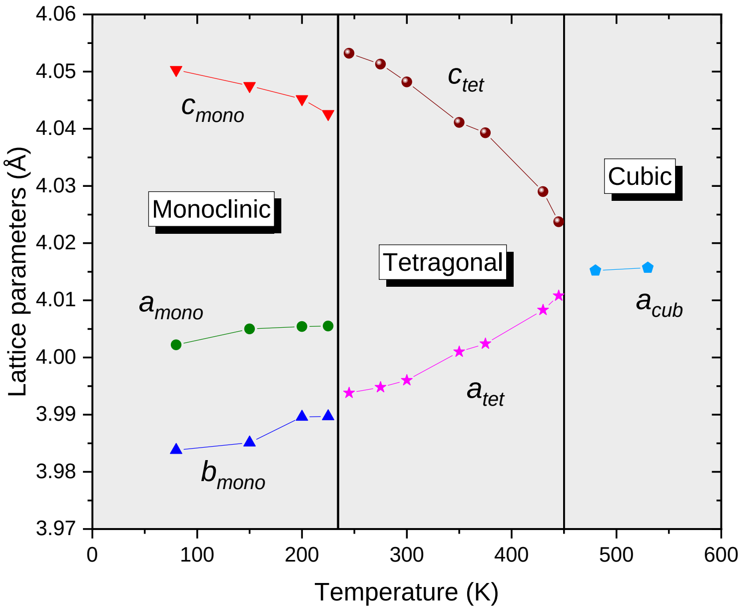

Figure 56: PMN-$_{0.36}$PT lattice parameter evolution as the function of temperature as shown by A.K. Singh and D. Pandey.[32]

Hangbo *et al.*[33] reported the PMN-$_{0.36}$PT (001) phase transition from orthorhombic (*O*) to tetragonal (*T*) around -15°C and calculated the temperature-dependent polarization, spontaneous strains, and dielectric properties, confirming the co-existence of these two phases in a small temperature range; this was considered as an indication of the possible presence of sort of metastable phases across the temperature transitions, here for instance the presence of a monoclinic phase as an adaptive one due to the interfacial mismatch between co-existing *O* and *T* phases. In addition, they reported a large value of temperature-dependent shear piezoelectric constant d_{15} = 1500 pC/N close to room temperature, indicating potential applications in transducer applications. Very recently, T. Rojac[34] discussed the implications of the polar structure on the piezoelectric response of PMN-PT ferroelectrics, including the role of PNRs, domain walls, and the effects of chemical composition as the function of varying temperature. The article shows the role of local polarization rotations and Pb-atom positional disorder, particularly when near the MPB, in explaining the large piezoelectric response.

This brief overview on the temperature dependencies of PMN-PT shows how complex its phase diagram is once temperature variations are taken into account. The picture becomes even more complex when ferroelectric domain directions and polar nanoregions are considered. In this framework, such characterizations have usually been done on pure PMN-PT substrates or ceramics, *i.e.* without including a ferromagnetic layer at the interface. In other words, the possibility of modifying the magnetic properties of a multiferroic heterostructure by optimizing the structural properties of PMN-PT substrates via thermal treatments is at present a fairly unexplored route. This could result particularly interesting for applicative purposes, since thermal treatments are one of the possible methods to both tune the structure and ferroelectric domain orientation and to reduce the mechanical fractures and aging of PMN-PT[35–38] once crossing the FE Curie temperature T_C. The transition from FE domains to a cubic structure and backward upon cooling is responsible for a re-organization of the domains, and can lead to modifications on the concentration of local defects or domain reorientation.[39–41] This can be used to good advantage in multiferroic heterostructures for tuning the FM interfacial properties via interfacial magnetoelastic coupling. This approach has been exploited in heterostructures with $BaTiO_3$ (BTO) as FE substrate. For instance, Motti *et al.* showed in the case of LSMO/BTO heterostructure that electric field cooling from cubic to *T* phase induces a substantial reorientation of the domains in the out-of-plane direction at room temperature.[42] Other systems including LSMO/BTO,[43] Fe_3O_4/BTO[44], SRO/BTO[45] and Ni/BTO[46–48] showed how temperature dependent structural transitions can tune the magnetization of the interfacial FM layer. Finally, regarding PMN-PT/FM system, in 2017, Y. Zhang *et al.*[49] showed the possibility of modifying the properties of Fe_3O_4 deposited on PMN-PT substrate showing strong interfacial mechanical coupling between the magnetic and ferroelectric phases.

In this framework, the work of this chapter focuses on how thermal treatments of PMN-$_{0.4}$PT (001) substrates affect their structural and ferroelectric properties at room temperature, and how they modify the magnetic properties of interfacial Fe thin film. PMN-$_{0.4}$PT composition is out of the MPB region, being in the *T* one (see figure 55), thus in theory with less complex structural characteristics. Nonetheless, here we show how different annealing times lead to variations in the domain direction and composition, together with improvements in the crystalline quality at both macroscopic and microscopic level.

4.2. Results and discussions

The characterization of the PMN-PT substrates was realized by combining XRD and micro-Raman spectroscopy measurements along the different stages of annealing, whereas MOKE measurements were taken to characterize the in-plane magnetic anisotropy of Fe film. In the following paragraphs these steps will be presented and discussed.

4.2.1. X-ray diffraction analysis of PMN-PT substrate

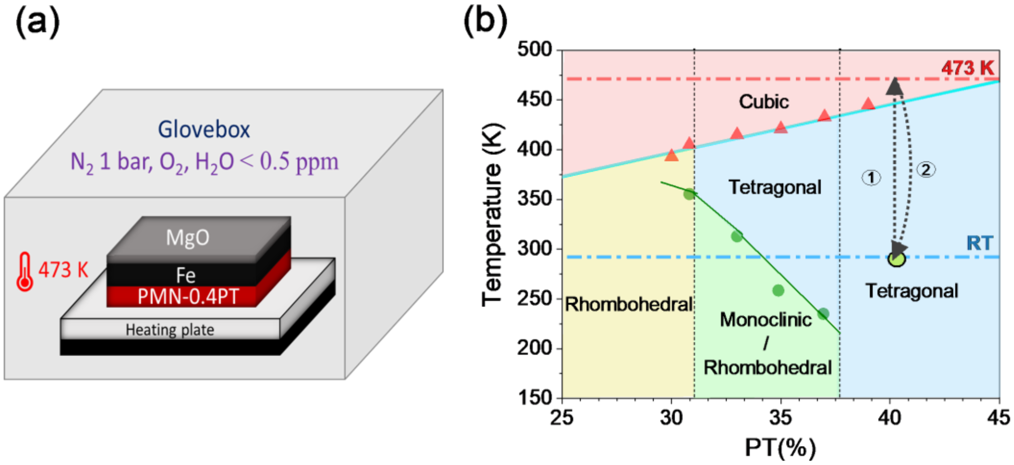

Figure 57: (a) Schematics of thermal treatment setup of PMN-$_{0.4}$PT/Fe heterostructure with heating in glovebox. **(b)** PMN-$_x$PT phase diagram;[25] dashed arrows indicate the thermal treatment process, going from room temperature (RT) up to 473 K, crossing the structural transition (1) then back to RT (2). Horizontal dashed lines indicate the two critical temperatures of the thermal treatment.

The structural properties of one-side polished bare PMN-$_{0.4}$PT (001) FE substrate of 2.5 × 2.5 mm^2 with thickness of 0.5 mm were studied using XRD analysis. The measurements were repeated for the pristine unannealed case and after two different time span annealing. The substrate underwent thermal treatments inside a N_2 filled MBraun glovebox in inert atmosphere (O_2, $H_2O < 0.5$ ppm) (figure 57a). The heating was done in glovebox in order to minimize the interactions with oxygen upon heating and cooling cycles to avoid uncontrolled natural oxidation at the surface. PMN-PT was annealed on a heating plate up to 473 K with controlled heating and cooling ramps of 40 K/min and ~35 K/min respectively. 473 K is a temperature large enough to cross the first order phase transition point for PMN-$_{0.4}$PT substrates, being its Curie temperature T_C at ~ 460 K, as shown in figure 57b. The heating and cooling cycles were repeated twice on the same piece with different annealing time span, 15 min during the first one (from now on, annealing 1) and an additional 180 minutes for the second case (annealing 2).

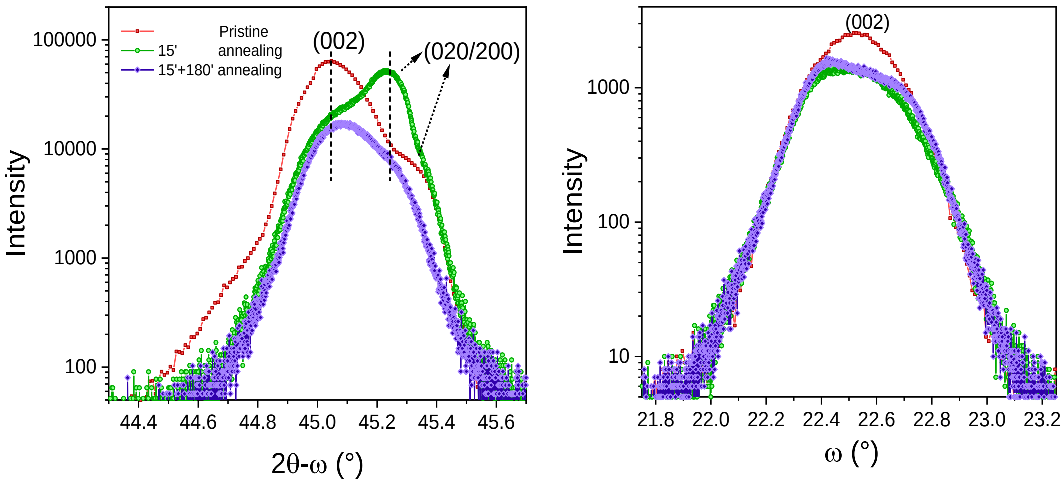

Figure 58: XRD **(a)** 2θ-ω and **(b)** rocking curves (ω-scan) for pristine, post annealing for 15 and 180 minutes of bare PMN-$_{0.4}$PT (001) substrate.

The symmetric XRD 2θ-ω scans and rocking curves of (002) peak of a bare 2.5 x 2.5 mm^2 PMN-$_{0.4}$PT substrate along the thermal processes are shown in figure 58. Two subsequent heating steps took place, with the sample left at 473 K first for 15 min (green curve) and then for additional 180 min (violet curve). At RT (red curve), the profile shows two main peaks indicating the presence of a double domain orientation, one out-of-plane (002) and one in-plane (200/020) for the tetragonal phases at 45.07° and 45.25°, respectively. The rocking curves shown in Figure 58b taken at the (002) Bragg plane showed that, after the first round of 15’ of annealing, there was a decrease of the Full-width half maximum (FWHM) of the curves ($0.147 \pm 6 \times 10^{-4}$) as compared to the pristine unannealed one ($0.323 \pm 9 \times 10^{-4}$), indicating an improvement in the quality of the crystalline structure. After the second round with additional 15’+180’ of annealing, the FWHM increases ($0.269 \pm 1\times10^{-4}$), with an intermediate value in-between the previous two. These values of FWHM were obtained by fitting the rocking curves with cumulative Voigt fits and similar trend is observed in figure 58b for the bare PMN-$_{0.4}$PT (001) substrate.

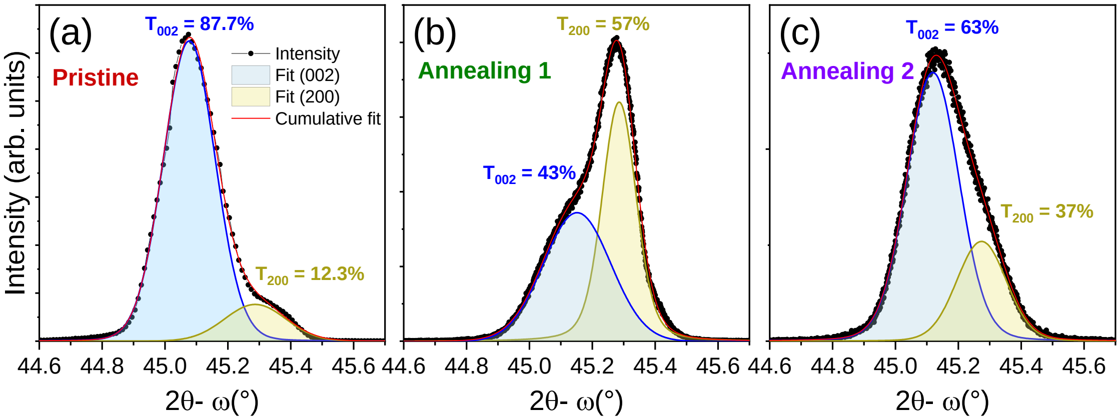

Figure 59: XRD 2θ-ω scans along with the fitting of (002) and (200)/(020) contributions for the pristine unannealed and after two thermal treatments.

From these peaks, by using the Voigt fitting and a quantitative phase analysis of the relative intensities of the two peaks present in the symmetric 2theta-omega scans (figure 59), we have depicted the relative percentages of the amount of out-of-plane (T_{002}) and in-plane domains ($T_{020/200}$) of the tetragonal structure, which is found to be 87.7% and 12.3% respectively for the unannealed pristine case, and 43% and 57% after the first 15’ annealing treatment. Therefore, a substantial increase in the population of in-plane domains due to thermal treatment is reported. It is possible to evaluate the lattice parameters of the tetragonal structure, being $(c)_{tet}$ for (002) at 45.07° equal to (4.022 ± 0.001) Å and $(a=b)_{tet}$ for (002/020) at 45.25° equal to (3.9936 ± 0.001) Å, in good agreement with what reported in literature.[50,51] Increasing the temperature up to 473 K for 15 minutes, a switch of the two peak intensities takes place, with the in-plane component (200/020) becoming predominant compared to the out-of-plane component (002). In this case, the lattice parameters were found to be 4.0201 and 4.0025 Å, respectively, *i.e.* a reduction of *c* and increase of *a* lattice parameter with respect to the pristine unannealed case. After the additional 180’ annealing, the contribution of the in-plane component reduces, with the presence of out-of-plane dominant peak at 45.14° (i.e. $c = 4.0146$ Å) and in-plane peak at 45.27° with $(a=b) = 4.002$ Å.

This procedure was repeated for PMN-$_{0.4}$PT/Fe heterostructure to verify of a similar trend of modification upon thermal treatments takes place. This was done to verify the reproducibility of the annealing treatment on the evolution of the ferroelectric domain populations and to discard any major role potentially played at the interface by Fe/MgO thin films. The results of the XRD measurements are shown in Figure 60.

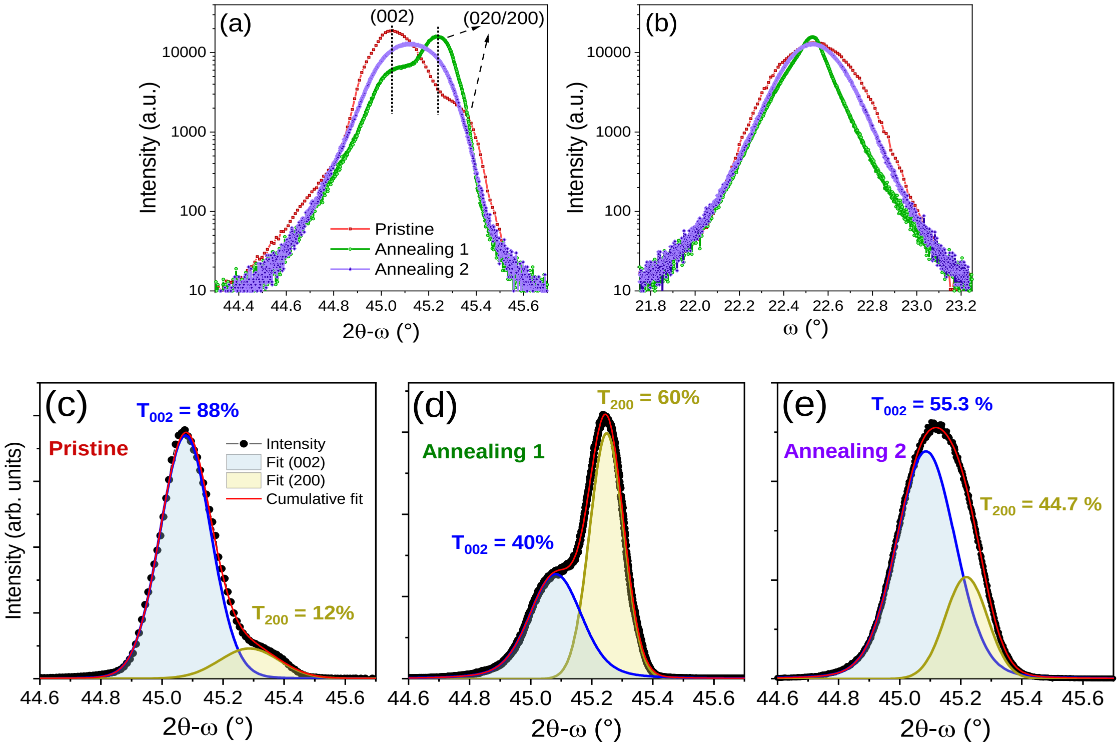

Figure 60: XRD **(a)** 2θ-ω, **(b)** rocking curve (ω-scan) for pristine, post annealing for 15’ (annealing 1) and 15+180 minutes (annealing 2) of PMN-$_{0.4}$PT/Fe heterostructure along with the Voigt fitted curves **(c-e)**.

In this case, the calculated out of-plane $(c)_{\text{tet}}$ and in-plane $(a = b)_{\text{tet}}$ lattice parameters for both Bragg planes (200) and (002/020) are 4.022 and 3.993 Å, respectively. After increasing the temperature up to 473 K for 15 minutes, the reversal of the peak intensities is confirmed, with the in-plane component (200/020) becoming predominant compared to the out-of-plane component (002). After annealing 1, $(c)_{\text{tet}}$ and $(a = b)_{\text{tet}}$ lattice parameters were found to be 4.020 and 4.002 Å, respectively. Once annealed at 473 K for additional 180 minutes, XRD scans confirm a recovery of the majoritarian out-of-plane main peak. This means that by keeping the sample five times longer at a temperature of 473 K, the tetragonal structure of PMN-$_{0.4}$PT reorients itself entirely out-of-plane following the (002) crystallographic direction.

By using the quantitative phase analysis of the relative intensities of the two peaks present in the 2θ-ω scans (figure 60c-e), we retrieved the relative percentages of the amount of (T_{002}) and ($T_{020/200}$) domains of the tetragonal structure, which is found to be 88% and 12% respectively for the unannealed pristine case, and 40% and 60% after the first 15' annealing treatment. The system again went back to its initial state after an additional annealing of 180 minutes, showing a consistent control of annealing treatment on different pieces of PMN-PT.

The 2-dimensional XRD reciprocal space maps (RSMs) recorded asymmetrically around the (103) reflection for the bare PMN-$_{0.4}$PT (001) substrate in the three conditions is shown in (figure 61).

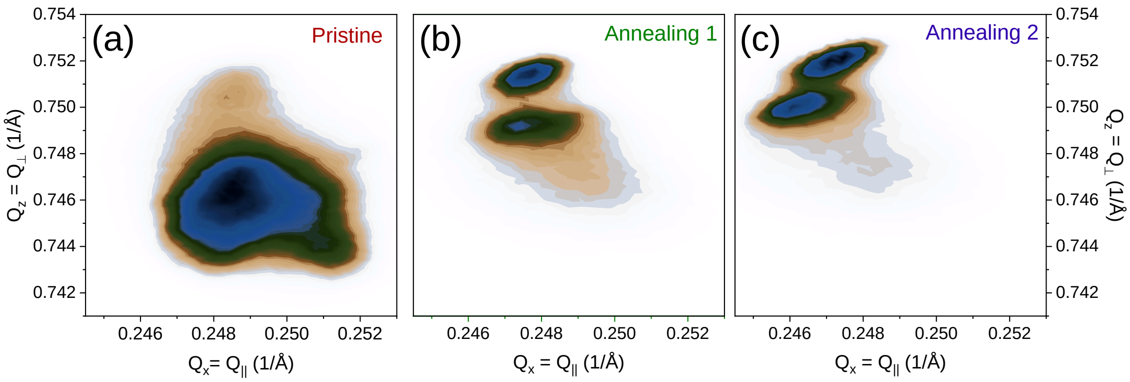

Figure 61: Two-dimensional reciprocal space maps (2D-RSMs) of PMN-$_{0.4}$PT for **(a)** pristine and after thermal treatments, *i.e.* **(b)** 15'annealed (annealing 1) and **(c)** 15'+180' annealed (annealing 2).

The reciprocal space map around (103) reflection of the unannealed pristine sample shows an inhomogeneous distribution of the diffracted intensities in both Q_x and Q_z directions of the reciprocal space. Furthermore, the presence of diffuse scattering around the maxima indicates the presence of crystalline disorder due to lattice defects such as clusters of point defects and/or linear defects such as dislocations. The latter are often associated with the coexistence of polar nanoregions (PNRs) and chemically ordered clusters, leading to intrinsic short- and long-range disorder.[52–54]

The two annealed cases present different patterns of the diffracted intensity distribution, with common characteristics. Firstly, we can notice a sharp separation of two maxima, indicating the formation of two well separated crystalline domains with a net reduction of the diffuse scattering all around them. All of these crystalline domains are characterized by a different status of lattice strain and tilt (i.e., overall structure) due to thermal treatment. Hence, this can modify the interfacial coupling when coupled with a FM layer in different manners.

4.2.2. Micro-Raman Analysis on pristine and annealed PMN-PT/Fe

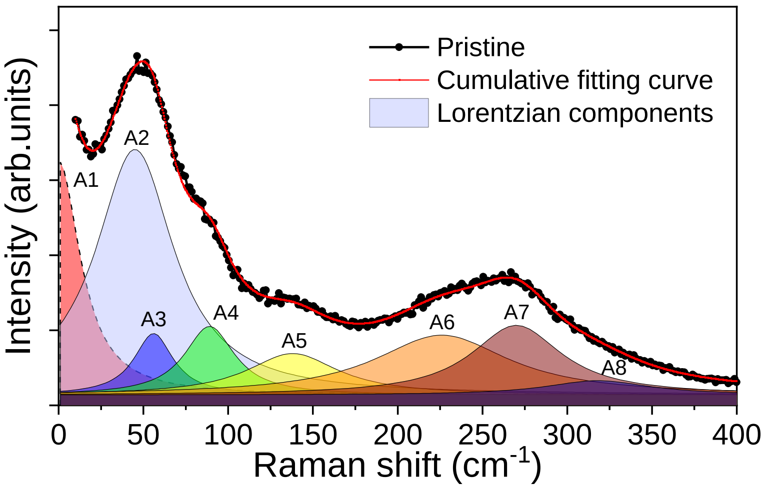

Figure 62: Raman spectrum of pristine unannealed PMN-$_{0.4}$PT/Fe heterostructure along with the fitted Raman modes A2-A8 and fitting curve (red).

The lattice modes at a local scale of PMN-$_{0.4}$PT heterostructure were studied using micro-Raman analysis. Micro-Raman spectra were collected on the pristine PMN-$_{0.4}$PT/Fe heterostructure in the spectral range from 10 to 410 cm^{-1}, with a spectral resolution of 3 cm^{-1} and a probed area of 3 μm^2. An example of spectrum is shown in figure 62, with the fitting curve, obtained by combining eight Lorentzian peaks in correspondence to the main features of the spectrum. An index 'Ai' is attributed to each peak. The Raman shifts of the fitted peaks are consistent with what reported in literature.[55] The peaks labelled from A2-A8 are associated with the vibrational modes of the system. The modes at lower frequencies (A2 and A3, at 43 and 50 cm^{-1}, respectively) are attributed to the lifting of degeneracy of the low wavenumber modes of PMN, associated to the variable elemental composition of the B site of perovskite structure of PMN-$_{0.4}$PT. The other peaks A4 (88 cm^{-1}) and A5 (137 cm^{-1}) are attributed to the lattice modes while, the peaks A6 and A7 at 220 and 266 cm^{-1}, respectively corresponds to the oxygen vibrations.

To completely analyze the local symmetry of PMN-PT sample, Raman spectra were collected by tuning the incident and scattered light polarization with a combination of polarizers and rotators. Several spectra were collected as a function of the sample crystallographic axis orientation and of the relative orientation between polarization and sample axes. By selecting the intensity of each peak as a function of the reflected conditions, polar plots are obtained, giving information on both the local level of crystalline order and on the isotropic or anisotropic response of the selected peaks.

The spectra were observed for three different configurations (figure below):

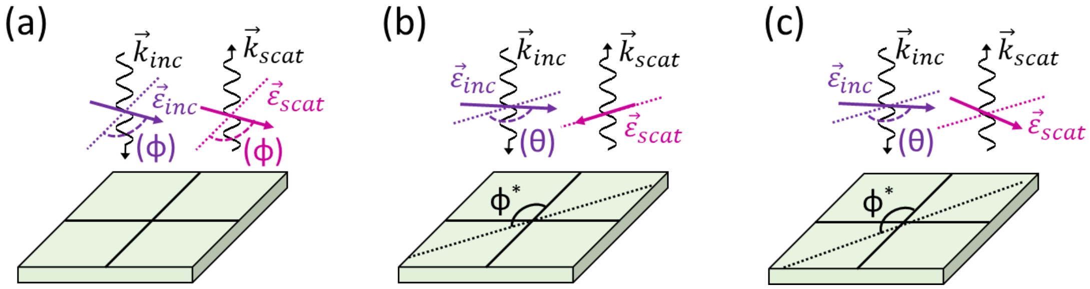

Figure 63: Three different setup configurations for collecting Raman measurements.

a) the polarization of both incident and scattered beams was set to vertical; the spectra collected for the polar plot were taken while rotating the crystallographic sample direction φ ($\varepsilon_{inc} = (\varphi)$, $\varepsilon_{scat} = (\varphi)$);

b) the rotation of the sample axis was set at a selected $\boldsymbol{\varphi^*}$ value, corresponding to a high symmetry direction defined from the trend measured with a) configuration; the incident beam polarization was rotated by a variable angle θ, while the scattered one was set to vertical, *i.e.*, parallel to $\boldsymbol{\varphi^*}$ direction ($\varepsilon_{inc} = (\varphi) + \boldsymbol{\varphi^*}$, $\varepsilon_{scat} = \boldsymbol{\varphi^*}$);

c) the rotation of the sample axis was set at a selected $\boldsymbol{\varphi^*}$ value; the incident beam polarization was rotated by a variable angle θ, while the scattered one was set to horizontal, *i.e.*, orthogonal to $\boldsymbol{\varphi^*}$ direction ($\varepsilon_{inc} = (\varphi) + \boldsymbol{\varphi^*}$, $\varepsilon_{scat} = 90° + \boldsymbol{\varphi^*}$).

The combination of these three sets of angular dependent characterizations allows having a rather complete picture of the phononic modes present in the heterostructure, exploring all the elements of the polarizability tensor accessible in the adopted backscattering configuration.

The polarization angular dependent Raman spectra for pristine unannealed and after first annealing of PMN-$_{0.4}$PT/Fe heterostructure in the three described configurations is shown in figure 64.

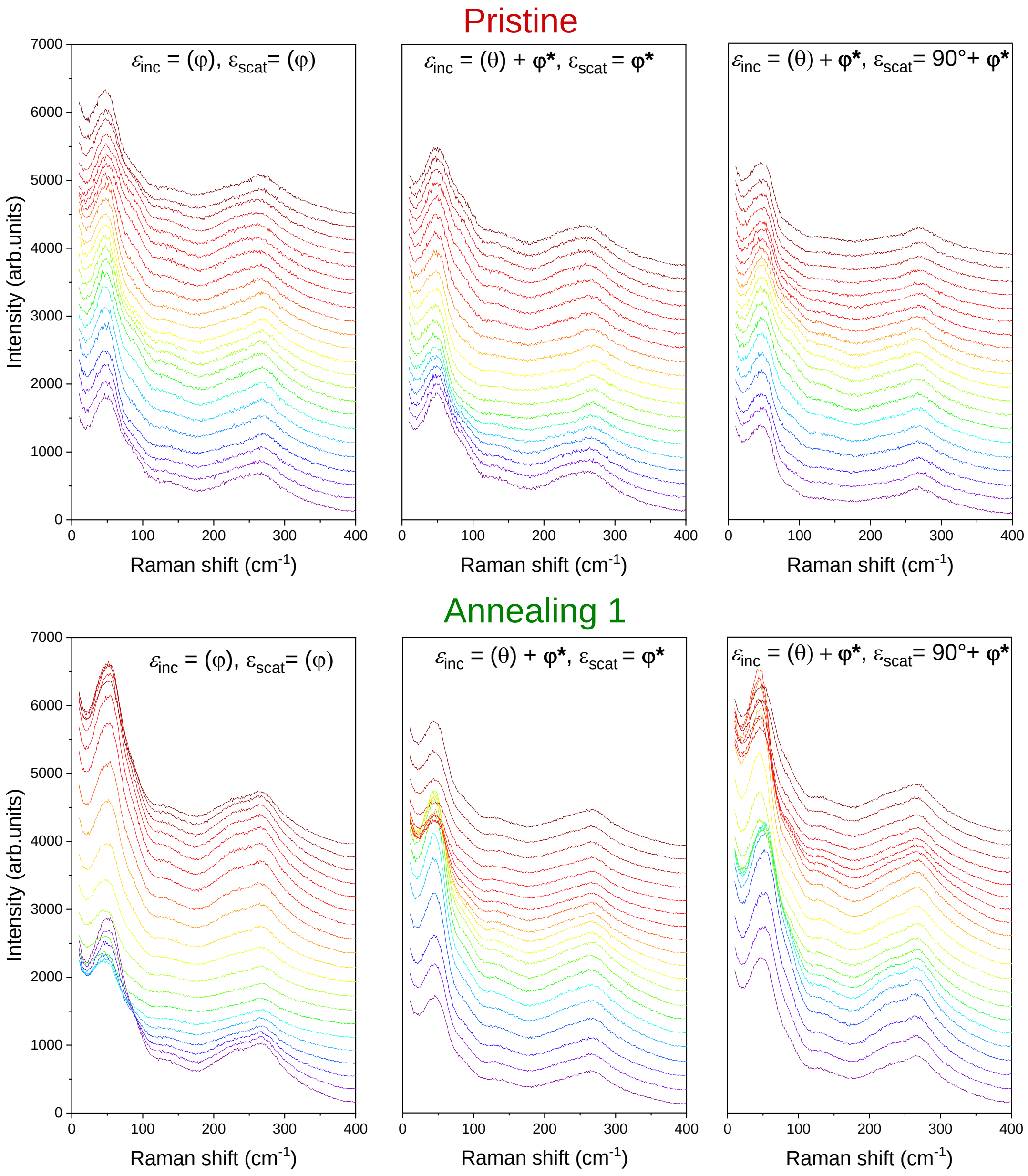

Figure 64: Comparative Raman study, spectra acquired in three different configurations at the frequency range of 10 to 410 cm^{-1} for PMN-$_{0.4}$PT/Fe heterostructure for pristine unannealed and annealed cases.

For the pristine unannealed case, in the first $\varepsilon_{inc} = (\varphi)$, $\varepsilon_{scat} = (\varphi)$ configuration, no significant modifications of the spectra in the frequency range from 50 to 270 cm^{-1} was observed as the function of sample rotation. Similarly, also in the two other optical configurations the modifications of the spectra when changing the polarization orientation were not particularly marked. On the other hand, in the case of the annealed sample a shift in the peaks was noticed.

To better underline the relative modifications of the Raman spectra as a function of the probed angles, we show in Figure 65 the variations of the Raman spectra to a chosen angle, together with the polar plots as a function of the angle for the A3 lattice mode.

Pristine

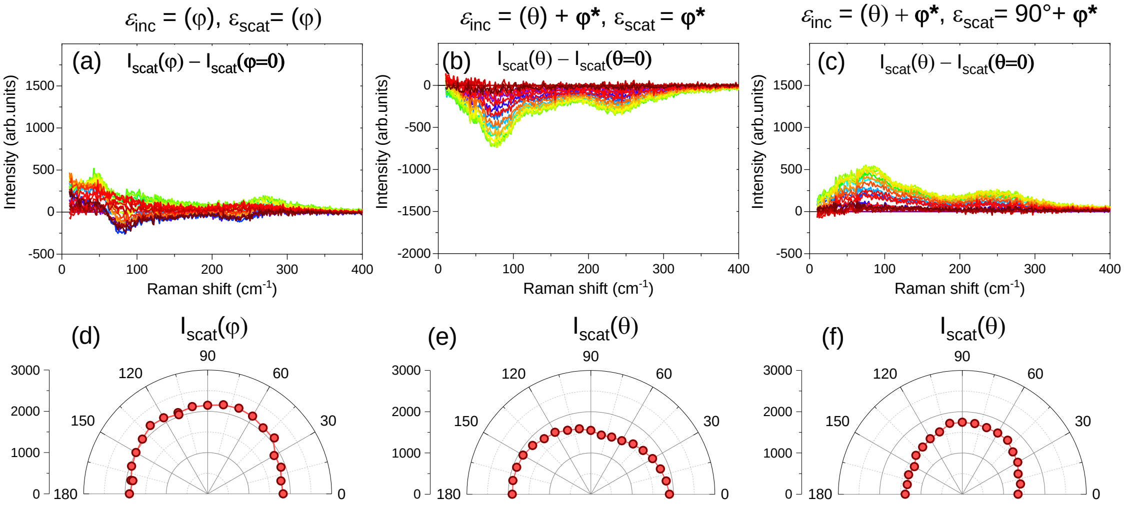

Annealing 1

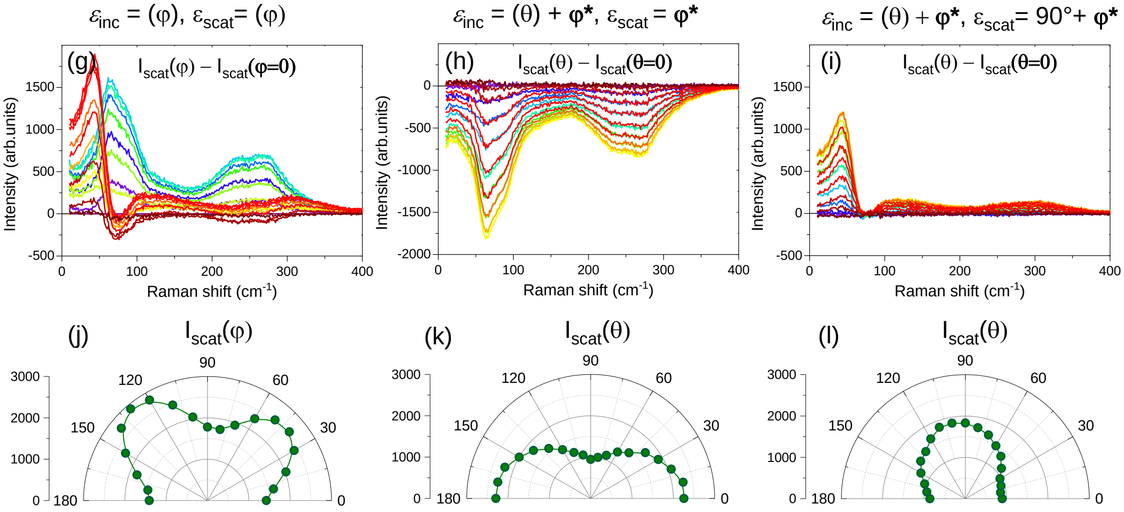

Figure 65: Polarization angular dependent Raman spectra of PMN-$_{0.4}$PT/Fe heterostructure for (top, a-f) pristine unannealed and (bottom, g-l) after annealing 1 case. Figures (a-c, g-i) show the spectral variations in the three configurations, while polar plots (d-f, j-l) present the A3 mode as a function of the rotating angle.

Raman peak intensity is expected to vary/shift as the function of $cos^2\theta$ in accordance with the angle of rotation θ of the sample. It depicts the relation and dependence of light polarization with the crystallographic directions of ferroelectric domains. In the pristine state we observe almost no changes in the Raman modes as a function of both θ and φ, with polar plots almost perfectly isotropic. This means that the sample structure lacks a polarization dependence in the response of the phononic modes and it is an indication of a lack of order in the probed area. This can be ascribed to a large presence of local defects and an average randomly distribute lattice orientation in the three directions. The lack of feature variations is reported through the whole Raman spectrum, with differential curves which present faint features for the three optical configurations. Same cases were observed for the other two $(\varepsilon_{inc} = (\varphi) + \boldsymbol{\varphi^*}, \varepsilon_{scat} = \boldsymbol{\varphi^*})$ and $(\varepsilon_{inc} = (\varphi) + \boldsymbol{\varphi^*}, \varepsilon_{scat} = 90° + \boldsymbol{\varphi^*})$ configurations in the pristine sample, indicating that the ferroelectric domains in the pristine state are randomly distributed along both in-plane and out-of-plane directions. This is consistent with the highly dispersive 2D-RSM measured with XRD and shown the in previous section. It indicates a case of very weak polarization dependence, which is a hint of polycrystalline/highly disordered structure so that the scattering volume contains many orientations.

On the other hand, a well-defined polarization dependence is observed for the annealed case. Differential curves present important variations, especially pronounced on the low Raman shift modes, as it can be seen in the differential curves of figure 65g-i. Once plotted as a function of the intensity of specific lattice modes, the anisotropic behavior of the annealed sample becomes evident. Figure 65j-l show the polar plots for the A3 lattice mode. A well-defined 2-fold and 4-fold symmetries can be seen in the three configurations, indicating a well-defined symmetry of the mode, clearly responding to the polarization direction. Similar anisotropic angular dependences were observed also for lattice modes A2 and A5 and oxygen vibrational A7 mode (figure 66, 67, and 68 respectively). In this case again we find a good consistency with XRD measurements: the increased crystalline quality is reflected on a well-defined local phononic response of the heterostructure.

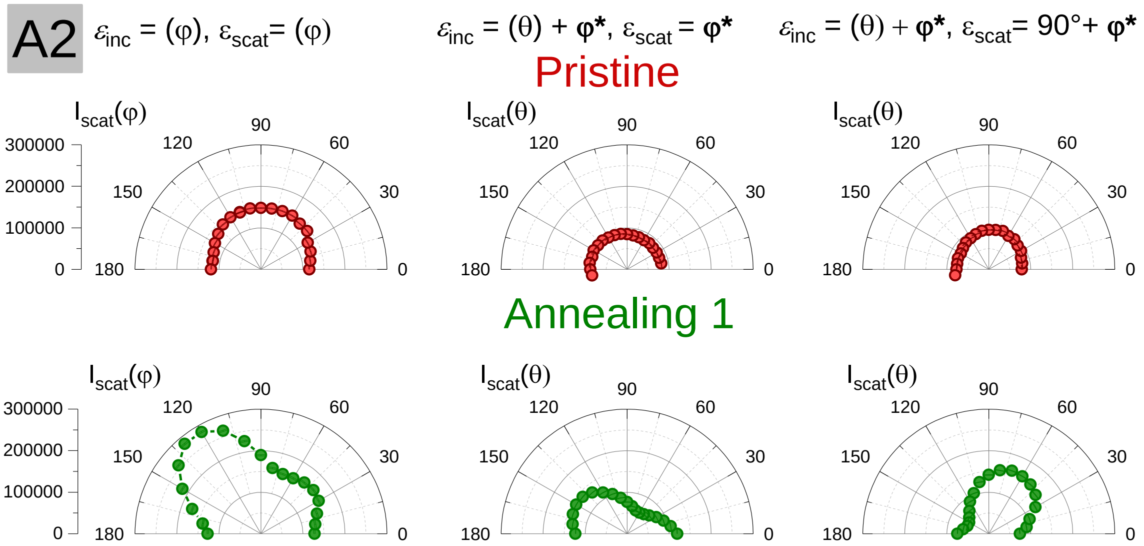

Figure 66: Polarization dependent polar plots PMN-$_{0.4}$PT/Fe heterostructure (pristine and annealed 1) in the three micro-Raman configurations at **A2** mode.

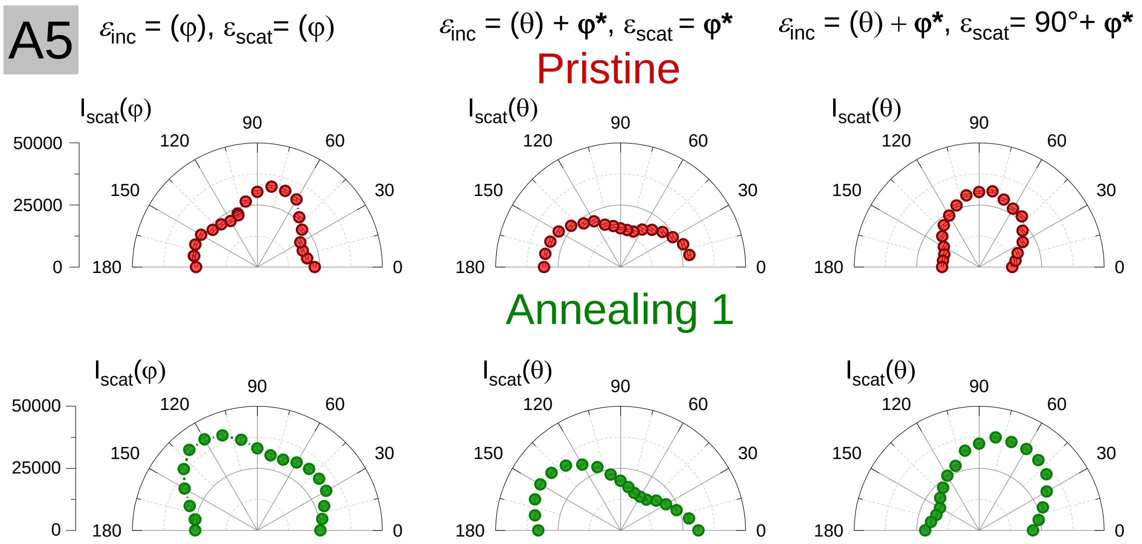

Figure 67: Polarization dependent polar plots PMN-$_{0.4}$PT/Fe heterostructure (pristine and annealed 1) in the three micro-Raman configurations at **A5** mode.

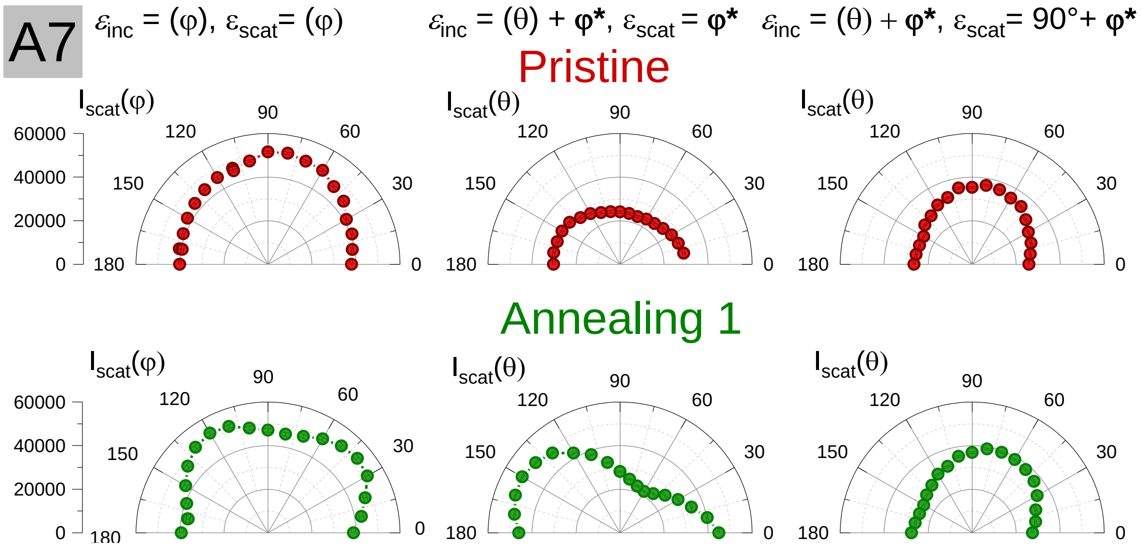

Figure 68: Polarization dependent polar plots PMN-$_{0.4}$PT/Fe heterostructure (pristine and annealed 1) in the three micro-Raman configurations at **A7** mode.

Micro-Raman measurements were taken on freshly deposited samples, *i.e.* the measured substrates were not the same as those used for XRD and MOKE characterizations. To confirm the consistent effect of the thermal annealing on the structural properties of these sample, XRD symmetric scans were repeated on this set of samples. The fitted curves are shown in figure 69.

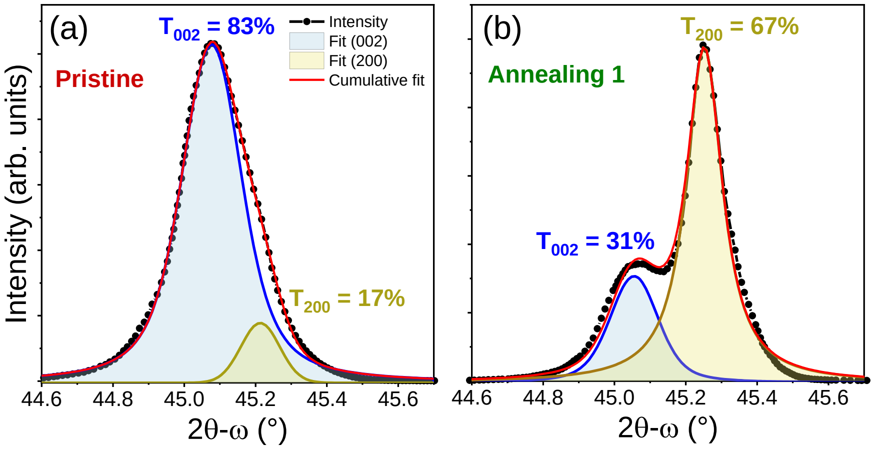

Figure 69: XRD 2θ-ω scans of pristine unannealed and after the first thermal treatment of PMN-$_{0.4}$PT/Fe heterostructure used for Raman characterizations.

Also, in this case a similar evolution of the ratios between the in-plane and out-of-plane domains was observed as a function of the thermal annealing treatments. The majority of domains shifted from mostly out-of-plane (200) (83%) to the in-plane (002) domains (67%) for the pristine and annealed cases, respectively.

4.2.3. MOKE Characterization of PMN-PT/Fe heterostructure

As for the previous chapter, the characterization of the magnetic properties of PMN$_{0.4}$-PT/Fe heterostructures were taken at room temperature by MOKE measurements. In figure 70 the schematic representation of the sample stack and measuring setup is shown.

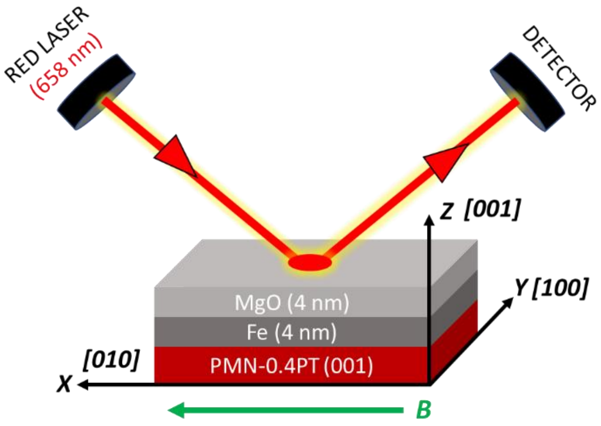

Figure 70: Schematic representation of the PMN-$_{0.4}$PT/Fe heterostructure and experimental setup of Longitudinal MOKE. A He-Ne laser of 658 nm was used.

The hysteresis loops were recorded in-plane along different crystallographic axis of the FE substrate. Polar plots showed an in-plane almost isotropic behavior for the unannealed as grown sample (figure 71a), with a coercive field of around 22.3 Oe along [100] and 20.5 Oe along [010] crystallographic axis. The measurements were then repeated after the 15’ annealing of the sample, always at room temperature (figure 71b). A drastic modification in the magnetic response was observed before and after thermal annealing. Specifically, the sample passed from a purely isotropic behavior to a uniaxial anisotropic one. The observed coercive field was found around 31.5 Oe along [100] and 60.5 Oe along [010] crystallographic axis, while the remanence was found to be 0.4 and 0.87 respectively. The highest remanence and lowest coercive field, signature of the in plane easy axis, was observed at 120° with respect to [100] crystallographic axis. This modification of the in-plane anisotropy after 15’ annealing is fully consisted with the structural characterizations done via XRD, since we noticed a huge modification (increase) in the in-plane orientated ferroelectric domains of the PMN-PT substrate upon annealing. The larger presence of in-plane oriented tetragonal domains leads to a non-uniform in-plane strain, since the interfacial lattice parameters are *a* and *c* (in the case of mostly out-of-plane domains the interfacial face has lattice parameters *a*=*b*). Therefore, the modification of the magnetocrystalline anisotropy driven by PMN-PT domain rearrangement, plus a lower level of structural disorder, as responsible of the transition from an isotropic to an anisotropic in-plane magnetic response.

Polar plots measurements were then repeated after the second annealing (15’+180’), as shown in figure 71c; in this case, an almost isotropic behavior is restored, with coercive fields of 42 Oe along [100] and 40 Oe along [010] crystallographic axis, larger than those measured in the unannealed pristine case. Again, as observed by XRD measurements, longer annealing brings the structure back to a mostly out-of-plane domain population. This is reflected in MOKE, where the magnetic behavior goes back to an isotropic one. The combined polar plot of coercive field and remanence values for the unannealed and annealed stages of the heterostructure are shown in figure 71d and 71e. We underline that the loops are normalized to the magnetic saturation of each curve, so changes in the total magnetization due to annealing, if any, are here not visible. This series of MOKE measurements shows that thermal annealing modifies the magnetic anisotropy of the Fe thin film due to substantial FE structural modifications in the PMN-PT substrate.

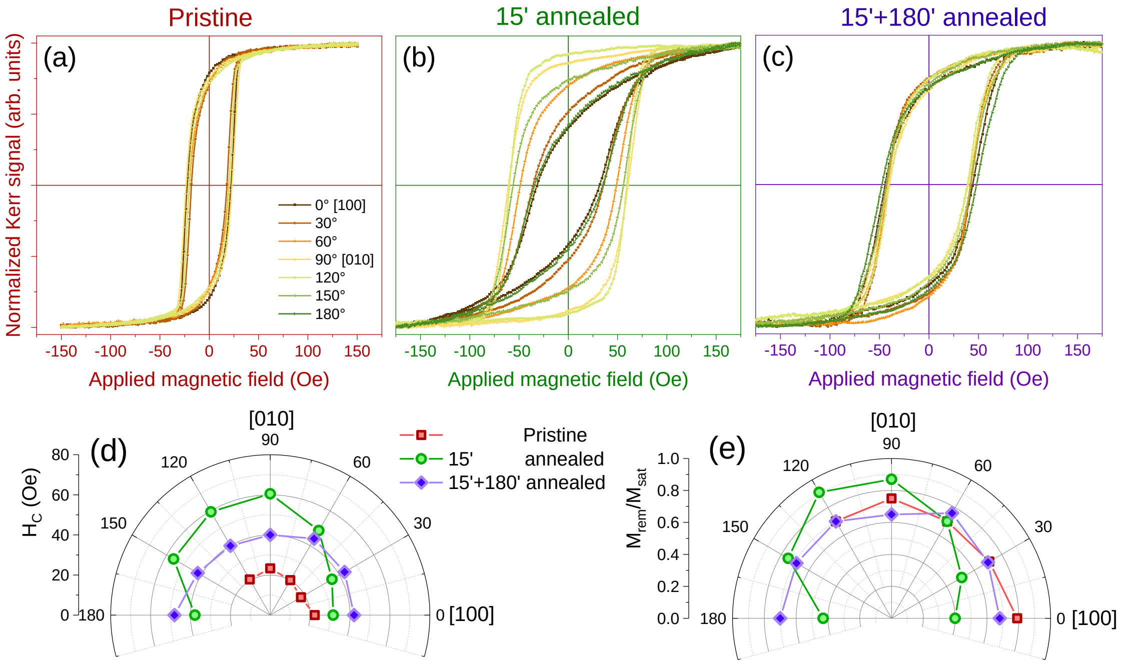

Figure 71: MOKE hysteresis loops for **(a)** as-grown, **(b)** 15’ and **(c)** 15’+180’ annealed PMN-$_{0.4}$PT/Fe heterostructures a function of in-plane magnetic field direction with respect to PMN-PT

crystallographic axis. 0° and 90° azimuthal angles correspond to PMN-PT (001) and (010) axis. **(d,e)** Polar plots of coercive field and magnetic remanence.

4.2.4. X-absorption spectroscopy of PMN-PT/Fe heterostructure

Absorption spectroscopic measurements on PMN-$_{0.4}$PT/Fe heterostructure were carried out APE-HE beamline in TEY mode. The XAS spectra collected at Fe $L_{2,3}$ edges for pristine, short-annealed (15') and long-annealed sample (15'+180') are shown in figure 72, along with the comparison of reference metallic Fe signal (black).[56]

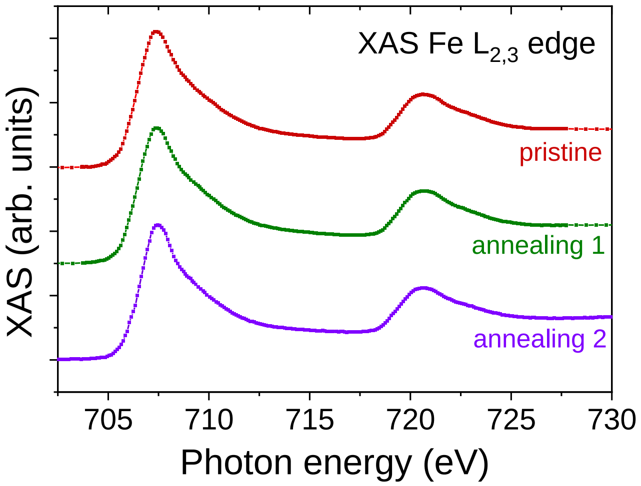

Figure 72: X-ray absorption spectra probed at Fe $L_{2,3}$ edges for the pristine, 15' annealed and 15+180' annealed PMN-$_{0.4}$PT/Fe heterostructure compared with bulk iron[56].

The spectra clearly show that Fe thin film remained metallic over the whole annealing procedure, with no changes in the spectrum and no sign of oxidation. This excludes the possibility of any kind of chemical changes (ion migration) or modification in the coordination geometry of Fe during annealing, which would have affected the magnetic response of the film. Therefore, we report that the modification in the magnetic response of Fe is fully linked to the structural modification of the PMN-PT substrate and not due to chemical modifications of the FM layer itself.

4.3. Conclusions and perspectives

In this chapter, the effects of thermal treatment on PMN-$_{0.4}$PT/Fe multiferroic heterostructure have been investigated by combining structural, magnetometric and spectroscopic characterizations, showing how the local and global properties of PMN-PT crystals can be improved (reduction of local defects and possibly of nanoclusters) and the ferroelectric domain population can pass through an intermediate state, where in-plane domains become majoritarian. Here we quickly sum up the main results of the study, and give some additional discussion and future prospects.

In the case of the pristine unannealed substrate, XRD characterizations showed from a macroscopic point-of-view a larger presence of out-of-plane ferroelectric domains, with broad features in the 2D reciprocal space maps and large FWHM rocking curve, signature of an important presence of local defects and low crystalline quality. This aspect was confirmed locally by micro-Raman measures, where fully isotropic polar plots were found along all crystallographic directions. Once the heterostructure was treated thermally, the structural quality clearly evolved towards a more ordered and better-quality crystallographic properties. The short 15' of annealing over PMN-$_{0.4}$PT ferroelectric Curie temperature led to what results to be a "metastable" intermediate domain population configuration, in which the majority of the ferroelectric domains shifted towards the in-plane one. This modification of the domain population implies a change of the interfacial strain due to the different lattice parameter of the majoritarian PMN-PT tetragonal face in contact with the Fe thin film, leading to a modification of its anisotropic behavior, which moved from an isotropic to an anisotropic one, as observed by MOKE. After this, another annealing cycle was carried out but for a longer time span. This operation led to a modification of the ferroelectric domains, which maintained the improved crystallinity properties and reduced level of local defects, but shifted the main population back towards the out-of-plane direction. As a consequence, the Fe magnetic response went back to an isotropic one, consistently with a lack of preferential in-plane strain due to the out-of-plane FE domains. These results underline the important role of strain and FE structural properties as one of the major actors in the magnetoelectric interfacial coupling. In addition, they spread light on how thermal treatments of FE substrates can be used to optimize the structural properties and tune the domain population of the FE part in multiferroic heterostructures, with possible transitions between different FE domain distributions.

In prospective, these thermal treatments can be used to get advantage of several weaknesses and inconveniences present in FE substrate. For instance, the defects and disordered clusters present in FE's leads to an inefficient magnetoelectric coupling in multiferroics, degrading the effects of external stimuli on the ferroic properties. Hence, a highly ordered structural state and pronounced crystalline quality, up to now mostly achieved by the aging and fatigue processes typical of voltage-controlled FE polarization switching, that I achieved by thermal annealing procedures is always anticipated for an effectual magnetoelectric coupling in multiferroic heterostructures for the optimum utilization in technological implementations. On the other hand, we still have some open question to be figured out.

The first question remained open is the transition upon annealing between the three states measured at room temperature. An in-situ characterization of the structural modifications taking place during the thermal cycles would help in better understanding the energetic balances and transitions taking place from the unannealed pristine configuration to the "fully annealed" substrate. In this prospect, XRD measurements on a heating stage are planned, either with a laboratory source or via beamline measurement at XRD1 beamline (proposal under evaluation).

Regarding the thermal process itself, one possibility is to perform thermal annealing with cooling cycles in presence of an external electric field, to see and compare the modifications in the heterostructure compared to the zero-field cooling case. Another aspect regards mechanical fatigue and loss of performances upon electrical switching. Our group has shown that all the different PMN-PT substrates have the tendency to break their surface into few hundreds nm height surface cracks during electric field induced polarization reversal,[57,58] with patterns in different directions according to the crystallographic growth orientation. These surface cracks, despite being in some case completely reversible, are symptomatic of mechanical fractures created during polarization switching. In the Master thesis of Paola Mantegazza,[59] done in 2019 in our group, preliminary heating studies showed that these surface cracks can be almost completely removed after an annealing over T_C with electric field cooling. These first results, which in part inspired the work presented in this chapter, deserve further investigations.

4.4. Bibliography

[1] Z.-W. Yin, H.-S. Luo, P.-C. Wang, G.-S. Xu, *Ferroelectrics* **1999**, *229*, 207.

[2] X. Zhao, B. Fang, H. Cao, Y. Guo, H. Luo, *Mater. Sci. Eng. B* **2002**, *96*, 254.

[3] E. M. Sabolsky, A. R. James, S. Kwon, S. Trolier-McKinstry, G. L. Messing, *Appl. Phys. Lett.* **2001**, *78*, 2551.

[4] Z. Wang, Y. (John) Yamashita, C. Luo, Y. Sun, T. Karaki, T. Fujii, *J. Ceram. Soc. Japan* **2022**, *130*, 794.

[5] P. Wang, H. Luo, X. Pan, D. Li, Z. Yin, *ISAF 2000. Proc. 2000 12th IEEE Int. Symp. Appl. Ferroelectr. (IEEE Cat. No.00CH37076)* **2000**, *2*, 537.

[6] Q. M. Zhang, J. Zhao, L. E. Cross, *J. Appl. Phys.* **1996**, *79*, 3181.

[7] H. Fu, R. E. Cohen, *Nature* **2000**, *403*, 281.

[8] S.-E. Park, T. R. Shrout, *J. Appl. Phys.* **1997**, *82*, 1804.

[9] D. Viehland, A. Amin, J. F. Li, *Appl. Phys. Lett.* **2001**, *79*, 1006.

[10] G. F. Nataf, M. Guennou, J. M. Gregg, D. Meier, J. Hlinka, E. K. H. Salje, J. Kreisel, *Nat. Rev. Phys.* **2020**, *2*, 634.

[11] D. Meier, S. M. Selbach, *Nat. Rev. Mater.* **2022**, *7*, 157.

[12] P. S. Bednyakov, B. I. Sturman, T. Sluka, A. K. Tagantsev, P. V Yudin, *npj Comput. Mater.* **2018**, *4*, 65.

[13] J. Wang, J. Ma, H. Huang, J. Ma, H. M. Jafri, Y. Fan, H. Yang, Y. Wang, M. Chen, D. Liu, J. Zhang, Y.-H. Lin, L.-Q. Chen, D. Yi, C.-W. Nan, *Nat. Commun.* **2022**, *13*, 3255.

[14] C. Liu, Y. Chen, C. Dames, *Phys. Rev. Appl.* **2019**, *11*, 44002.

[15] D. Dagur, V. Polewczyk, A. Y. Petrov, P. Carrara, M. Brioschi, S. Fiori, R. Cucini, G. Rossi, G. Panaccione, P. Torelli, G. Vinai, *Adv. Mater. Interfaces* **n.d.**, *n/a*, 2201337.

[16] I. Tatsuzaki, K. Itoh, S. Ueda, Y. Shindo, *Phys. Rev. Lett.* **1966**, *17*, 198.

[17] B. Kundys, *Appl. Phys. Rev.* **2015**, *2*, 11301.

[18] K. Uchino, M. Aizawa, L. S. Nomura, *Ferroelectrics* **1985**, *64*, 199.

[19] P. S. Brody, *Ferroelectrics* **1983**, *50*, 27.

[20] B. Kundys, M. Viret, D. Colson, D. O. Kundys, *Nat. Mater.* **2010**, *9*, 803.

[21] B. Kundys, M. Viret, C. Meny, V. Da Costa, D. Colson, B. Doudin, *Phys. Rev. B - Condens. Matter Mater. Phys.* **2012**, *85*, 1.

[22] M. Ahart, M. Somayazulu, R. E. Cohen, P. Ganesh, P. Dera, H. Mao, R. J. Hemley, Y. Ren, P. Liermann, Z. Wu, *Nature* **2008**, *451*, 545.

[23] Z. Necira, A. Boutarfaia, M. Abba, H. Menasra, N. Abdessalem, **2013**.

[24] N. K. Thomas R. Shrout Zung P. Chang, S. Markgraf, *Ferroelectr. Lett. Sect.* **1990**, *12*, 63.

[25] B. Noheda, D. E. Cox, G. Shirane, J. Gao, Z.-G. Ye, *Phys. Rev. B* **2002**, *66*, 54104.

[26] H. Zhang, X. Lu, R. Wang, C. Wang, L. Zheng, Z. Liu, C. Yang, R. Zhang, B. Yang, W. Cao, *Phys. Rev. B* **2017**, *96*, 54109.

[27] X. Shi, J. Wang, J. Xu, X. Cheng, H. Huang, *Acta Mater.* **2022**, *237*, 118147.

[28] D. Viehland, S. J. Jang, L. E. Cross, M. Wuttig, *J. Appl. Phys.* **1990**, *68*, 2916.

[29] G. Xu, Z. Zhong, Y. Bing, Z.-G. Ye, G. Shirane, *Nat. Mater.* **2006**, *5*, 134.

[30] V. Polinger, I. B. Bersuker, *Phys. Rev. B* **2018**, *98*, 214102.

[31] X. Lu, L. Zheng, H. Li, W. Cao, *J. Appl. Phys.* **2015**, *117*, 134101.

[32] A. K. Singh, D. Pandey, O. Zaharko, *Phys. Rev. B* **2006**, *74*, 24101.

[33] H. Zhang, X. Lu, C. Wang, L. Zheng, B. Yang, W. Cao, *Phys. Rev. B* **2018**, *97*, 54114.

[34] T. Rojac, *Commun. Mater.* **2023**, *4*, 12.

[35] S. Yan, X. Hu, X. Lu, S. Xiao, F. Huang, X. Ying, *Adv. Opt. Mater.* **2022**, *10*, 2201092.

[36] A. Negi, H. P. Kim, Z. Hua, A. Timofeeva, X. Zhang, Y. Zhu, K. Peters, D. Kumah, X. Jiang, J. Liu, *Adv. Mater.* **n.d.**, *n/a*, 2211286.

[37] R. Wongmaneerung, R. Guo, A. Bhalla, R. Yimnirun, S. Ananta, *J. Alloys Compd.* **2008**, *461*, 565.

[38] H. Sabarou, V. Drozd, O. Awadallah, A. Durygin, S. Darvish, D. Huang, Y. Zhong, *J. Alloys Compd.* **2019**, *784*, 592.

[39] L. Zheng, X. Lu, H. Shang, Z. Xi, R. Wang, J. Wang, P. Zheng, W. Cao, *Phys. Rev. B* **2015**, *91*, 184105.

[40] C. Yang, E. Sun, B. Yang, W. Cao, *J. Phys. D. Appl. Phys.* **2018**, *51*, 415303.

[41] D. C. Lupascu, U. Rabe, *Phys. Rev. Lett.* **2002**, *89*, 187601.

[42] F. Motti, G. Vinai, A. Petrov, B. A. Davidson, B. Gobaut, A. Filippetti, G. Rossi, G. Panaccione, P. Torelli, *Phys. Rev. B* **2018**, *97*, 94423.

[43] G. Panchal, D. M. Phase, V. R. Reddy, R. J. Choudhary, *Phys. Rev. B* **2018**, *98*, 45417.

[44] G. Panchal, D. Kojda, S. Sahoo, A. Bagri, H. Singh Kunwar, L. Bocklage, A. Panchwanee, V. G. Sathe, K. Fritsch, K. Habicht, R. J. Choudhary, D. M. Phase, *Phys. Rev. B* **2022**, *105*, 224419.

[45] A. Bagri, D. M. Phase, R. J. Choudhary, *Acta Mater.* **2023**, *255*, 119091.

[46] A. Bagri, A. Jana, G. Panchal, S. Chowdhury, R. Raj, M. Kumar, M. Gupta, V. R. Reddy, D. M. Phase, R. J. Choudhary, *ACS Appl. Mater. Interfaces* **2023**, *15*, 18391.

[47] M. Ghidini, F. Maccherozzi, X. Moya, L. C. Phillips, W. Yan, J. Soussi, N. Métallier, M. E. Vickers, N.-J. Steinke, R. Mansell, C. H. W. Barnes, S. S. Dhesi, N. D. Mathur, *Adv. Mater.* **2015**, *27*, 1460.

[48] S. Geprägs, A. Brandlmaier, M. Opel, R. Gross, S. T. B. Goennenwein, *Appl. Phys. Lett.* **2010**, *96*, 142509.

[49] Y. Zhang, M. Liu, L. Zhang, Z. Zhou, B. Peng, C. Wang, Q. Lin, Z.-D. Jiang, W. Ren, Z.-G. Ye, *Appl. Phys. Lett.* **2017**, *110*, 82902.

[50] Y. Zhang, D. Xue, H. Wu, X. Ding, T. Lookman, X. Ren, *Acta Mater.* **2014**, *71*, 176.

[51] J. C. Ho, K. S. Liu, I. N. Lin, *J. Mater. Sci.* **1993**, *28*, 4497.

[52] A. Slodczyk, P. Colomban, *Materials (Basel).* **2010**, *3*, 5007.

[53] Z. Guo, R. Tai, H. Xu, C. Gao, G. Pan, H. Luo, K. Namikawa, *Appl. Phys. Lett.* **2007**, *91*, 81904.

[54] M. Eremenko, V. Krayzman, A. Bosak, H. Y. Playford, K. W. Chapman, J. C. Woicik, B. Ravel, I. Levin, *Nat. Commun.* **2019**, *10*, 2728.

[55] J. A. Lima, W. Paraguassu, P. T. C. Freire, A. G. Souza Filho, C. W. A. Paschoal, J. M. Filho, A. L. Zanin, M. H. Lente, D. Garcia, J. A. Eiras, *J. Raman Spectrosc.* **2009**, *40*, 1144.

[56] T. J. Regan, H. Ohldag, C. Stamm, F. Nolting, J. Lüning, J. Stöhr, R. L. White, *Phys. Rev. B* **2001**, *64*, 214422.

[57] G. Vinai, F. Motti, V. Bonanni, A. Y. Petrov, S. Benedetti, C. Rinaldi, M. Stella, D. Cassese, S. Prato, M. Cantoni, G. Rossi, G. Panaccione, P. Torelli, *Adv. Electron. Mater.* **2019**, *5*, 1970033.

[58] F. Motti, G. Vinai, V. Bonanni, V. Polewczyk, P. Mantegazza, T. Forrest, F. Maccherozzi, S. Benedetti, C. Rinaldi, M. Cantoni, D. Cassese, S. Prato, S. S. Dhesi, G. Rossi, G. Panaccione, P. Torelli, *Phys. Rev. Mater.* **2020**, *4*, 114418.

[59] P. Mantegazza, E-Field Effect on the Fe/PMN-PT Heterostructure Morphology and Magnetism, Università degli Studi di Milano, **2019**.

Chapter 5

Summary and outlook

Objectives

The main aim of my thesis was to study the interfacial coupling in multiferroic heterostructures and how it can be modified by external stimuli, by combining electrical, spectroscopic, structural and magnetic characterizations. Multiferroic systems were composed by a ferromagnetic layer deposited on top of a ferroelectric substrate. In this context, the choice of samples for this thesis were two prototypical heterostructures: $PMN_{0.4}$-PT/Ni and $PMN_{0.4}$-PT/Fe. In chapter 3, the modifications in the magnetic response of Ni and Fe thin films were analyzed as the function of visible light illumination and thermal treatment of the heterostructure, respectively. Visible light illumination induced photostriction effect in the PMN-PT substrate, which further modified the magnetization of Ni thin film via interfacial strain propagation. While, in chapter 4, the magnetism of Fe thin film was modified due to the structural evolution and change of domain population of PMN-PT substrate upon thermal treatments. In both the cases, the link between ferroelectric and ferromagnetic order parameters of the heterostructure was explored, exploiting the high sensitivity of PMN-PT to several different external stimuli, in particular focusing the attention on two parameters up to now poorly investigated compared to the more traditional ones.

Methods and techniques used

Multiferroic heterostructures were studied in depth by means of magnetic, electrical, structural and spectroscopic characterizations.

For the deposition of heterostructures, one-sided polished (001) $PMN\text{-}_{0.4}PT$ substrates were first cleaned with standard acetone and ethanol procedures in ultrasonic bath and rinsed with N_2 flow.

The substrates were then introduced in the growth chambers either at the MBE Cluster of APE-HE beamline for depositing Fe thin films using MBE or at the clean room facility of NFFA-Trieste for performing e-beam sputtering in order to deposit Ni layers. The capping layers were also deposited at the same time in order to prevent the oxidation of metallic films. All the depositions were carried out at the room temperature. After the deposition, various characterizations have been done.

First of all, room temperature *ex-situ MOKE* magnetometry was performed in order to analyze the static macroscopic magnetic properties of Ni and Fe thin film, analyzing the in-plane polar plots for coercive field and magnetic remanence using the angular-dependent hysteresis loops. For the PMN-PT/Ni heterostructure, the MOKE measurements were recorded both in absence and presence of light illumination, comparing the magnetic behavior between unpolarized pristine case and electrically polarized ones. In the case of PMN-PT/Fe heterostructures, MOKE measurements were taken on the same samples after different thermal treatments, comparing the as-grown unpolarized pristine sample before and after thermal treatments.

Regarding the electrical characterization, two main measurements were carried out on the heterostructures: *photocurrent measurements* and *I(E) curves*. The PMN-PT/FM heterostructures were polarized out-of-plane by sweeping an electric field up to ±6 kV cm^{-1} through the thickness of the sample, using AuRh thin films as backside electrode and the FM layer as front one. Current-voltage curves showed well pronounced peaks in correspondence of out-of-plane polarization switching of ferroelectric domains, showing stable and reproducible ferroelectric transitions.

The modification of FE domain populations and structural properties upon either electric field or thermal treatments of PMN-PT were by observed by means of *XRD* by performing θ-2θ scan and rocking curves, combined with 2D reciprocal space maps. These characterizations gave information on the macroscopic structural properties of the FE substrates along the study. Being the ferroelectric crystals highly inhomogeneous, a campaign of *micro-Raman* spectroscopic measurements was carried out on specific samples to analyze the crystalline quality of the substrates on a microscopic level.

The main spectroscopic method used to analyze locally the chemical, electronic and magnetic properties of Fe and Ni thin films was *X-ray absorption spectroscopy and X-ray magnetic circular dichroism* at APE-HE beamline at Elettra synchrotron. By carrying out XMCD sum rules, it was possible to quantify locally the spin and magnetic moment of the magnetic layer under external stimuli, giving the first spectroscopic evidence of light-induced interfacial magnetostriction. A set of these techniques and characterizations gives a complete analysis of the heterostructures being sensitive to external stimulus like light illumination, voltage and thermal annealing.

By combining and examining these various characterization techniques on multiferroic heterostructures, the effects of two external stimuli: light excitation and thermal annealing have been explored for tuning the magnetoelectric coupling at the interface of adjoining of FE and FM materials. It has been shown from the structural characterizations that electrical poling and thermal treatments can substantially modify the structural properties of FE substrate by orientating the domain population from in-plane to out-of-plane direction or vice versa, while magnetometric and spectroscopic analysis helped in analyzing the modifications in the magnetism of FM layer affected by these FE structural changes.

Summary and significance of the two case studies

In the first study, presented in chapter 3, I observed the effects of *visible light illumination* on the magnetic response of magnetostrictive Ni layer due to light-induced photostriction mechanism of ferroelectric PMN-PT substrate. The main result that we found is a reduction of Ni coercive field upon illumination, as observed via MOKE, together with a modification in orbital magnetic moment, as seen via XMCD, proving the interfacial strain transfer between the Ni layer and PMN-PT substrate when exposed to light. By comparing the effects of light illumination between pristine and polarized substrate, we concluded that the main cause for this finding can be attributed the photostrictive contribution coming from the in-plane ferroelectric domains, as the coercive field variation of Ni film strongly reduced after setting the PMN-PT polarization out-of-plane. These results have been obtained after combining several combinations of ferromagnetic layers, PMN-PT compositions and choice of electrodes, which were not presented in the thesis for readability reasons.

Regarding the second case of study, presented in chapter 4, I explored the possibility for modifying the magnetic functionalities of Fe thin films via optimizing the structural arrangement of PMN-PT substrate via *thermal treatments*. As written in the chapter, such approach is to our knowledge a fairly unexplored route in the state-of-the-art literature. Thermal treatments over

PMN-PT Curie temperatures resulted to be an efficient method to tune the orientation of ferroelectric domains without passing through voltage application, a method that generally leads to a degradation of the FE properties. Specifically, the transition from tetragonal to cubic phase above Curie temperature has two main effects: firstly, a substantial reduction of local disorder and defects, as seen via micro-Raman measurements, with an improvement of the crystallinity of the substrate. Secondly, a variation of the ferroelectric domain population, passing from a metastable mostly in-plane one to a majoritarian out-of-plane one after longer annealing. These variations in the structural properties influenced the magnetic anisotropy of Fe interfacial layer. MOKE magnetometry showed a passage from isotropic to anisotropic behavior at the intermediate annealing state, with huge changes in the coercive field and remanence according to the direction of applied magnetic field.

Outlook

What can be the use of these two explored effects for advanced applications involving multiferroic heterostructures? I believe both studies prove light illumination and thermal treatment as two additional levers for tailoring the functionalities of heterostructures, beyond the more classical approach of electric field controlled interfacial strain transfer. The work of this thesis goes beyond the modeled scenario of strain transfer across a defect-free interface, which results in uniform expansion or contraction of the magnetic layer. The multiferroic systems were intrinsically complicated to analyze: in our two case studies we studied the magnetoelectric coupling mechanisms between a relatively simple ferromagnetic layer deposited on a complicated ferroelectric material, that embeds different structural complexities resulting in involuted functionalities. For what concerns the technical applications although being not the main focus of this thesis, the results showed in the 1st chapter about light illumination-controlled PMN-PT/Ni heterostructure showed the potentialities to serve the heterostructure as convertor between light and mechanical energy, as we reported a direct coupling between optical and mechanical functionalities. Potentially, similar photostrictive/magnetostrictive heterostructures can be implemented to develop acoustic or electrical powered devices due to their relatively fast speed and smaller dimensions. Strain mediated magnetization control in low dimensional multiferroics can be a key aspect for magnetic memories. In spintronics, this is typically done by passing large currents to microstrips generating the magnetic fields but at a certain point this huge amount of current give rise to heating effect that becomes a serious problem as the dimensions are reduced below few nanometers. This makes the approach particularly challenging for high-density magnetic devices. In such a case, photostriction can play a role and could be combined with magnetic layer resulting in inverse-magnetostriction effect making it an alternative wireless approach. The analogy of this approach is based on piezoelectric control of magnetic anisotropy via inverse magnetoelastic effect that leads to an additional degree of freedom in hybrid straintronics-spintronic devices, enabling us to maintain stable magnetization induced by light even at zero power.

Another possible idea is to construct photoelastic-piezomagnetic magnetometers by putting a magnetoelastic layer on top of a photoelastic base. The light illumination of variable power/wavelength can induce photostrictive effect on the base being transferred to magnetoelastic layer. This strain dynamics can result in rotation in orientation of magnetization vector of the adlayer, which can yield to electromotive force in a pick-up coil. The low frequency signal can be then analyzed from the magnitude of modulation of emf force using phase sensitive detection techniques. Apart from this, the deposited multiferroics can be used in many other practical and short-term perspectives such as light-controlled gas storage, sonic-ultrasonic emission devices, etc. proving them a potential candidate for envisaging further in upcoming years (a general overview of multiferroic along with some application ideas is depicted in the figure below).

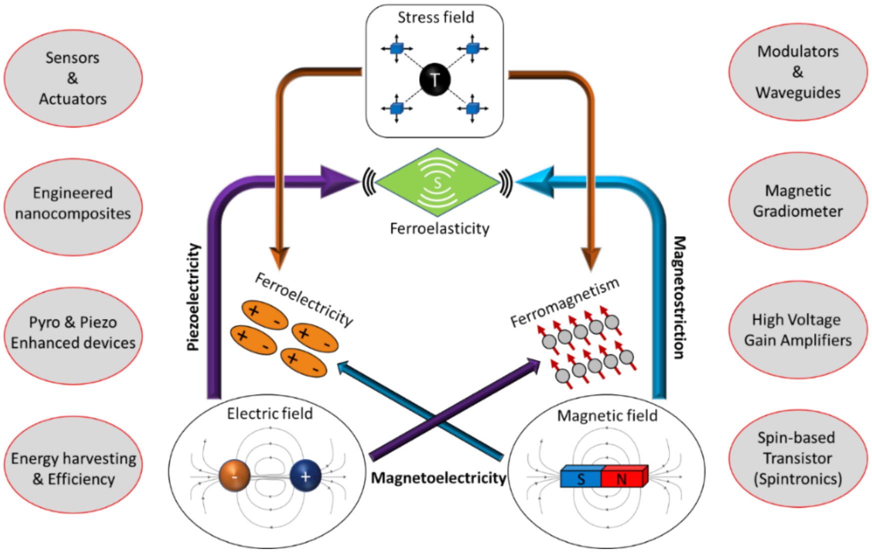

Figure 73: Graphical overview of multiferroics (showing the linkage between ferroelectricity, ferromagnetism and ferroelasticity) with various application aspects.[1]

Regarding the fundamental perspectives, the main perspective will be the optimum utilization of freely-bounded piezoelectric expansion of PMN-PT substrate, as in our studies PMN-PT has been always glued to sample holder which precludes and hinders the optical-straintronics effect. The photostriction is a combination of both the expansion and contraction processes of the size of material at the adjacent directions, therefore a free bounded material will have the full convenience to show photostrictive efficiency at its maximum. Also, other highly photostrictive materials like $KNbO_3$ or SrO should be envisaged in future with a deposition of highly magnetostrictive film on top, for instance FeGa.

The role of electrodes on the top and bottom of ferroelectric substrate also plays a vital role as it can promote or hinder the generation and free flow of charge carriers in the thickness, which results in the photostriction phenomenon. In our study, we used a conductive layer of Au or AuRh to promote the built-in electric field of the PMN-PT affecting the internal electric fields at the interface. These electrodes led to a non-negligible amount of leakage current. The mechanism of manipulating the photovoltaic process deals with the internal electric field caused by the work function at interfaces and the depolarization field induced by the ferroelectric polarization, therefore one should look for right interfacial electrodes in order to boost the photovoltaic/photostrictive efficiency and control the polarization direction of the ferroelectric material. A comparative study of different electrodes with the one used in this study would be very useful in order to identify the ideal candidates.

Finally, as, in the 4th chapter of thesis, we have shown that a short annealing treatment above the first order structural phase transition can subsequently increase the in-plane domain population of PMN-PT substrate, plus according to the fact that we showed in chapter 3rd that presence of in-plane domains is the main responsible for light induced photostrictive effects on magnetostrictive Ni thin film, one should deposit Ni thin film on PMN-PT substrate and heat the heterostructure for 15 minutes in order to have majoritarian in-plane ferroelectric domain population that would affect the magnetic anisotropy of Ni overlayer. Then, one should carry out the magnetic characterizations in presence of light illumination and I expect the magnetic modifications to be huge in the interfacial Ni layer upon exposure to light compared to what we observed.

Reference

[1] D. K. Pradhan, S. Kumari, P. D. Rack, *Nanomaterials* **2020**, *10*, 2072.

Acknowledgements

I am really grateful for the opportunity to be a part of an exceptional research institute and group that provided deep insights into my PhD project. When I embarked on my PhD journey three years ago, little did I know the profound experiences that lay ahead. I began my PhD at the onset of Covid-19 pandemic, a period that presented numerous challenges and uncertainties. I started my work with delay and that too in pandemic condition. This was an uneven start for me, and also was the first time for me to enter in a synchrotron and to experience the operative mechanism of a beamline. At that time, I was asking myself that will I be able to do this but nonetheless, I learned it and made it to the finish line! As I bring my PhD journey to a close, I can genuinely say that I am immensely proud of my accomplishments. This transformative journey has not only shaped me as a researcher but also as an individual, imparting the invaluable lesson that *‘‘perseverance yields fruitful rewards in the long run’’*.

The unwavering commitment and determination displayed by those around me have profoundly influenced my character henceforth, I would like to express my deepest gratitude to every exceptional individual who supported and guided me throughout this transformative journey, enabling me to successfully complete the PhD despite many unforeseen obstacles that arose. First and foremost, I would like to express that I owe an immense debt of gratitude to Professor Giorgio Rossi, coordinator of NFFA Trieste project, for giving me the opportunity to carry out the research activities at his premises, where the possibility of using and exploring the advanced instrumentation has certainly contributed to the successful completion of my project, including the works published during the three years. For the same reason, a sincere thanks goes to Elettra Sincrotrone and CNR-IOM.

Undoubtedly, I cannot envision a better PhD supervisor than Dr. Piero Torelli, whose feedback and guidance played a pivotal role in refining my academic understanding and sharpening the urgings. His constant support, never ending guidance, and encouragement have been invaluable throughout the entire process. His exceptional academic expertise, coupled with commitment to support early career researchers truly make him a role model in the often-competitive realm of academia. I also highly appreciated the meetings we held, which not only served as crucial checkpoints to keep me on track academically, but also provided me with plenty of encouragement. I am profoundly grateful for the immeasurable contributions he made to my academic development and I aspire to follow in your footsteps one day.

Furthermore, the endeavor to achieve this PhD degree would not have been possible without the prodigious help and contribution of Dr. Giovanni Vinai, who superintended my work on a daily basis and was the mentor of each and every single experiment that I carried out in my PhD journey. From the initial stages of refining my research proposal to the final submission of thesis, his unwavering presence and wealth of wisdom have been instrumental in shaping my academic growth. He was the one who followed my first steps in the laboratory and trained me on the functioning of every machine, without ever giving the impression of doubting my abilities showing unlimited patience and efforts. He made me grow both from professional and personal prospect, by showing trust in me and assigning me the responsibilities that sometimes even shivered me, but the results of which made me proud. He was a strong mentor, always persuading me to work hard with utmost diligence, although I never had the feeling that he has given me orders. Finally, I am truly thankful for his firm yet compassionate guidance, which not only facilitated significant contributions to publications during my PhD but also opened the doors I never thought possible.

From a scientific and personal prospective, pursuing PhD is a fair share of challenges. Early on, I encountered setbacks when some of my experiments didn’t worked as per expectations and I had no clue of what to do next. At that time, Dr. Vincent Polewczyk was the one because of whom, what initially appeared as hurdles eventually revealed themselves as blessings in disguise. For me, he was basically the person that I always used to run in absence of Dr. Giovanni Vinai for any kind of doubt, misshaping in the lab or to take scientific advice. Beside the fact that his expertise and knowledge was always way more impactful than me, we became friends more than just colleagues. Although later on he went back to France when I was starting my third year, we are still in touch and hope to be good friends ever. Thanksgiving should also go to him for the numerous suggestions that he gave me about being a valuable person in life. In my last year of PhD, I really missed his presence and support despite of the fact that he always told me that one day he is going to leave and then I'll have to do everything by myself. In any case, words cannot express my gratitude towards him but he understands.

I would be remiss in not mentioning Dr. Aleksander Yu. Petrov ''Sasha'', who helped me a lot during my initial days for the diffraction measurements, later on he made me autonomous in using the machine. He always used to teach me the basics of the measurement using practicality. He also had the habit of testing my understanding of the physical phenomenon by asking very appropriate questions related to the measurements and experimental aspects, that always kept me busy in hunt for finding the answers. This really fortified me for studying new things that further helped me in cumulating more knowledge. I am also thankful and indebted to my lab mates of the 'Cell' group of APE-HE beamline including Dr. Luca Braglia, Dr. Silvia Mauri and PhD's (Ferdinando Bassato, Mario Rivera and Sara Stolfi). Although we didn't work together but would like to thank them for helping me whenever needed and also teaching me a bit of in-operando measurements.

I also feel incredibly fortunate to have had the opportunity to work under the mentorship of many other research scholars and scientists. This includes especially, what regards the members of the NFFA-Trieste family; Dr. Riccardo Cucini, Pietro Carrara and Marta Brioschi who helped me in the HHG photocurrent measurements, Dr. Andrea Giugni and Alice Margherita Finardi for the Raman spectroscopy, and finally, Dr. Pietro Parisse working in the Microfabrication, Micro-sensing and Mechanobiology (3M) laboratory for the AFM. Also, I would like to express appreciation to Jun Fujii (APE-LE), Andrea

Fondacaro and Federico Salvador for giving technical help in the proper functioning of beamline.

My academic journey has also taken me to several schools and conferences in different countries of Europe, marking that Italy was already my first experiences in Europe. Beyond the intellectually stimulating discussions, these trips have provided unforgettable adventures to me. Among the most memorable highlights of my PhD journey was the opportunity to work in collaborative manners with two different groups in Rome and Torino. To be specific, the collaboration at Sapienza University of Rome with Dr. Paolo Postorino and Dr. Claudia Fasolato has been incredibly rewarding in terms of micro-Raman analysis of PMN-PT, allowing us to successfully complete one of the studies presented in the thesis. Therefore, I extend my heartfelt thanks to both of them for welcoming me in their group and helped in making this partnership. On the other hand, the work that I did at INRiM (Torino) on the FE strain measurements in the Advanced Materials Metrology and Life Sciences division under the supervision of Dr. Paola Tiberto was another success, and we managed to establish solid collaborations with her group. This collaboration not only gave us fruitful results but also awarded me with one friend that helped a lot in the measurements and then later on he also came to Trieste for some beamline and MOKE measurements. So, my sincere thanks to Dr. Paola Tiberto.

Lastly, I'd like to acknowledge and dedicate a big thanks to my friends and family, whose support has been a constant source of motivation. Both the formal and informal chats with my friends, whether conducted via phones during lockdowns or in person whenever circumstances allowed, provided a lifeline during the most challenging times. Guys your encouragement played an integral role in my accomplishment. To my mom, dad, and sister: thank you for being everything. I dedicate this PhD thesis to you.

To sum up, *''it takes a village to raise a child''*, and I strongly believe that completing a PhD also requires the same. Henceforth, I would like to express again my deepest appreciation to everyone who played momentous roles in this journey, and now, I'm excited to see what future holds.

List of publications

1. **Dagur**, **D.**, Finardi, A. M., Polewczyk, V., Petrov, A. Y., Dolabella, S., Motti, F., Dobovicnik, E., Giugni, A., Rossi, G., Panaccione, G., Fasolato, C., Torelli, P., & Vinai, G. **Thermal treatment effects on PMN-$_{0.4}$PT/Fe multiferroic heterostructures**. *In preparation*

2. **Dagur**, **D.**, Polewczyk, V., Petrov, A. Y., Carrara, P., Brioschi, M., Fiori, S., Cucini, R., Rossi, G., Panaccione, G., Torelli, P., & Vinai, G. (2022). **Visible light effects on photostrictive/magnetostrictive PMN-PT/Ni heterostructure**. *Advanced Materials Interfaces*, 9(36). https://doi.org/10.1002/admi.202201337.

3. Nanao, Y., Bigi, C., Rajan, A., Vinai, G., **Dagur**, **D.**, King P.D.C. (2024). **Epitaxial growth of AgCrSe$_2$ thin films by molecular beam epitaxy**. *Journal of Applied Physics*, 135(045303) https://doi.org/10.1063/5.0184273.

4. Bigi, C., Qiao, L., Liu, C., Barone, P., Hatnean, M. C., Siemann, G.-R., Achinuq, B., Mayoh, D. A., Vinai, G., Polewczyk, V., **Dagur**, **D.**, Mazzola, F., Bencok, P., Hesjedal, T., van der Laan, G., Ren, W., Balakrishnan, G., Picozzi, S., & King, P. D. C. (2023). **Covalency, correlations, and interlayer interactions governing the magnetic and electronic structure of Mn$_3$Si$_2$Te$_6$.** *Physical Review. B*, 108(5). https://doi.org/10.1103/physrevb.108.054419.

5. Fiori, S., **Dagur**, **D.**, Capra, M., Picone, A., Brambilla, A., Torelli, P., Panaccione, G., & Vinai, G. (2023). **Electronically ordered ultrathin Cr$_2$O$_3$ on Pt(1 1 1) in presence of a multidomain graphene intralayer**. *Applied Surface Science*, 613(155918), 155918. https://doi.org/10.1016/j.apsusc.2022.155918.

6. Polewczyk, V., Chaluvadi, S. K., **Dagur**, **D.**, Mazzola, F., Punathum Chalil, S., Petrov, A. Y., Fujii, J., Panaccione, G., Rossi, G., Orgiani, P., Vinai, G., & Torelli, P. (2023). **Chemical, structural and electronic properties of ultrathin V2O3 films on Al_2O_3 substrate: Implications in Mott-like transitions**. *Applied Surface Science*, 610(155462), 155462. https://doi.org/10.1016/j.apsusc.2022.155462.

7. Brioschi, M., Carrara, P., Polewczyk, V., **Dagur**, **D.**, Vinai, G., Parisse, P., Dal Zilio, S., Panaccione, G., Rossi, G., & Cucini, R. (2023). **Multidetection scheme for transient-grating-based spectroscopy**. *Optics Letters*, 48(1), 167. https://doi.org/10.1364/ol.476958.

8. Carrara, P., Brioschi, M., Longo, E., **Dagur**, **D.**, Polewczyk, V., Vinai, G., Mantovan, R., Fanciulli, M., Rossi, G., Panaccione, G., & Cucini, R. (2022). **All-optical generation and time-resolved polarimetry of magnetoacoustic resonances via transient grating spectroscopy**. *Physical Review Applied*, 18(4). https://doi.org/10.1103/physrevapplied.18.044009.

9. Ghosh, M. P., Kinra, S., **Dagur**, **D.**, Choubey, R. K., Mukherjee, S. (2020). **Evidence of large exchange bias effect in single-phase spinel ferrite nanoparticles**. *Physica Scripta*, 95 (9). https://doi.org/10.1088/1402-4896/abaf90.

‘‘Insanity is doing the same thing over and over again,
but expecting different results.’’

\- Albert Einstein